

AD-751 746

MICROWAVE NETWORK SYNTHESIS

Robert E. Lee, et al

Stanford Research Institute

Prepared for:

Army Electronics Command

November 1972

DISTRIBUTED BY:

NTIS

National Technical Information Service
U. S. DEPARTMENT OF COMMERCE
5285 Port Royal Road, Springfield Va. 22151

AD

Research and Development Technical Report
ECOM-0127-S



AD 751746

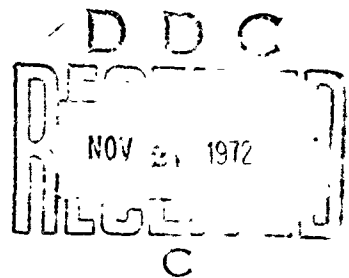
MICROWAVE NETWORK SYNTHESIS

SEMIANNUAL REPORT

By

R. E. Lee A. J. Babr E. G. Crista!

NOVEMBER 1972



DISTRIBUTION STATEMENT

Approved for Public Release; Distribution Unlimited.

ECOM

Prepared by
NATIONAL TECHNICAL
INFORMATION SERVICE
U.S. Government Printing Office
Springfield, Virginia 22151

UNITED STATES ARMY ELECTRONICS COMMAND • FORT MONMOUTH, N.J. 07703

CONTRACT DAAB07-72-C-0127

STANFORD RESEARCH INSTITUTE

Menlo Park, California 94025

ACCESSION for	
NTIS	NTIS Service <input checked="" type="checkbox"/>
DEC	SEC. 5 (a) <input type="checkbox"/>
UNANNOUNCED	<input type="checkbox"/>
JUSTIFICATION	
BY	
DISTRIBUTION AVAILABILITY CODES	
Dist.	AVAIL. CODE/ST. SYMBOL
A	

NOTICES

Disclaimers

The findings in this report are not to be construed as an official Department of the Army position, unless so designated by other authorized documents.

The citation of trade names and names of manufacturers in this report is not to be construed as official Government indorsement or approval of commercial products or services referenced herein.

Disposition

Destroy this report when it is no longer needed. Do not return it to the originator.

UNCLASSIFIED

Security Classification

DOCUMENT CONTROL DATA - R & D

Security classification of title, body of abstract and indexing annotation must be entered when the overall report is classified

1 ORIGINATING ACTIVITY (Corporate author) Stanford Research Institute Menlo Park, California 94025		2a. REPORT SECURITY CLASSIFICATION Unclassified	
		2b. GROUP n/a	
3 REPORT TITLE MICROWAVE NETWORK SYNTHESIS			
4 DESCRIPTIVE NOTES (Type of report and inclusive dates) Semiannual Report Covering the period 1 February to 31 July 1972			
5 AUTHOR(S) (First name, middle initial, last name) Robert E. Lee Alfred J. Bahr Edward G. Cristal			
6 REPORT DATE November 1972		7a. TOTAL NO OF PAGES 124 106	7b. NO OF REFS 29
8a. CONTRACT OR GRANT NO Contract DAAB07-72-C-0127		9a. ORIGINATOR'S REPORT NUMBER(S) Semiannual Report SRI Project 1679	
b. PROJECT NO		9b. OTHER REPORT NO(S) (Any other numbers that may be assigned this report) ECOM-0127-S	
c.			
d.			
10 DISTRIBUTION STATEMENT Approved for public release; distribution unlimited.			
11 SUPPLEMENTARY NOTES Details of illustrations in this document may be better studied on microfiche.		12 SPONSORING MILITARY ACTIVITY U.S. Army Electronics Command Fort Monmouth, New Jersey 07703 AMSEL-TL-MM	
13 ABSTRACT <p>The results of a theoretical and experimental study of the grating transducer are presented. The results clearly demonstrate that such a structure can couple effectively to surface acoustic waves. However the study has revealed two problem areas: (1) It is difficult to prevent the parasitic capacitance to ground from dominating the electrical behavior of such transducers, and (2) the electric fields that "jump over" between nonadjacent electrodes can couple to surface waves (and bulk waves) and therefore must be taken into account in a transducer design. A possible method for improving the transducer design is discussed.</p> <p>A compact channel-dropping-filter geometry consisting of hairpin bandpass and folded-line bandstop filters is proposed for stripline and MIC (microwave integrated circuits). Design details and theoretical and experimental data for a trial channel-dropping filter are presented.</p>			

UNCLASSIFIED

Security Classification

14 KEY WORDS	LINK A		LINK B		LINK C	
	ROLE	WT	ROLE	WT	ROLE	WT
Surface-acoustic-wave transducers						
Interdigital transducer						
Grating transducer						
Folded-line bandstop filter						
Hairpin filter						
Channel-dropping filter						
Multiplexers						

sports Control Symbol
OSD-1366

TECHNICAL REPORT ECOM-0127-S
NOVEMBER 1972

MICROWAVE NETWORK SYNTHESIS

SEMIANNUAL REPORT

SRI Project 1679

CONTRACT DAA207-72-C-0127

Prepared by

R. E. LEE A. J. BAHR E. C. CRISTAL

STANFORD RESEARCH INSTITUTE
MENLO PARK, CALIFORNIA 94025

For

U.S. ARMY ELECTRONICS COMMAND, FORT MONMOUTH, N.J. 07703

DISTRIBUTION STATEMENT

Approved for Public Release, Distribution Unlimited.

24
111

UNCLASSIFIED

Security Classification

14 KEY WORDS	LINK A		LINK B		LINK C	
	ROLE	WT	ROLE	WT	ROLE	WT
Surface-acoustic-wave transducers						
Interdigital transducer						
Grating transducer						
Folded-line bandstop filter						
Hairpin filter						
Channel-dropping filter						
Multiplexers						

PURPOSE OF THE CONTRACT

The purpose of this contract is the synthesis and development of new filters and multiplexers utilizing two new microstrip filter structures-- the hairpin line and the meander line. A second purpose of this contract is the development of a new surface-acoustic-wave grating transducer at UHF frequencies.

Preceding page blank

ACKNOWLEDGMENTS

The authors would like to acknowledge the excellent work of Messrs. H. Moessner and J. Hunt of Stanford Research Institute, who constructed the surface-acoustic-wave devices. Also, Dr. U. Gysel lent his able assistance during the construction and testing of the trial stripline multiplexer.

Preceding page blank

CONTENTS

ABSTRACT	iii
PURPOSE OF CONTRACT.	v
ACKNOWLEDGMENTS.	vii
LIST OF ILLUSTRATIONS.	xi
LIST OF TABLES	xv
I INTRODUCTION.	1
A. Grating Transducers.	1
B. Multiplexers	1
II GRATING TRANSDUCERS	3
A. General.	3
B. Review of Surface-Acoustic-Wave-Transducer Models. . .	5
C. A Circuit Model for the Grating Transducer	10
D. Predictions of the Model	21
E. Experimental Measurements on Surface-Wave Transducers.	27
1. Experimental Approach	27
2. Test-Fixture and Transducer Design and Fabrication	29
3. Experimental Results.	38
a. Input Impedance of Interdigital Transducers.	40
b. Input Impedance of Grating Transducers . . .	42
c. Insertion Loss and Pulse Response of Grating Transducers.	46
d. Measurements on Multi-Section or "Hybrid" Grating Transducers.	53
e. Spurious Signals in Grating Transducers. . .	62

III MULTIPLEXERS	69
A. General	69
B. Folded-Line Bandstop-Filter Design	71
C. Definition of Parameters Used in Design Tables	77
D. Experimental Results	78
IV CONCLUSIONS	85
A. Grating Transducers	85
B. Multiplexers	87
Appendix RAPID-DESIGN CHARTS FOR COUPLED MICROSTRIP LINES	89
REFERENCES	97

DISTRIBUTION LIST

DD FORM 1473

ILLUSTRATIONS

Figure 1	Basic Grating Surface-Acoustic-Wave Transducer	4
Figure 2	Equivalent Circuit for a Thickness-Mode Bulk-Acoustic-Wave Transducer	6
Figure 3	Equivalent Circuit for One Period of an Interdigital Transducer (After Smith ⁷).	8
Figure 4	Equivalent Circuit (Crossed-Field Model) for One Period of an Interdigital Transducer	9
Figure 5	Equivalent Circuit for One Period of a Grating Transducer (Crossed-Field Model)	12
Figure 6	Illustration of the Cascading of Equivalent Circuits for One Periodic Section to Model an N-Section (a) Interdigital Transducer and (b) Grating Transducer	14
Figure 7	Definition of the Transmission Matrix for an N-Port Network	15
Figure 8	Input Resistance as a Function of Frequency for Two Different Values of Capacitance to Ground--A Comparison of Interdigital and Grating Transducers	22
Figure 9	Magnitude of Input Reactance as a Function of Frequency for Two Different Values of Capacitance to Ground--A Comparison of Interdigital and Grating Transducers.	23
Figure 10	Return Loss at an Acoustic Port as a Function of Frequency for Different Load Conditions on the Electrical Port--A Comparison of Interdigital and Grating Transducers.	25
Figure 11	Input Resistance as a Function of Frequency and "Jump-Over" Capacitance for a Grating Transducer	26
Figure 12	Effective Radiation Q as a Function of N, the Number of Transducer Periods	28
Figure 13	Multiport Test Fixture for the Evaluation of Grating and Interdigital Transducers	30

Figure 14	(a) Transformer Equivalent Circuit and Measured Characteristics (b) Measured Transformer Characteristics- Admittance Chart (150-250 MHz)	33
Figure 15	Polar Plot of the Reflection Coefficient of a 470- Ohm Load Measured with Transformer Frequency Variations Calibrated Out (110 to 310 MHz)	34
Figure 16	Experimental Configuration Used for Measuring the Characteristics of a Grating Transducer at 190 MHz . .	35
Figure 17	Photographs of Aluminum Transducer Patterns on Y-Cut Z-Propagating LiNbO_3	36
Figure 18	Equivalent Series Circuit Representation for Either Grating or Interdigital Surface-Wave Transducers . . .	39
Figure 19	Comparison of (a) Measured and (b) Calculated Input Resistance of a Four-Period Interdigital Transducer	41
Figure 20	Comparison of (a) Measured and (b) Calculated Input Reactance of a Four-Period Interdigital Transducer	43
Figure 21	Comparison of Calculated and Measured Input Impedance of a Five-Period Grating Transducer.	45
Figure 22	Comparison of Calculated and Measured Input Impedance of a Three-Period Grating Transducer	47
Figure 23	Schematic Diagram of Test Set-up Used to Measure Insertion Loss and Pulse Response of Surface-Wave Devices.	49
Figure 24	Relative Untuned Surface-Wave Insertion Loss (Response) Between Two Five-Period Grating Transducers.	50
Figure 25	Relative Untuned Surface-Wave Insertion Loss (Response) Between Two Three-Period Grating Transducers.	51
Figure 26	Photographs of Aluminum-Transducer Patterns on YZ LiNbO_3 (Transducer Period = $12 \mu\text{m}$)	54
Figure 27	Schematic Diagram of the Electric-Field Profile in a Multisection Grating Transducer Illustrating the Grating Electric Field E_g and Jump-Over Field E_J . . .	55

Figure 28	Relative Untuned Insertion Loss for Surface Waves Generated and Detected by Three-Section Transducers Having Four Periods per Section (i.e., $N = 13$)	57
Figure 29	Comparison of Measured and Calculated Transducer Response Between a Four-Period Interdigital Transducer and a Thirteen-Period Grating Transducer	59
Figure 30	Detected Surface Acoustic Wave Outputs Between (a) Two Interdigital Transducers and (b) Two Grating Transducers.	61
Figure 31	Pulse Response of a Five-Period Grating Transducer	64
Figure 32	Pulse Response of a Thirteen-Period Grating Transducer	65
Figure 33	Strip-Line Channel-Dropping Filter Utilizing Halfwave Parallel-Coupled-Line Bandpass Filter and Quarter- Wavelength-Line Bandstop Filter.	70
Figure 34	Compact Strip-Line Channel-Dropping Filter Utilizing Hairpin Bandpass Filter and Folded-Line Bandstop Filter	71
Figure 35	Folded-Line Bandstop Filter.	72
Figure 36	Folded-Line-Bandstop-Filter Equivalent Circuit	73
Figure 37	Computed and Theoretical Input Conductance for Trial Bandstop Filter.	75
Figure 38	Schematic Cross-Sectional Representation for Coupled Transmission Lines	77
Figure 39	Photograph of Trial Channel-Dropping Filter.	79
Figure 40	Theoretical and Experimental Normalized Input Conductance of Trial Folded-Line Bandstop Filter	80
Figure 41	Return Loss and Attenuation of Initial Channel- Dropping Filter.	82
Figure 42	Return Loss and Attenuation of Final Channel- Dropping Filter.	83
Figure A-1	Coupled-Line Design Curves	92
Figure A-2	Coupled-Line Design Curves	93

TABLES

**Table 1 Initial Parameter Values for Trial Channel-
Dropping Filter 76**

Preceding page blank

I INTRODUCTION

A. Grating Transducers

In Section II the present state of knowledge concerning the recently proposed grating transducer^{1,2*} is presented. A model for this transducer is proposed and calculations based on this model are presented. The experimental results that have been obtained for this transducer during the reporting period are also presented and are compared with the predictions of the model. The result is an improved understanding of how the grating transducer operates. Changes in design that should lead to an improvement in the performance of such transducers are discussed.

B. Multiplexers

On previous contracts in this series, design methods and tables were developed for very compact filters and transformers--i.e., the hairpin filter and meander-line transformer. The meander-line geometry can easily be converted to a bandstop filter by the addition of shunt stubs. This filter geometry will be referred to as a folded-line bandstop filter. In Section III of this report, details of design and experimental results are presented for combining the hairpin filter and folded-line bandstop filter into a compact channel-dropping filter for use as constant-impedance filters in multiplexers.

* References are listed at the end of the text.

II GRATING TRANSDUCERS

A. General

In many respects, it is the development of the interdigital transducer³ that has been largely responsible for the current flurry of activity in the development of surface-acoustic-wave devices. For frequencies above about 30 MHz, the interdigital transducer is really the only practical surface-acoustic-wave transducer that has been available. The subject of this report is a new surface-acoustic-wave transducer--the grating array.

The basic configuration for the grating transducer, depicted schematically in Figure 1, is composed of a planar array of thin metal electrodes situated on the surface of a piezoelectric medium. A voltage applied between the two terminals produces an electric field across each gap by virtue of the capacitance that exists between adjacent fingers. At any instant of time the fields in all the gaps are in phase, since the array is much smaller than an electromagnetic wavelength. Thus, if the gaps are spaced by a surface acoustic wavelength, λ , or an odd multiple thereof, cumulative surface-wave generation will take place. This transducer differs from other "single-phase" grating transducers⁴ in that, for those transducers the potential on each finger is the same, whereas in this case the potential on each finger is different.

Acoustically, this transducer operates much like an interdigital transducer except that the minimum spacing between coupling-gap centers is one wavelength instead of one-half wavelength. Electrically, however, the coupling gaps are in series, whereas for the interdigital array they

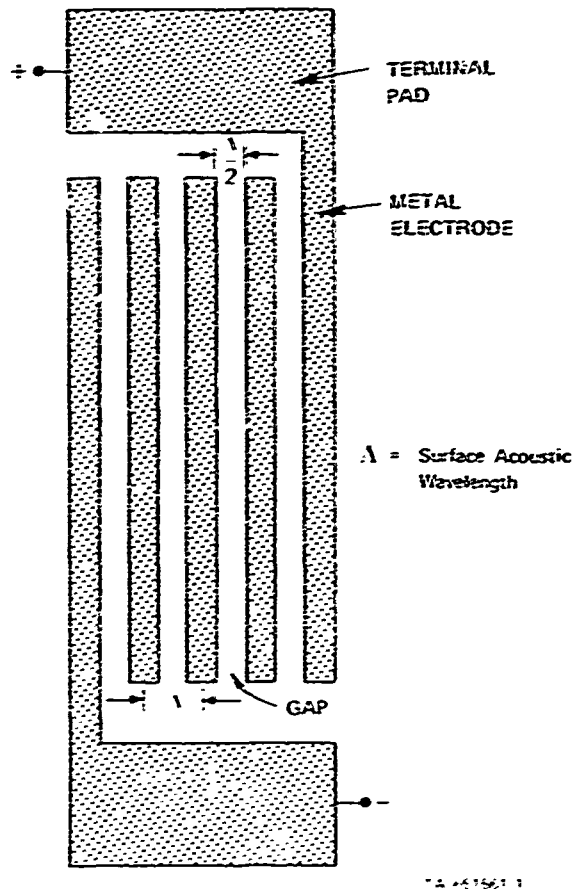


FIGURE 1 BASIC GRATING SURFACE-ACOUSTIC-WAVE TRANSDUCER

are in parallel. Thus it is clear that the input impedance should be much higher than for an interdigital array.

Besides increased input impedance, the grating transducer appears to offer the following advantages when compared to an interdigital transducer:

- (1) The grating array can be made in a single planar process with electrodes and gaps one-half acoustic wavelength wide, thus easing photolithographic tolerances for high-frequency-transducer fabrication.
- (2) A short between adjacent fingers does not completely prevent a grating transducer from operating. Also,

small breaks in any number of the fingers (except the first and last) will not significantly affect the operation of the transducer.

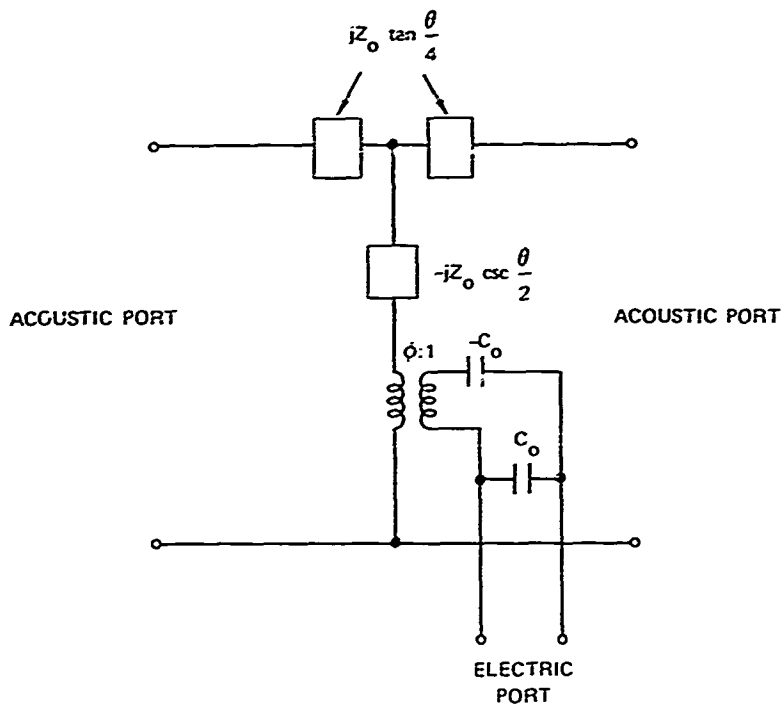
- (3) Since the voltage applied to the grating transducer is divided between all of the gaps, the power-handling capabilities with respect to voltage breakdown should be greater for this transducer.

An equivalent circuit model for a grating transducer will be developed in the following sections. The results of calculations based on this model will be presented and then compared with the results of measurements made on several different grating transducers. Based on this comparison, the validity of the model and the general characteristics of a grating transducer will be discussed. In particular, the effects of parasitic capacity to ground and nonadjacent interelectrode, or "jump-over" field components between various fingers of the grating will be examined.

B. Review of Surface-Acoustic-Wave-Transducer Models

Equivalent circuit models for bulk-acoustic-wave transducers were developed by Mason⁵ many years ago and have been proven to provide accurate descriptions of the behavior of such transducers. These models are derived from exact solutions of the one-dimensional wave equations for piezoelectric materials. A typical equivalent circuit is shown in Figure 2. The T-network in this figure represents a section of acoustic transmission line. This acoustic transmission line is coupled to the electrical port by means of the piezoelectric effect; this coupling is represented by the transformer in the shunt arm of the network.

The excitation of surface acoustic waves cannot be precisely represented as a one-dimensional problem. However, it was proposed and demonstrated by Krairojananan and Redwood⁶ that an interdigital surface-acoustic-wave transducer could be accurately represented by a cascade of



$$\theta = 2\pi \frac{f}{f_0}$$

f_0 = Frequency where the transducer is one wavelength thick = $\omega_0 / 2\pi$

C_0 = The static or "clamped" capacitance of the transducer

Z_0 = Acoustic impedance of the piezoelectric material

$$\phi^2 = \frac{\omega_0 C_0 K^2 Z_0}{\pi} \quad \text{where } K \text{ is the electromechanical coupling factor of the material.}$$

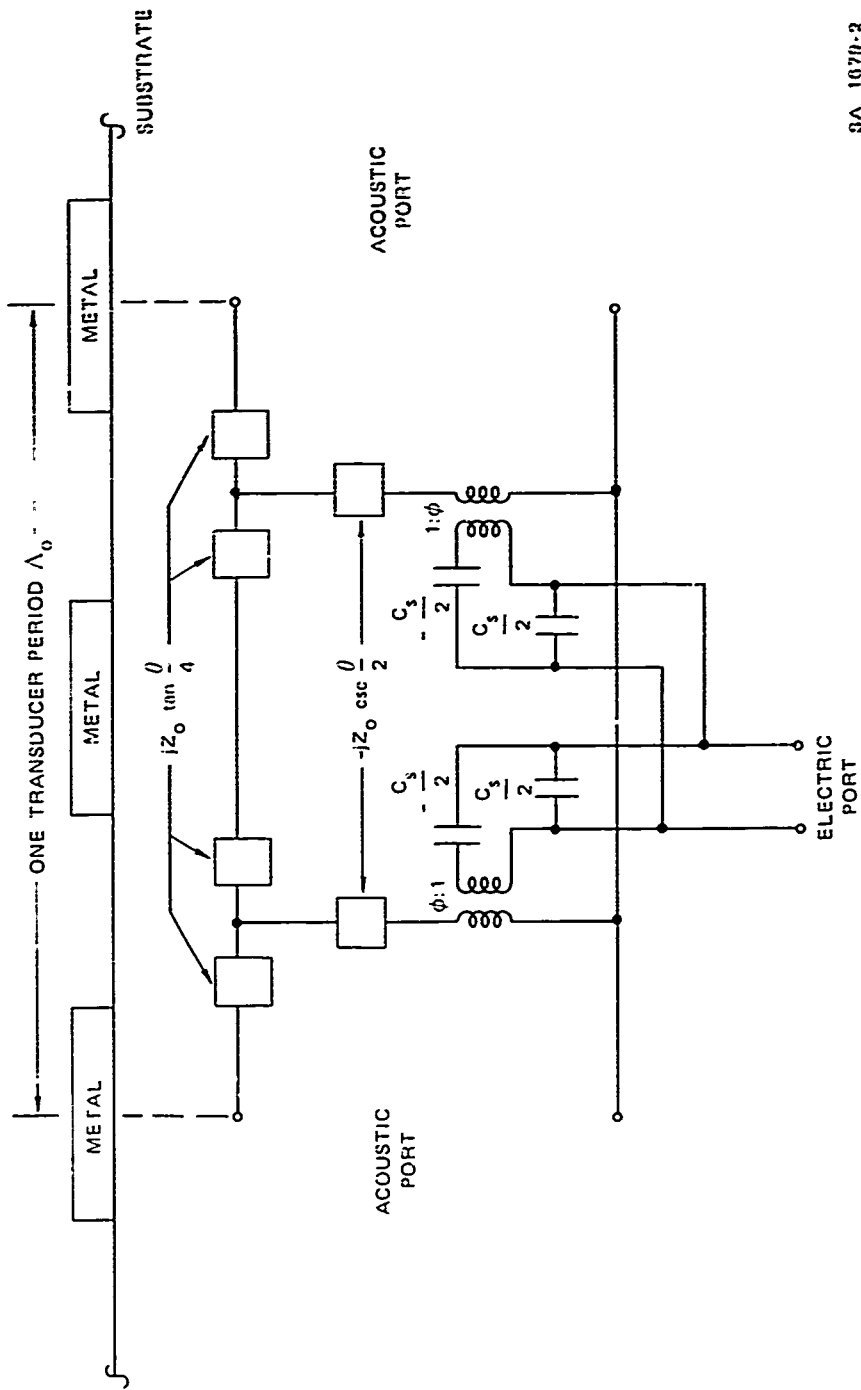
SA 1679-1

FIGURE 2 EQUIVALENT CIRCUIT FOR A THICKNESS-MODE BULK-ACOUSTIC-WAVE TRANSDUCER

circuits like that shown in Figure 2. About the same time Smith and coworkers at Stanford University independently proposed using the same kind of equivalent circuit for interdigital surface-wave transducers, and they subsequently published a comprehensive treatment of this type of model.⁷ Smith's equivalent circuit for one period of an interdigital transducer is shown in Figure 3. In this circuit the quantity C_s is the capacitance per period. The circuit as shown in Figure 3 is designated by Smith as the "in-line" model. If the negative capacitances in Figure 3 are short-circuited, the circuit becomes the "crossed-field" model. Smith shows experimentally that the "crossed-field" model should be used for surface waves propagating in the Z-direction on Y-cut lithium niobate. On the other hand, the "in-line" model seems to be more appropriate when the substrate is a piezoelectric ceramic.^{8,9}

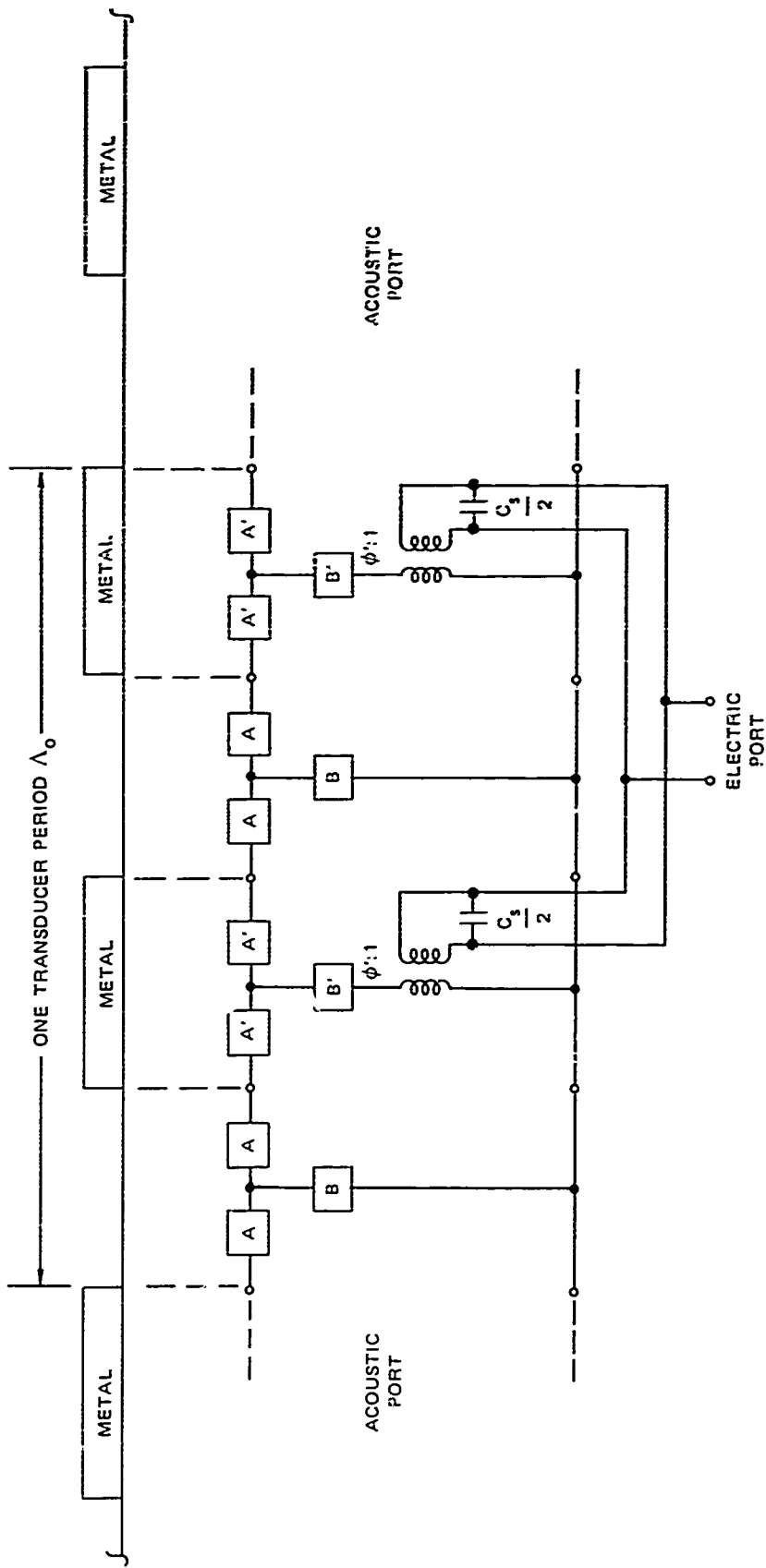
As the variety of surface-wave devices increased, it soon became apparent that certain second-order effects were not modeled by the Smith circuit of Figure 3. In particular, acoustic reflections between metal electrodes are caused by the shorting of the tangential electric fields under the metal electrodes and the mass loading of the electrodes. Jones et al.¹⁰ modeled this effect by breaking up the transducer into metalized and unmetalized portions. Their equivalent circuit is shown in Figure 4. In this circuit only the sections under the metal fingers are assumed to be coupled to the electrical port. If the radiation conductance computed using the circuit given in Figure 3 is assumed to be correct, the transformer ratio σ' for the circuit of Figure 4 must be adjusted if calculations using that circuit are to give the same value of radiation conductance. Analysis of the two circuits shows that one must have

$$\sigma' = \sqrt{2} \sigma \quad . \quad (1)$$



SA 107D-2

FIGURE 3 EQUIVALENT CIRCUIT FOR ONE PERIOD OF AN INTERDIGITAL TRANSDUCER (After Smith?)



$$A = jZ_0 \tan \frac{\theta}{8}$$

$$A' = jZ_0' \tan \frac{\theta}{8}$$

$$B = -jZ_0 \csc \frac{\theta}{4}$$

$$B' = -jZ_0' \csc \frac{\theta}{4}$$

DA-1070-0

FIGURE 4 EQUIVALENT CIRCUIT (crossed-field model) FOR ONE PERIOD OF AN INTERDIGITAL TRANSDUCER

For materials with fairly strong coupling and for frequencies below a few hundred MHz the shorting of the tangential electric fields is the dominant cause of the impedance discontinuity between the metalized and unmetalized portions of the transducer. Under this assumption the acoustic impedance of the metalized portion is approximately given by

$$Z'_0 = Z_0 / (1 + k^2/2) \quad (2)$$

where k^2 is the square of the electromechanical coupling coefficient for surface acoustic waves.

Smith¹¹ has used a similar circuit for modeling the effect of the impedance discontinuity due to metalization, but he includes coupling transformers in both the metalized and unmetalized portions of his circuit. By doing this he obtains the correct radiation conductance without having to make the transformer ratio different from the ratio he used in his original model (see Figure 3).

Although the circuits that include the effects of impedance discontinuities due to electrodes give the same value of radiation conductance as Smith's original model, they give different values of radiation susceptance at the acoustic synchronism frequency f_0 . Smith's original model gives a zero value for the radiation susceptance at synchronism, while the more detailed models give non-zero, negative values for this quantity. However, this synchronous negative susceptance is of the order k^2 , and thus this small discrepancy between the models is generally neglected.

C. A Circuit Model for the Grating Transducer

The equivalent circuit for an interdigital transducer is based on the assumption that all electric fields emanating from one electrode terminate only on adjacent electrodes--i.e., that no electric fields

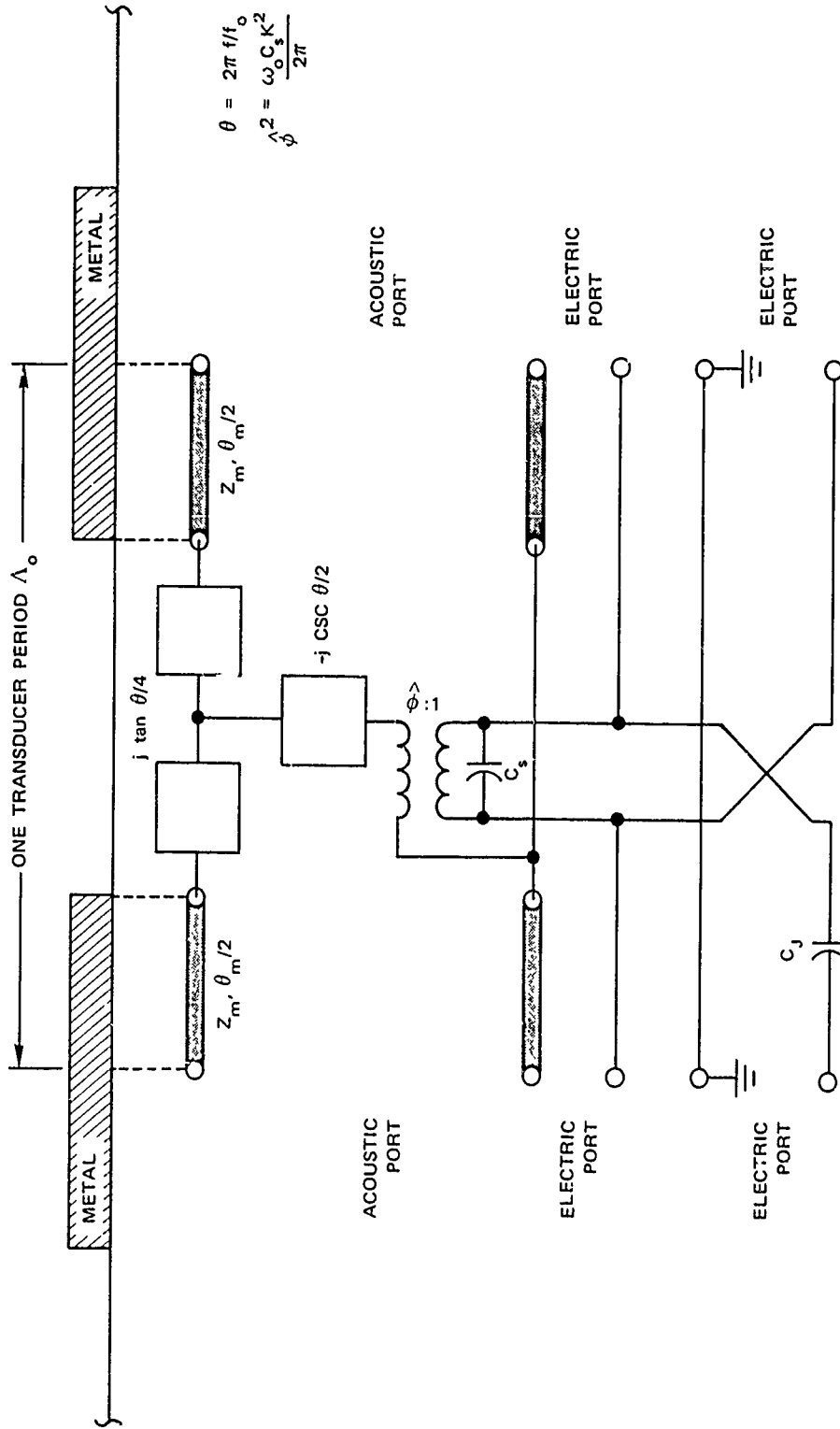
"jump over," or extend to nonadjacent electrodes so as to terminate on an electrode of opposite polarity that is farther away. One would guess that this is a good assumption for the interdigital transducer because the charges on adjacent electrodes are always opposite and equal.

In the grating transducer, next-nearest-neighbor electrodes (and others farther away) are not as well shielded by the nearest-neighbor electrodes as they are in the interdigital transducer. This is because in an interdigital transducer, if a charge Q is imposed on a given electrode, a charge $-Q$ is imposed on adjacent electrodes. This is not true in a grating transducer. Thus, in general, there might exist significant field components spanning every pair of electrodes in the grating structure. If this is the case, the equivalent circuit must be quite complicated in order to account for coupling to every field component. In addition, the significant field components and their corresponding coupling factors are difficult to determine.

Thus, to begin the development of an equivalent circuit model for the grating transducer one must make some rather bold assumptions. In what follows it will be assumed initially that the strongest electric-field component occurs between adjacent electrodes. The model will allow for some electric field occurring between next-nearest-neighbor electrodes, but it will assume that this field component does not couple to the surface acoustic wave. By comparing experimental results with those obtained from the model, one can hopefully modify the model until theory and experiment agree.

The proposed equivalent circuit for one period of the grating transducer is shown in Figure 5. Since the absolute value of acoustic impedance for surface acoustic waves is not known, the acoustic impedances in the circuit have been normalized to the acoustic impedance of an unmetalized section. Thus,

$$Z_0 = 1 \quad (3a)$$



SA-1679-4

FIGURE 5 EQUIVALENT CIRCUIT FOR ONE PERIOD OF A GRATING TRANSDUCER (crossed-field model)

and

$$Z_m = 1/(1 + k^2/2) \quad . \quad (3b)$$

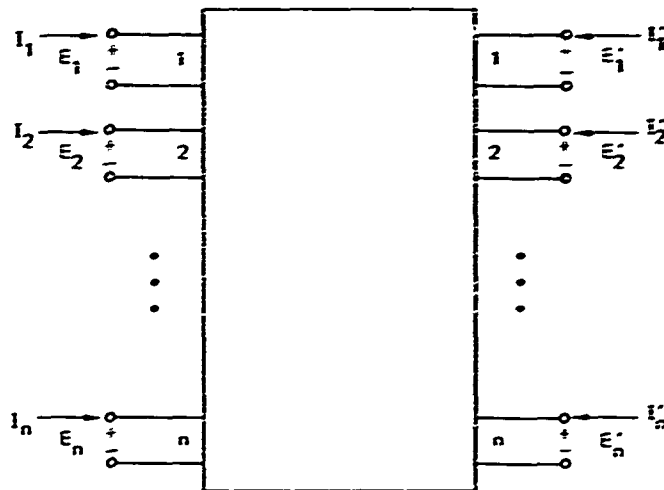
In addition, the transformer ratio, $\hat{\phi}$, has been normalized to eliminate acoustic impedance. With this normalization it is still possible to compute absolute values for the electrical input impedance, reflection coefficient at an acoustic port, and power transfer between the electrical and acoustic ports.

Other quantities to be noted in the equivalent circuit of Figure 5 are θ_m , the transit angle of the metalized section, and C_j , the "jump-over" capacitance between next-nearest-neighbor electrodes. By allowing different transit angles in the metalized and unmetalized sections one can model different electrode width-to-gap ratios. Note that the inclusion of C_j results in the addition of an extra pair of electrical ports in the circuit.

The electrode and gap widths were initially chosen to be one-half acoustic wavelength. This decision was based on a consideration of the impulse model¹² for surface-acoustic-wave transducers. In this model it is assumed that the surface wave is driven by delta functions placed at the corners of each electrode. Adjacent delta functions separated by a gap have opposite polarities. Thus, since the polarity of the electric field is the same in each gap in the grating, it follows that the electrodes and the gaps in the grating should be one-half wavelength wide.

Finally, it should be noted in Figure 5 that coupling between acoustic and electric quantities exists only in the unmetalized sections of the transducer. The choice of whether the coupling is placed in the metalized or unmetalized sections is arbitrary, but both sections cannot be coupled at the same time. If they were, the circuit for a transducer having more than one period would either result in no coupling at

The definition of the transmission matrix for a 2n-port network is given in Figure 7. The definition is such that the transmission matrix for a network that is composed of N 2n-port networks in cascade is obtained simply by multiplying the transmission matrices for the individual networks together. The multiplication is carried out from right to left.



$$\begin{bmatrix} E_1 \\ I_1 \\ E_2 \\ I_2 \\ \cdot \\ \cdot \\ \cdot \\ E_n \\ I_n \end{bmatrix} = \tilde{T} \begin{bmatrix} E'_1 \\ -I'_1 \\ E'_2 \\ -I'_2 \\ \cdot \\ \cdot \\ \cdot \\ E'_n \\ -I'_n \end{bmatrix}$$

SA-1679-6

FIGURE 7 DEFINITION OF THE TRANSMISSION MATRIX FOR AN N-PORT NETWORK

For the network shown in Figure 5 it is simplest to define sub-matrices for the metalized and unmetalized portions of the circuit and obtain the matrix for the periodic section by multiplying the sub-matrices together--viz.,

$$\tilde{T} = \tilde{T}_m - \tilde{T}_0 - \tilde{T}_m \quad (4)$$

where \tilde{T} is the matrix for one periodic section of a grating transducer, \tilde{T}_m is the matrix for one-half of a metalized portion, and \tilde{T}_0 is the matrix for an unmetalized portion.

The equivalent circuit for the metalized portion of the transducer is simply a section of acoustic transmission line. The transmission matrix for a transmission line is well known.¹³ Thus,

$$\tilde{T}_m = \begin{bmatrix} \cos \frac{\theta}{2} & jZ_H \sin \frac{\theta}{2} & 0 & 0 & 0 & 0 \\ j\frac{1}{Z_H} \sin \frac{\theta}{2} & \cos \frac{\theta}{2} & 0 & 0 & 0 & 0 \\ 0 & 0 & 1 & 0 & 0 & 0 \\ 0 & 0 & 0 & 1 & 0 & 0 \\ 0 & 0 & 0 & 0 & 1 & 0 \\ 0 & 0 & 0 & 0 & 0 & 1 \end{bmatrix} \quad (5)$$

Analysis of the unmetalized portion of the transducer is somewhat more complicated. After considerable algebra one obtains

$$\begin{bmatrix}
 \cos \frac{\pi}{2N} & j \sin \frac{\pi}{2N} & -\tau_{15} & 0 & \tau_{15} & 0 \\
 j \sin \frac{\pi}{2N} & \cos \frac{\pi}{2N} & -\tau_{25} & 0 & \tau_{25} & 0 \\
 0 & 0 & 0 & 0 & 1 & 0 \\
 \tau_{25} & \tau_{15} & -j \frac{\pi}{\omega C_s} & 0 & j \frac{\pi}{\omega C_s} & 1 \\
 j \frac{\pi}{\omega C_s} & j \frac{\pi}{\omega C_s} & \begin{bmatrix} R & C \\ 0 & S \end{bmatrix} & -j \frac{\pi}{\omega C_s} & -\begin{bmatrix} R & C \\ 0 & S \end{bmatrix} & 0 \\
 -\tau_{25} & -\tau_{15} & j \frac{\pi}{\omega C_s} & 1 & -j \frac{\pi}{\omega C_s} & 0
 \end{bmatrix} \quad (5)$$

where

$$\tau_{15} = \sqrt{\frac{\pi}{\omega C_s} k^2} (\cos \frac{\pi}{2} - 1) \quad (7a)$$

$$\tau_{25} = j \sqrt{\frac{\pi}{\omega C_s} k^2} (\sin \frac{\pi}{2}) \quad (7b)$$

$$\pi = \frac{\pi}{\omega C_s} + \frac{\pi}{2\tau} \sin \frac{\pi}{2} \quad (7c)$$

Once the transmission matrix for an N-period transducer is obtained, it is possible to calculate various terminal quantities from the matrix elements. For example, the electrical input impedance, Z_{in} , is found by solving the matrix equation subject to the following terminal conditions:

$$Z_{in} = E_2 / I_2$$

$$-Z_1 = E_1 / I_1 = E_1' / I_1'$$

$$E_2' = 0$$

$$I_3 = I_3' = 0$$

where Z_L is the load seen looking out of an acoustic port. In the above expressions the symbols E and I are used to represent both electrical and acoustic quantities. The subscript "1" is used to represent an acoustic port and "2" and "3" to represent electrical ports. The unprimed quantities refer to the input ports of Section 1 in Figure 6(b) and the primed quantities refer to the output ports of Section X in that figure. One obtains

$$Z_{in} = \frac{T_{31} Z_L + T_{32} + T_{34} (I_2'/I_1') - T_{35} (E_3'/I_1')}{T_{41} Z_L + T_{42} + T_{44} (I_2'/I_1') - T_{45} (E_3'/I_1')} \quad (8)$$

where

$$E_3'/I_1' = (T_{61} Z_L + T_{62} + T_{64} (I_2'/I_1'))/T_{65} \quad (9a)$$

and

$$I_2'/I_1' = \frac{Z_L^2 (T_{25} T_{61} - T_{21} T_{65}) + Z_L (T_{25} T_{62} + T_{15} T_{61} - T_{11} T_{65} - T_{22} T_{65}) + T_{15} T_{62} - T_{12} T_{65}}{Z_L (T_{24} T_{65} - T_{25} T_{64}) + T_{12} T_{65} - T_{15} T_{64}} \quad (9b)$$

In these expressions the T_{ij} are the matrix elements for the overall transmission matrix of the grating transducer,* and

$$Z_L = Z_n \frac{\cos \varphi_n' + jZ_n \sin \varphi_n'}{Z_n \cos \varphi_n' + j \sin \varphi_n'} \quad (10)$$

* Note that the indices of the matrix elements will take on the integer values 1 to $2n$ in general. In this case $n = 3$.

is the normalized acoustic impedance loading the acoustic ports of the transducer. If the end fingers of the transducer have a total transit angle θ_{end} , then

$$\theta'_m = \theta_{end} - \theta_m / 2 \quad (11)$$

Similarly, to find the normalized acoustic input impedance, Z_A , at an acoustic port one uses the following terminal conditions:

$$Z_A = E_1 / I_1$$

$$-Z_L = E'_1 / I'_1$$

$$-Z_E = E_2 / I_2$$

$$E'_2 = 0$$

$$I_3 = I'_3 = 0$$

where Z_E is the electrical impedance loading the electrical port. One obtains

$$Z_A = \frac{T_{11} Z_L + T_{12} + T_{14} (I'_2 / I'_1) - T_{15} (E'_3 / I'_1)}{T_{21} Z_L + T_{22} + T_{24} (I'_2 / I'_1) - T_{25} (E'_3 / I'_1)} \quad (12)$$

where E'_3 / I'_1 is again given by Eq. (9a) and

$$I'_2 / I'_1 = \frac{Z_L Z (T_{41} T_{65} - T_{45} T_{61}) + Z (T_{42} T_{65} - T_{45} T_{62}) + Z (T_{31} T_{65} - T_{35} T_{61}) + T_{32} T_{65} - T_{35} T_{62}}{Z (T_{45} T_{64} - T_{44} T_{65}) + T_{35} T_{64} - T_{34} T_{65}} \quad (13)$$

As mentioned before, the complexity of these equations requires that calculations be done on a digital computer. It is highly desirable to have simpler equations so that one may arrive at an approximate design quickly and easily. If one assumes that there is no jump-over capacitance, that the acoustic impedances in the metalized and unmetalized sections are the same, and that the fingers and gaps are all one-half wavelength wide, the following approximate equations for the input impedance, $\hat{R}_a \div j\hat{X}_a$, at the synchronism frequency, f_0 , can be deduced:

$$\hat{R}_a \approx \frac{1}{\left[1 + \frac{C \cdot N}{C_s}\right]^2} \cdot N^2 \cdot \frac{k^2}{\pi} \cdot \frac{1}{\rho_0 C_s} \quad (14a)$$

$$\hat{X}_a \approx \frac{1}{1 + \frac{C \cdot N}{C_s}} \cdot N \cdot \frac{1}{\rho_0 C_s} \quad (14b)$$

Note that these equations include the effect of a capacitance to ground, C_g , at the input. The corresponding equations for an interdigital transducer are

$$\hat{R}_a \approx \frac{1}{\left[1 + \frac{C}{NC_s}\right]^2} \cdot \frac{4k^2}{\pi} \cdot \frac{1}{\rho_0 C_s} \quad (15a)$$

$$\hat{X}_a \approx \frac{1}{1 + \frac{C}{NC_s}} \cdot \frac{1}{N} \cdot \frac{1}{\rho_0 C_s} \quad (15b)$$

It is interesting to note from these equations that for the grating transducer the effect of C_g becomes greater as N increases, while for the interdigital transducer the effect of C decreases as N increases. In what follows it will be assumed that k^2 is the same for both transducers. In general, however, C_s , the capacitance per period, will be different for the two transducers.

D. Predictions of the Model

This section will present some sample calculations made using the equivalent circuit model for a grating transducer that was described in the last section and a similar model for the interdigital transducer.⁷ The transducer parameters for these sample calculations were chosen to correspond to some extent to the parameters of the experimental devices to be described in later sections. The capacitance per period of the grating transducer was assumed to be one-half that of an interdigital transducer having the same aperture. However, the validity of this assumption remains to be determined.

Figure 8 shows the input resistance as a function of frequency for corresponding grating and interdigital transducers. Note the relatively large effect that a small amount of capacitance to ground has on the input resistance of a grating transducer. This effect is also predicted by the simplified expressions given in Eqs. (14a) and (15a). The corresponding input reactance magnitudes are shown in Figure 9. If one computes the electrical Q for the cases shown in these figures he finds that the Q of the interdigital transducer only varies between 4.4 and 5, while the Q of the grating transducer varies between 18 and 92. Thus the introduction of a small amount of capacitance to ground has two large effects on the grating transducer: It reduces the input resistance and increases the Q. The experimental results to be discussed later will verify that capacitance to ground constitutes a major problem that must

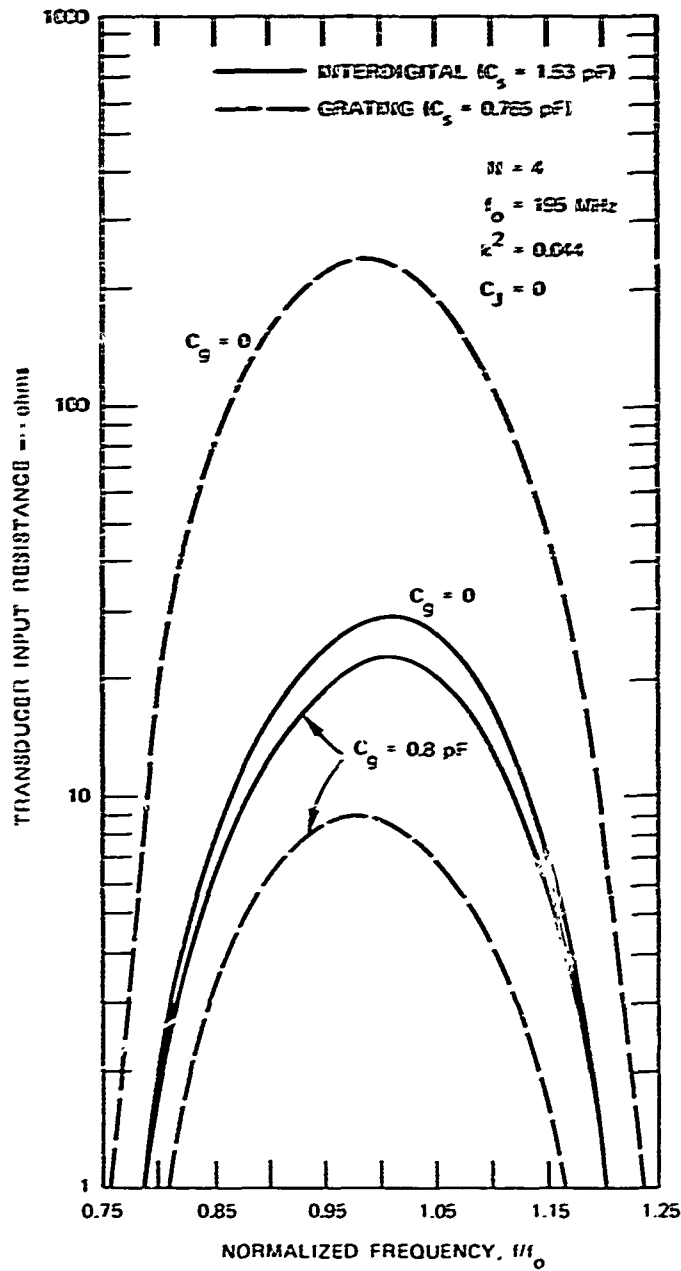


FIGURE 8 INPUT RESISTANCE AS A FUNCTION OF FREQUENCY FOR TWO DIFFERENT VALUES OF CAPACITANCE TO GROUND — A COMPARISON OF INTERDIGITAL AND GRATING TRANSDUCERS

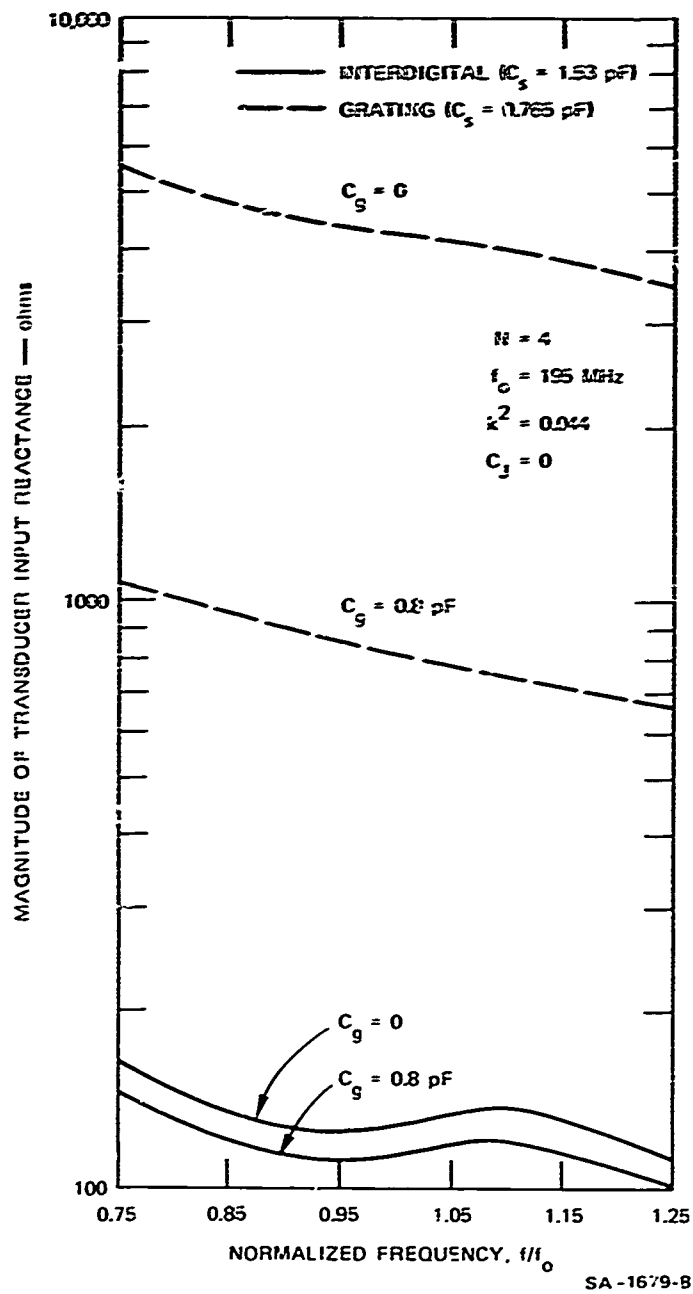


FIGURE 9 MAGNITUDE OF INPUT REACTANCE AS A FUNCTION OF FREQUENCY FOR TWO DIFFERENT VALUES OF CAPACITANCE TO GROUND — A COMPARISON OF INTERDIGITAL AND GRATING TRANSDUCERS

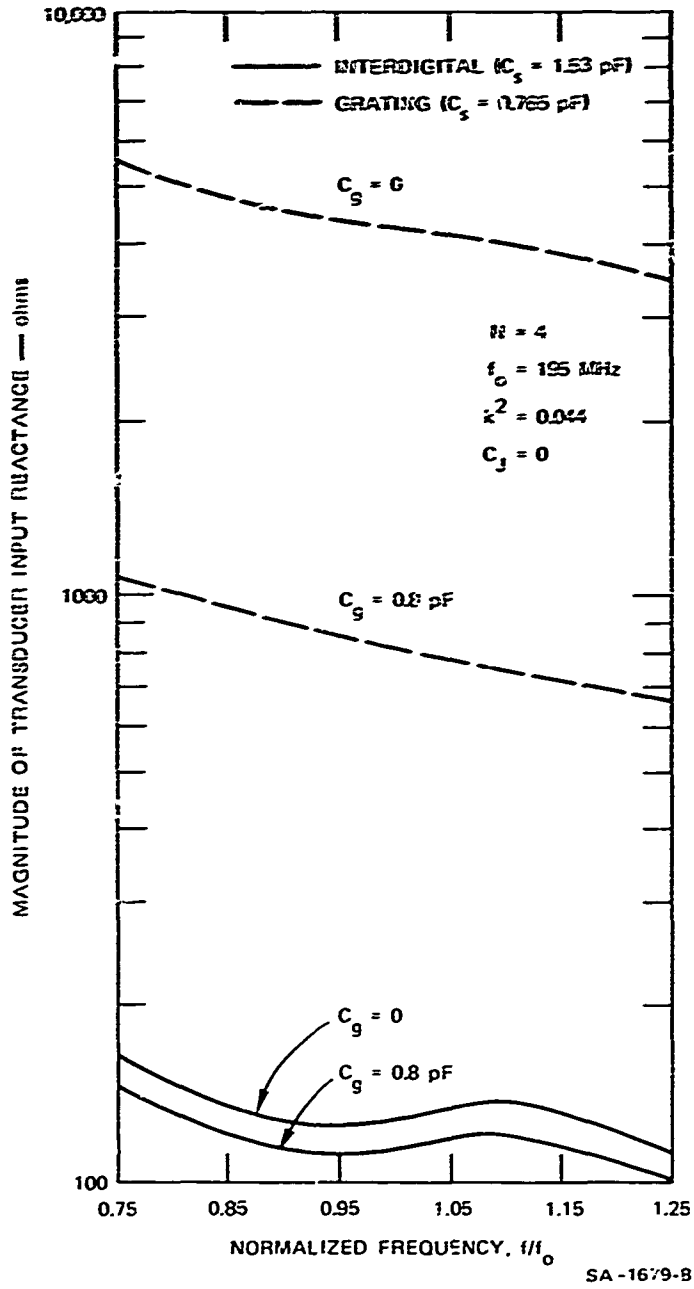


FIGURE 9 MAGNITUDE OF INPUT REACTANCE AS A FUNCTION OF FREQUENCY FOR TWO DIFFERENT VALUES OF CAPACITANCE TO GROUND — A COMPARISON OF INTERDIGITAL AND GRATING TRANSDUCERS

be solved before the grating transducer in its most simple form can be used successfully in devices.

Figure 10 compares grating and interdigital transducers with regard to the effect of an electrical load on the acoustic reflection at an acoustic port. There seems to be less acoustic reflection from a grating transducer than from an interdigital transducer, except for the case where the interdigital transducer is short-circuited. Ideally, in this case the interdigital transducer should give no reflection. It should be noted that the acoustic reflection considered here is assumed to be due entirely to electrical back-reaction and not to mass loading on the surface. The addition of capacitance to ground has very little effect on the curves shown in Figure 10 except as noted for the open-circuited grating transducer. It is interesting to note that a short-circuited grating transducer does not give zero back-reaction reflection over the whole transducer band as does a short-circuited interdigital transducer. This can be explained by noting that only the net voltage across a short-circuited grating transducer must be zero, and so individual gap voltages can be finite as long as their phases are such that they add up to zero. In a short-circuited interdigital transducer all the gap voltages must be zero.

In Figure 11 the effect of the postulated jump-over capacitance on the input resistance of a grating transducer is shown. Since it has been assumed in the model that the electric fields in this capacitor do not interact with the surface wave, the effect of this capacitor is simply to reduce the input resistance and to increase the electrical Q. Thus, under this assumption, its effect on transducer behavior is much like that of capacitance to ground.

As mentioned previously, Eqs. (14) and (15) can be used to predict the general effects of capacitance to ground. For example, the effective

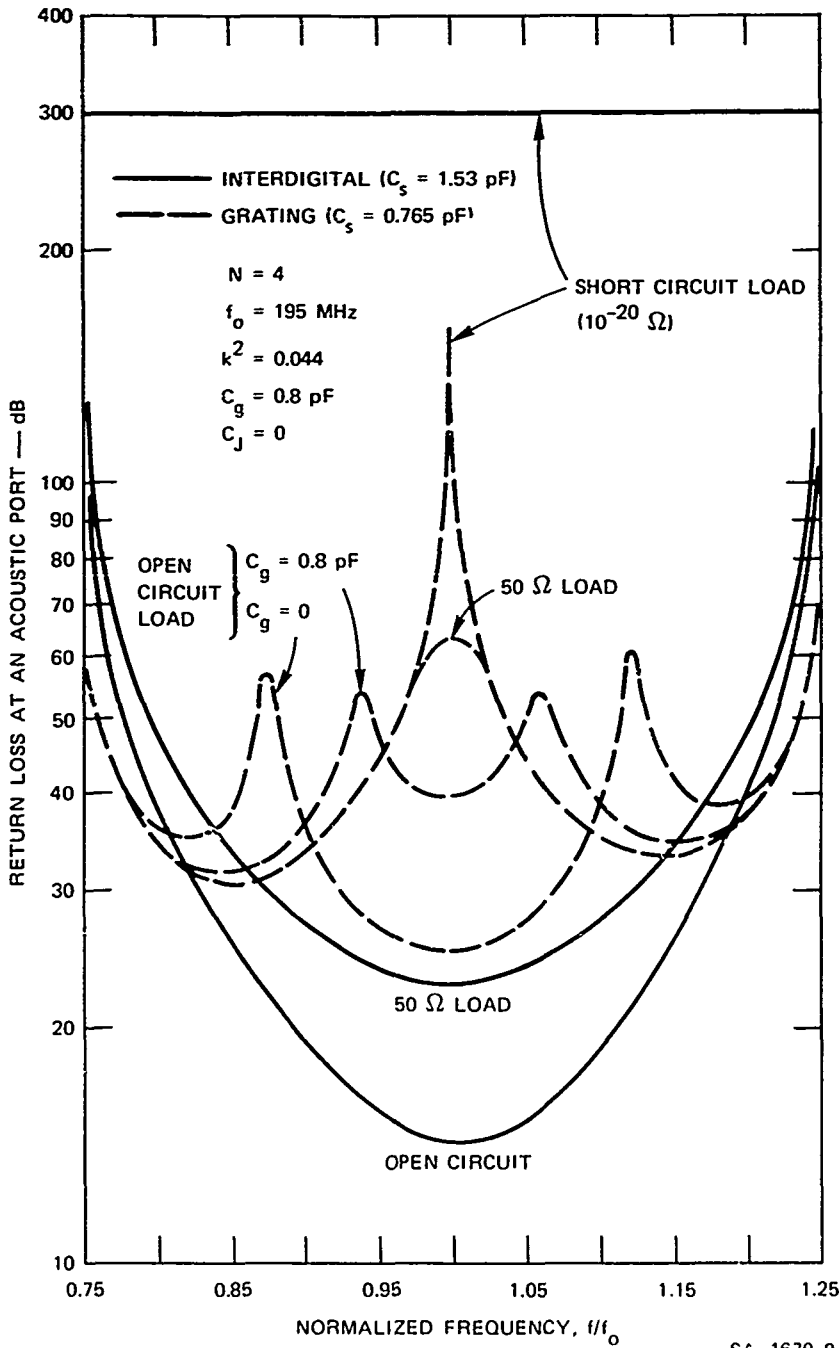


FIGURE 10 RETURN LOSS AT AN ACOUSTIC PORT AS A FUNCTION OF FREQUENCY FOR DIFFERENT LOAD CONDITIONS ON THE ELECTRICAL PORT — A COMPARISON OF INTERDIGITAL AND GRATING TRANSDUCERS

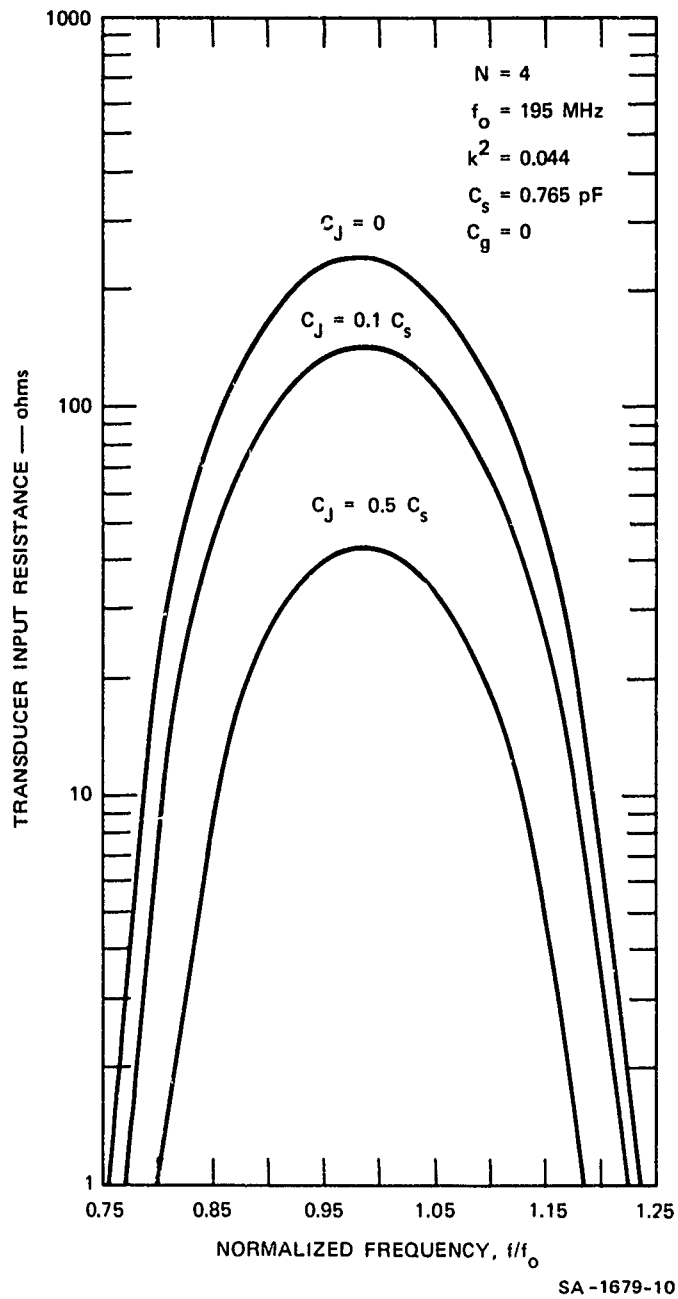


FIGURE 11 INPUT RESISTANCE AS A FUNCTION OF FREQUENCY AND "JUMP-OVER" CAPACITANCE FOR A GRATING TRANSDUCER

radiation Q can be obtained by dividing the reactance by the resistance as given in those equations. A plot of this effective radiation Q as a function of N and of capacitance to ground is shown in Figure 12. This figure again illustrates the drastic effect that capacitance to ground has on the grating transducer.

E. Experimental Measurements on Surface-Wave Transducers

1. Experimental Approach

In order to evaluate the proposed model of the grating transducer and determine the grating array's performance as a surface-acoustic-wave (SAW) transducer, detailed measurements were conducted on several different surface-wave devices. The behavior of the grating transducer was studied by two different techniques: (1) measurement of the electrical input impedance of grating and interdigital transducers (fabricated on high-electromechanical-coupling material, LiNbO_3) using a Hewlett Packard (HP) automatic network analyzer, and (2) measurement of the insertion loss between pairs of grating transducers, between pairs of interdigital transducers, and between one transducer of each kind over a wide frequency range. Both methods yield important information that is valuable in characterizing the grating transducer. It should be noted that both the grating and interdigital transducers were fabricated on each surface-wave device tested so that a direct comparison of the two kinds of transducers could be made. Since both kinds of transducer were fabricated simultaneously on the same substrate, this assured that both transducer types experienced the same processing conditions (e.g., metalization thickness, etch factors, etc.).

The measured input-admittance characteristics of interdigital transducers^{14,15} typically show quite close agreement with the values of conductance and susceptance predicted by the equivalent-circuit models

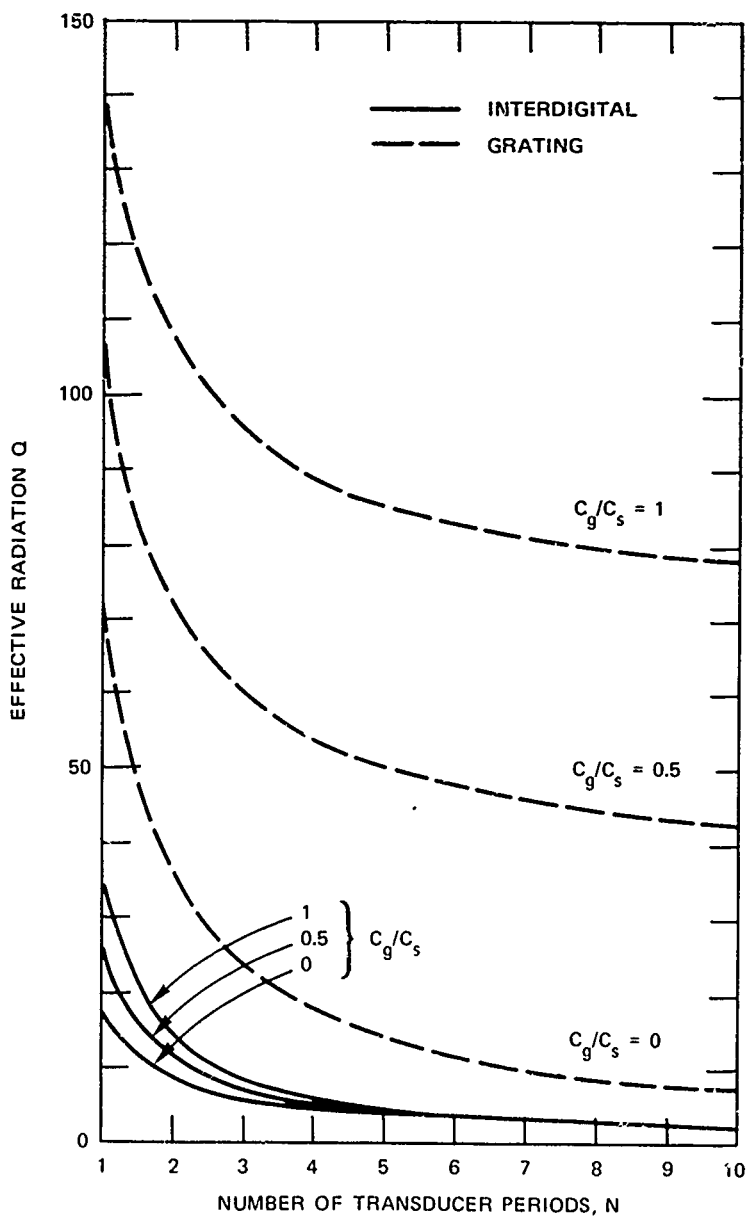


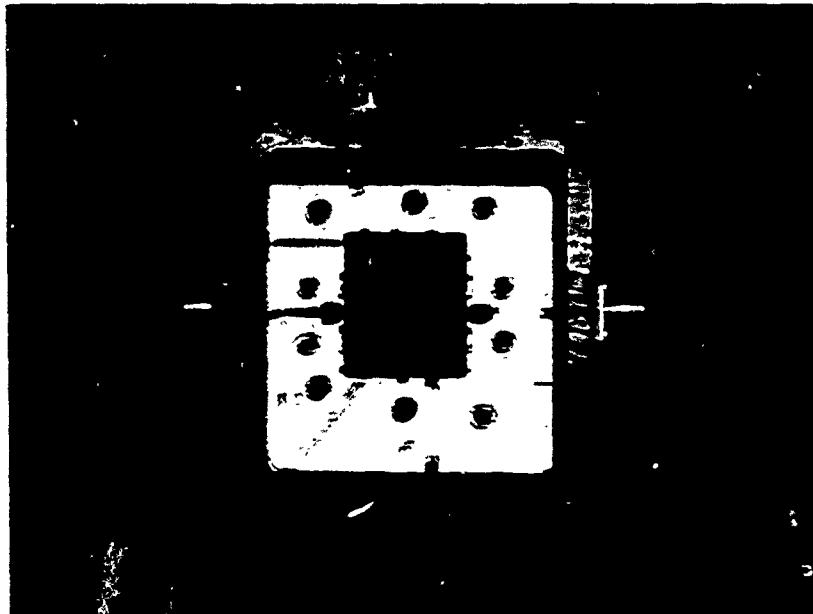
FIGURE 12 EFFECTIVE RADIATION Q AS A FUNCTION OF N , THE NUMBER OF TRANSDUCER PERIODS

of Krairojananan⁶ and Smith.⁷ At tens of megahertz, bridge measurements can be used to determine the transducer equivalent-circuit elements. However, at VHF frequencies and higher, sophisticated microwave measuring techniques can be employed to characterize a surface-wave transducer. In the present study an HP automatic network analyzer was used to perform such measurements on the surface-wave transducers being tested because of its speed and high degree of accuracy. Also the network analyzer has the ability to "calibrate out" certain kinds of parasitic elements associated with (but not part of) surface-wave transducers so that only the real transducer performance is measured.

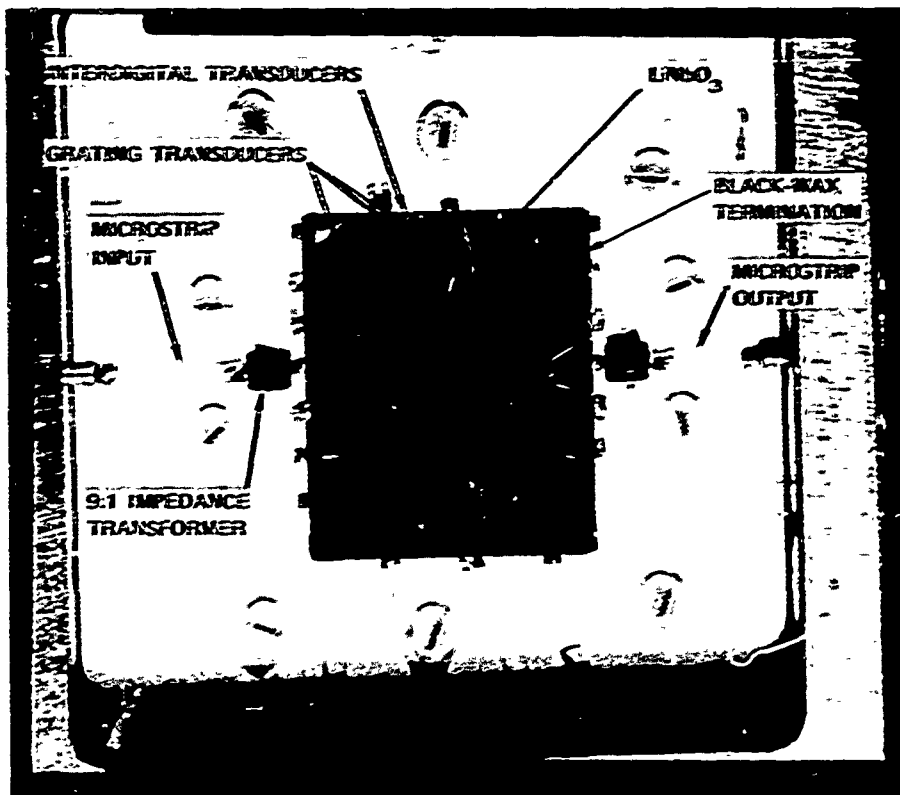
As a check on the impedance measurements and to ascertain other information not available from the CW network-analyzer measurements, pulse-transmission measurements were made on SAW devices consisting of groups of grating and interdigital transducers. These measurements were used to determine the frequency-dependent transmission characteristics of the grating transducer over a very wide frequency range and to give information on any spurious acoustic signal produced by this transducer. The surface waves and spurious modes could be separated both by resolving them in time and selectively attenuating the surface waves.

2. Test-Fixture and Transducer Design and Fabrication

Use of the HP automatic network analyzer to make input-impedance measurements on surface-wave transducers necessitates that the SAW device be embedded in an electrical test fixture for which the reference plane corresponding to the transducer terminals can be accurately determined. The test fixture designed to accomplish this task is shown in Figure 13. Here a multiport microstrip circuit board has been cut out to accommodate a rectangular lithium niobate crystal on which an array of grating and interdigital transducers is situated. The thin metallic grating and



(a) Overall view of test fixture



(b) Close-up view of LiNbO_3 surface-wave device in microstrip circuit

TA-1679-22

FIGURE 13 MULTIPOINT TEST FIXTURE FOR THE EVALUATION OF GRATING AND INTERDIGITAL TRANSDUCERS

interdigital patterns on the polished crystal surface are wire-bonded to the ends of different microstrip lines. As shown in Figure 13(b) the interdigital transducers are connected directly to the 50-ohm microstrip, while the grating transducers are attached to the microstrip through a 9:1 impedance transformer (the reason for this will be discussed below). Also noticeable in the photograph is a thin layer of black wax on the crystal's edge that is utilized to terminate the acoustic waves and prevent spurious reflections.

Measurements that are done using the HP automatic network analyzer are normally referred to a 50-ohm system. When the impedance to be measured is highly reactive and greater than a few hundred ohms, the measurement accuracy, especially for the real part of the impedance, becomes poor. The grating transducer presents this type of load impedance.

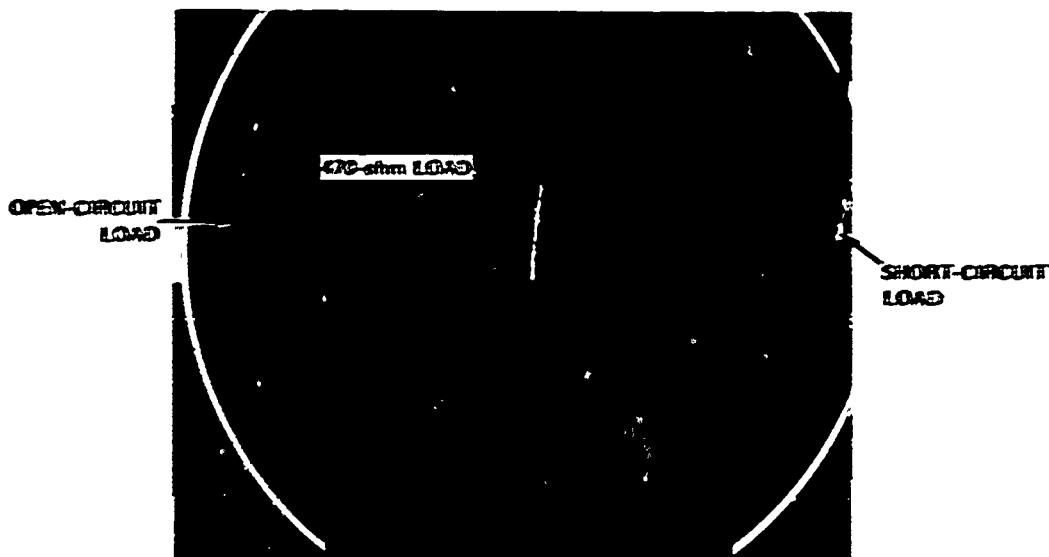
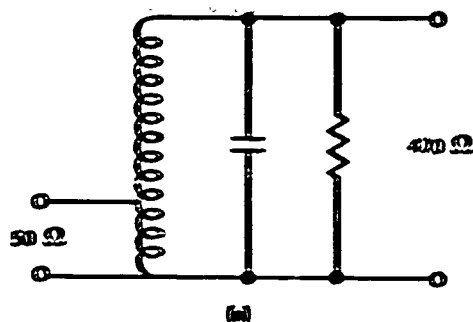
In such a situation it is possible to improve the measurement accuracy by inserting a transformer between the network analyzer and the high-impedance load. This effectively allows the measurements to be performed in a higher-impedance system.

Ideally, one would like to use a transformer with transformation properties that are frequency-independent so that one can make measurements of the unknown load impedance over a wide frequency band. In practice all transformers exhibit some frequency-dependent behavior. Fortunately, because of the tremendous power of the automatic network analyzer, it is possible to calibrate out this frequency-dependent behavior so that the transformer becomes effectively very nearly ideal. To do this, one simply calibrates the system by placing a good load, short, and open on the high-impedance side of the transformer. The value for the load would be equal to the impedance level of the high-impedance side. The measurements of the load, short, and open used to calibrate

the analyzer are referred to calibrated standards, and thus the frequency variations caused by the transformer in the microstrip are considered by the analyzer to be system errors. The analyzer then stores these system errors and applies appropriate corrections to all subsequent measurements. In other words, as far as the network analyzer is concerned, the non-ideal behavior of the transformer is equivalent to other system errors—e.g., errors that might be caused by poor directivity in a directional coupler inside the analyzer. It should be noted that the analyzer is not capable of providing a perfect correction for any amount of non-ideal behavior in the transformer. The worse the behavior of the transformer, the poorer the accuracy will be.

For the measurement of the grating transducers, a small transformer was built having a 9:1 impedance-transformation ratio. The design of the transformer was obtained by trial and error. The equivalent circuit for the transformer is shown in Figure 14(a). The major design requirement for the transformer is that the number of turns be adjusted so that the shunt capacity on the high-impedance side produces resonance at the desired frequency of operation. In order to keep the transformer small it was wound on a two-hole ferrite core^{*} using No. 35 gauge copper wire (see Figure 13). It was found that twelve turns in the secondary and four turns in the primary produced resonance at about 180 MHz. The experimental transformer characteristics are illustrated in Figure 14(b). This figure is a Smith-chart plot of admittance, showing the characteristics for an open-circuit, short-circuit, and 470-ohm load on the high-impedance side of the transformer. The frequency range is 150 to 250 MHz. It can be seen that the transformer provides a good match between 50 and 470 ohms at resonance. Also from the measurement with an open

* Manufactured by Siemens, Type M145 U60.



SA-1579-21

FIGURE 14 TRANSFORMER EQUIVALENT CIRCUIT AND MEASURED CHARACTERISTICS

circuit on the high-impedance side it can be seen that losses in the transformer are negligible.

The transformer exhibits considerable frequency variation (it is a parallel resonant circuit). Figure 15 illustrates the effectiveness of the automatic network analyzer in calibrating out this frequency variation. This figure is a polar plot of the reflection coefficient of a 470-ohm load (1/8-watt carbon resistor) measured with the calibrated system. The outer circle corresponds to a reflection-coefficient magnitude of 0.05. (The Smith-chart coordinates should be disregarded



SA-1679-20

FIGURE 15 POLAR PLOT OF THE REFLECTION COEFFICIENT OF A 470-OHM LOAD MEASURED WITH TRANSFORMER FREQUENCY VARIATIONS CALIBRATED OUT (110 to 310 MHz)

in this figure.) The frequency range is 110 to 310 MHz. The clustering of the points means that the load is effectively constant over the whole measurement frequency range. This fact would be dramatically illustrated if these points were to be plotted in Figure 14(b), since the outer circle in that figure corresponds to a reflection-coefficient magnitude of 1.0. Thus, all the points in Figure 15 would lie at the center of the chart in Figure 14(b) and the transformer would appear to be ideal.

Figure 16 shows schematically the experimental configuration of grating and interdigital transducers used to characterize the grating transducer. The substrate utilized in this experiment was a lithium niobate Y-cut, Z-propagating (YZ) crystal with the top surface optically polished free of scratches and pits. The substrate was 25 mm by 3 mm by 2 mm in the X, Y, Z directions and accommodated 16 individual transducers on its surface. The mask used to produce the patterns had rows of five-period grating, four-period interdigital, and three-period grating transducers, all aligned to within 1 minute of arc. This

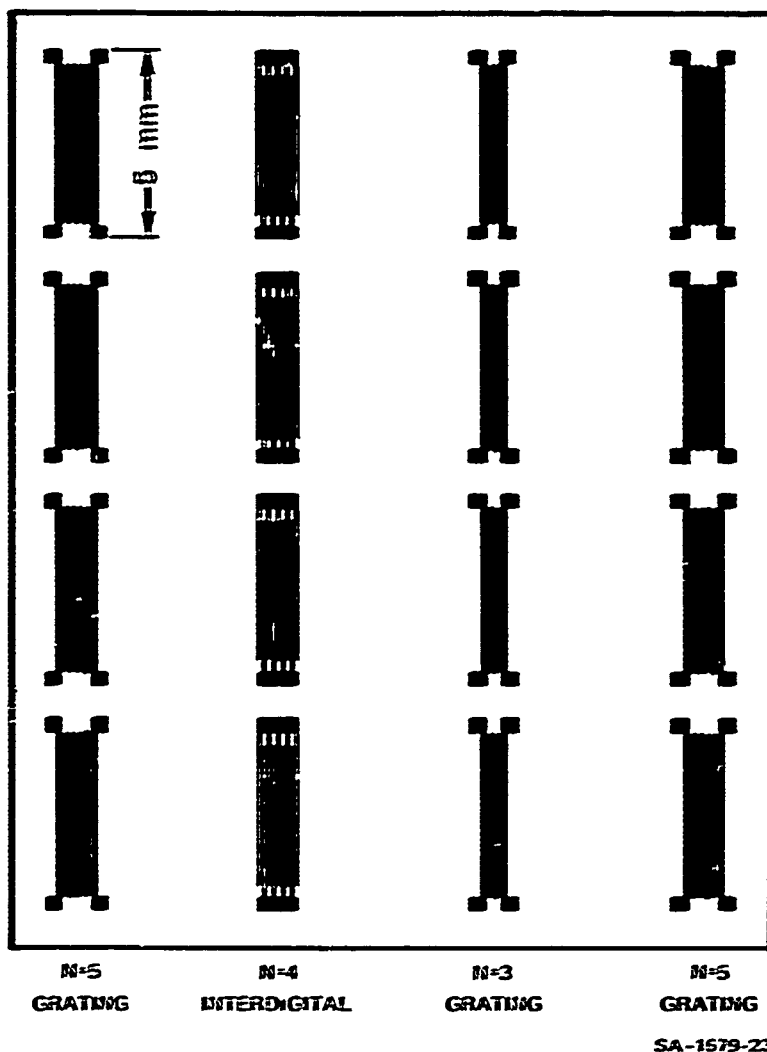
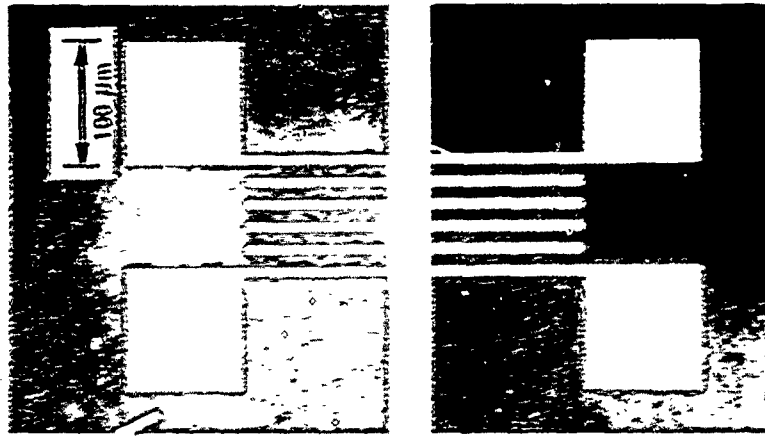


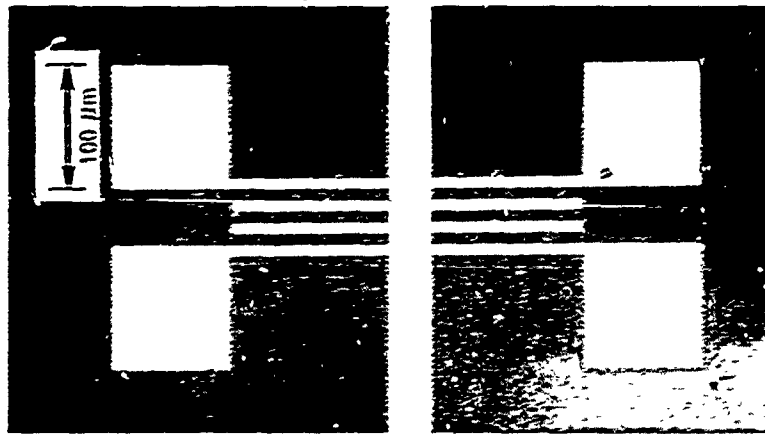
FIGURE 16 EXPERIMENTAL CONFIGURATION USED FOR MEASURING THE CHARACTERISTICS OF A GRATING TRANSDUCER AT 190 MHz

permitted a pair of identical transducer patterns to be fabricated at either end of the LiNbO_3 with one column of each of the other two patterns in the middle. For example, $N = 5$ gratings appear at the edge of the substrate illustrated schematically in Figure 16. Thus, moving the mask by one pattern allowed either $N = 5$ or $N = 3$ grating transducers to be placed at the crystal edge.

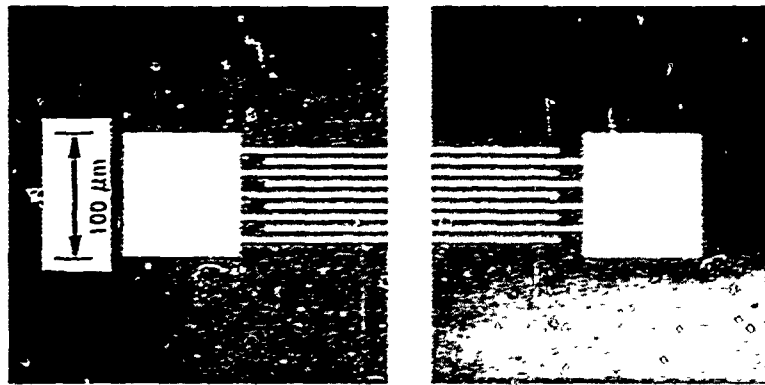
Photographs of the thin (1500-\AA -thick) aluminum grating and interdigital surface-wave-transducer patterns are shown in Figure 17.



(a) Five period grating.



(b) Three period grating.



(c) Four period interdigital.

FIGURE 17 PHOTOGRAPHS OF ALUMINUM TRANSDUCER PATTERNS ON Y-CUT, Z-PROPAGATING LiNbO_3

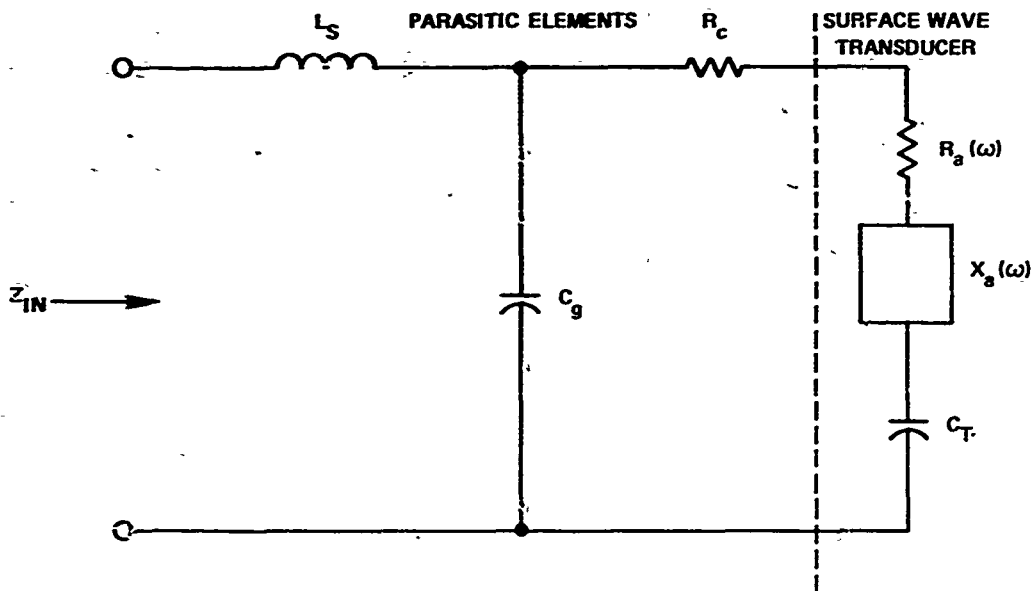
These patterns correspond to the ones shown in Figure 16 for the three different transducers. The five-period and three-period grating transducers have five and three coupling gaps, respectively, with one-wavelength spacing between the centers of adjacent gaps. On the other hand, the four-period interdigital transducer has eight coupling gaps, but these are spaced one-half acoustic wavelength apart at the synchronous frequency. The period of all transducers used is 18 μm , which corresponds to a theoretical synchronous operating frequency of 190 MHz on YZ LiNbO_3 . The transducer-pad area is kept small (0.01 mm^2) in order to reduce the capacitance to ground of the connections, but not so small that it does not leave adequate area to allow the bonding of wire leads. The transducer patterns were very wide, being 5 mm (or 280 wavelengths) transverse to the propagation direction. This was done to increase the capacitance per period C_s of the grating structure, since C_s is linearly proportional to the finger length. However, this long finger length caused all of the transducer structures to exhibit appreciable ohmic loss, and this had to be taken into account in the interpretation of the measurements.

The transducers were fabricated using standard surface-wave transducer photolithographic techniques. Shipley AZ-1350 positive photoresist and chemical etching were used to produce the transducers, and both gold and aluminum patterns were tested to determine any differences that might occur due to (1) mass loading or, (2) slightly different film conductivities. In the final surface-wave devices tested on the network analyzer the transducer patterns appeared to be of excellent quality, being free of any shorts or opens. In fact all sixteen aluminum transducer patterns (covering almost one square inch) were of uniformly high quality. This demonstrates that the photolithographic techniques used were adequate for producing the thinnest lines required for the interdigital transducer ($4.5 \mu\text{m}$) and thus that the measurements were probably free from constructional artifacts.

3. Experimental Results

The first way chosen to investigate the characteristics of the surface-acoustic-wave transducers was to make electrical-input-impedance measurements on each transducer type over a range of frequencies centered about its synchronous frequency. The measured impedance values can thus be compared to those obtained from the equivalent-circuit models for interdigital and grating transducers (see Sections II-B and II-C). The input-impedance measurements were made using an HP automatic network analyzer in its automatic mode. The test fixture used for this measurement, shown in Figure 13, permits a very accurate determination of reference-plane position. The test fixture is constructed so that the three required calibration terminations (load, short, and open) may be implemented right at the point of attachment of the transducer bond wire. For the case of the grating transducer, the calibrations are carried out on the side of the transformer nearest the transducer. As was explained above, these calibration data are retained by the computer and subtracted out of subsequent measurements that are made when the grating transducer is attached to this port. The interdigital transducers (being of lower impedance than the grating) are connected directly to the 50-ohm microstrip transmission line.

In order to aid the interpretation of the results to be presented, a one-port series equivalent circuit for a surface-wave transducer is presented in Figure 18. The appropriate circuit elements are defined in that figure. Measurements made of the input impedance Z_{in} will be compared to predicted values of $R_a(\omega)$ and $X_a(\omega)$ that have been suitably modified to take into account the effects of capacitance to ground C_g and series inductance L_s .



- WHERE
- L_S = Series inductance of the bond wires
 - C_g = Capacitance to ground of the transducer and pad
 - R_c = Ohmic resistance of the thin transducer electrodes
 - C_T = Transducer static capacitance
 - $R_a(\omega)$ = Acoustic radiation resistance of the transducer
[i.e., the quantity given in Eqs. (14) and (15) with $C_g = 0$]
 - $X_a(\omega)$ = Acoustic radiation reactance of the transducer,
and equals zero at synchronism

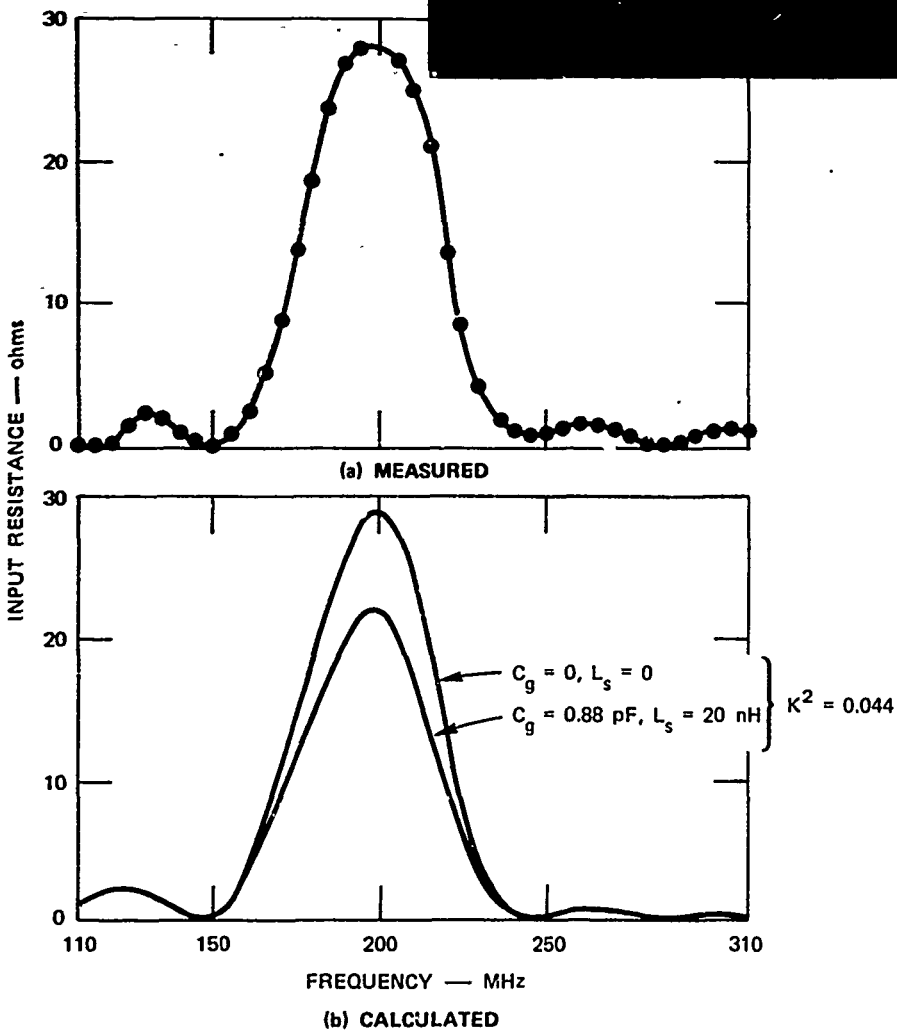
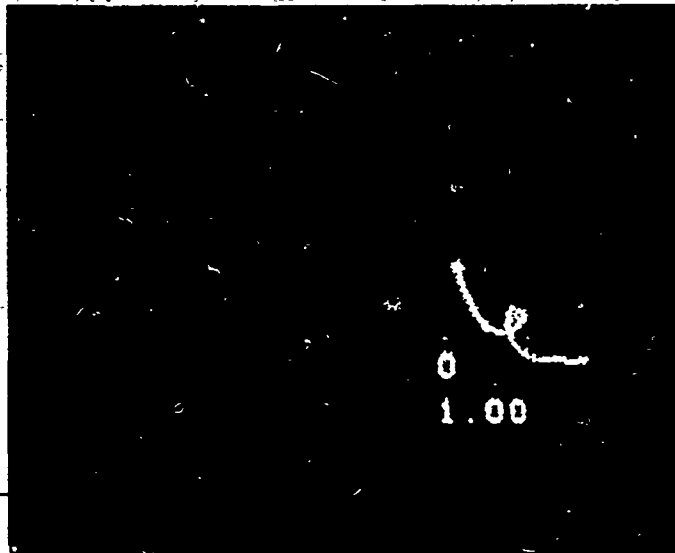
SA-1679-39

FIGURE 18 EQUIVALENT SERIES CIRCUIT REPRESENTATION FOR EITHER GRATING OR INTERDIGITAL SURFACE-WAVE TRANSDUCERS

a. Input Impedance of Interdigital Transducers

Figure 19 presents the measured and calculated real part of the input impedance for one 5-mm-wide, four-period interdigital transducer [shown in Figure 17(c)]. The measurements of the real part of Z_{in} are plotted in Figure 19(a) as taken from a direct X-Y display of this quantity on the network analyzer. The actual measurement interval extended from 110 MHz to 310 MHz, with measurements being taken in 2-MHz steps. This provides adequate resolution to show the resistance peak and the first sidelobes in detail. A Smith-chart presentation of the input impedance of the $N = 4$ interdigital transducer over the same frequency range is shown in the insert of Figure 19, where the center of the chart corresponds to an impedance of 50 ohms. Both the characteristic main acoustic loop at the synchronous frequency and the broadband background resistance (of 100 ohms) due to the finite finger resistivity is evident in this picture. The circuit is tending to resonance due to the two long (1.1 mm), thin (0.7 mil diameter) bond wires used to attach this transducer to the microstrip circuit.

Computer calculations (using Smith's model)⁷ of the real part of the input impedance are displayed in Figure 19(b) over the same 110-to-310-MHz frequency range. The resistance plot is shown for two cases: (1) no series inductance and capacitance to ground, and (2) for $L_s = 20$ nH and $C_g = 0.88$ pF. The value of $C_g = 0.88$ pF was determined from an independent measurement of the stray transducer capacitance to ground. This measurement was made on a dummy transducer pattern whose ground pad was left open-circuited. The series-inductance value of 20 nH was obtained from a measurement of the frequency at which the lead inductance resonates with the transducer capacitance and the capacitance to ground. It should be noted that for comparison purposes the constant background resistance of approximately 100 ohms has been subtracted from



SA-1679-25

FIGURE 19 COMPARISON OF (a) MEASURED AND (b) CALCULATED INPUT RESISTANCE OF A FOUR-PERIOD INTERDIGITAL TRANSDUCER

the measured data. Figures 20(a) and (b) show a comparison of the measured and calculated input reactance of the transducer for the case of no stray parasitic elements and for the case using the measured values of $C_g = 0.88$ pF and $L_s = 20$ nH.

In making the comparison between measurements and computations it is seen that the inclusion of 0.88 pF for the capacitance to ground reduces the computed input resistance below the measured value. On the other hand, the inclusion of this amount of capacitance to ground seems to be necessary to make the computed and measured input reactances agree. However, it should be noted that the equivalent-circuit calculation assumed a capacitance per period C_s of 1.53 pF for the 5-mm-long fingers. This capacitance is an empirical value for interdigital transducers on Y-cut, Z-propagating lithium niobate that was obtained from Gerard et al.¹⁶ If the value assumed for C_s was incorrect it could possibly account for the observed discrepancy.

The relatively good agreement over a wide frequency range between the calculated and measured input impedance (see Figures 19 and 20) of this interdigital transducer promotes confidence in the measurement technique and illustrates the validity of this approach in characterizing surface-wave transducers in general. By using measured values for the stray parasitic elements and measuring the input resistance and reactance, a verification of the assumed transducer model can be obtained.

b. Input Impedance of Grating Transducers

Input-impedance measurements similar to the ones made on the interdigital transducer were carried out on both the five-period and three-period grating transducers, the only difference between the two measurement techniques being that the grating transducer was attached to the network analyzer through a 9:1 impedance transformer. The measured

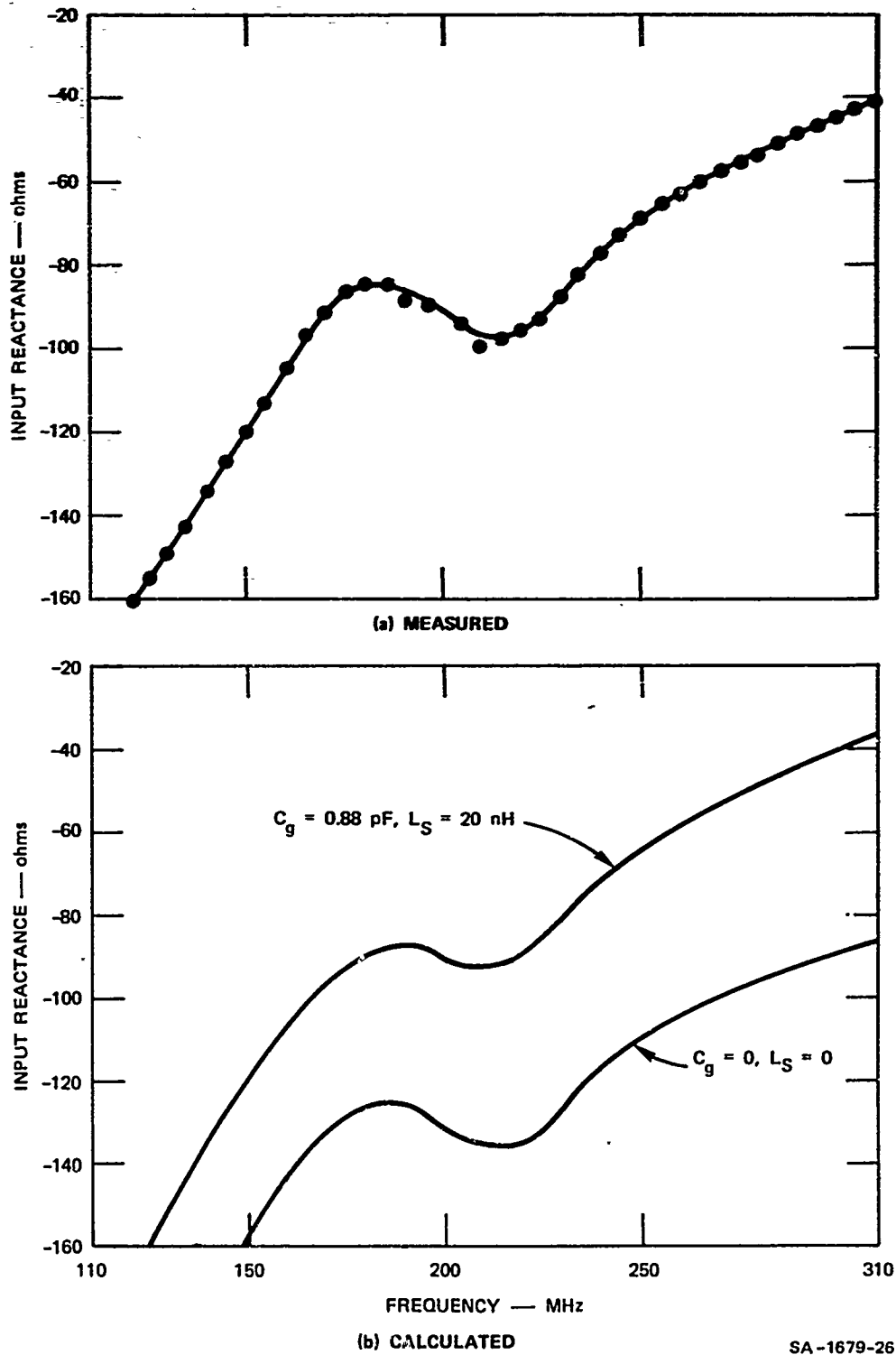
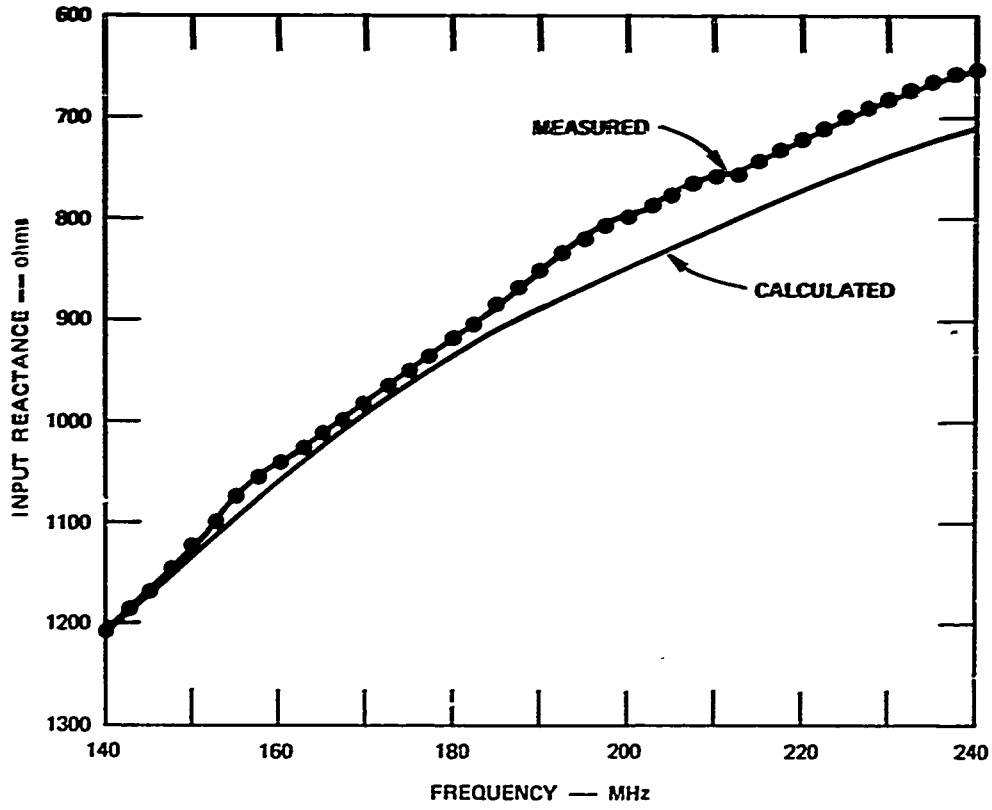
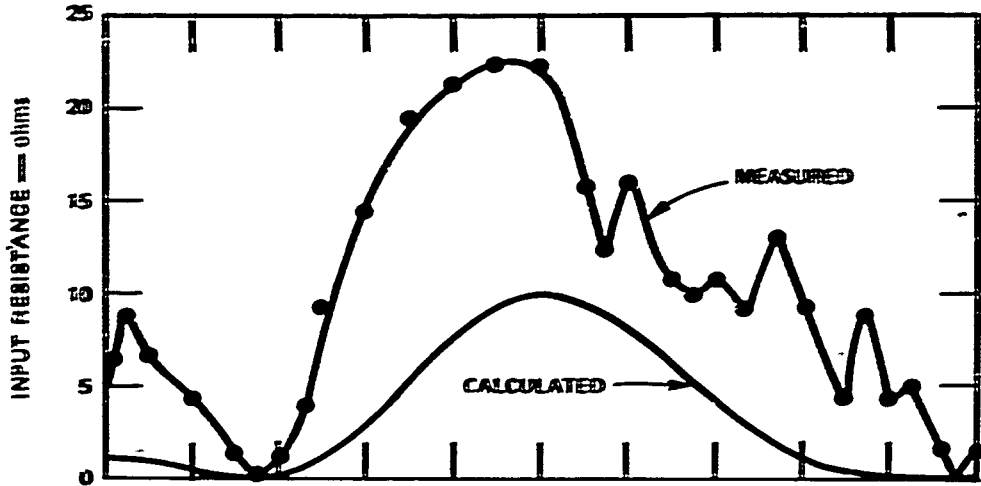


FIGURE 20 COMPARISON OF (a) MEASURED AND (b) CALCULATED INPUT REACTANCE OF A FOUR-PERIOD INTERDIGITAL TRANSDUCER

and calculated input resistance and reactance of the $N = 5$ grating transducer are displayed in Figures 21(a) and (b), respectively, over the frequency range 140 MHz to 240 MHz. The impedance measurements were made at 2-MHz intervals over the indicated 100-MHz range. The equivalent-circuit model that was used to calculate the characteristics of the grating transducer is the one developed in Section II-D. In this model the capacitance per period of the grating is assumed to be 0.765 pF, which is one-half that of the interdigital transducer. Also, the measured capacitance to ground of the grating, $C_g = 0.780$ pF, is used and the inductance is assumed to be negligible (due to the very short bond-wire lengths used). The model accounts for both the acoustic-impedance discontinuity due to the metallic film (approximately 1500-Å-thick gold) and the unequal finger and gap widths that existed in the $N = 5$ grating transducer. In this case, however, the model did not include any jump-over capacitance or acoustic-wave coupling due to jump-over fields. In the plot of input resistance, the background resistance of 126 ohms has been subtracted out of the measured data so that the calculated and measured values can be compared more easily. It is seen from Figure 21(a) that the overall shape of the measured input resistance matches that of the calculated curve, with the central peaks occurring at nearly the same frequency and the lower-sidelobe frequencies and the frequencies at which resistance minima occur agreeing. However, the measured value of the input resistance appears to be too large. This fact could be explained if some of the measured input resistance represented coupling to bulk waves or to surface waves generated by jump-over fields. Either one of these effects would tend to raise the input-resistance curve above the computed value. On the other hand, the computed input reactance [see Figure 21(b)] of the $N = 5$ grating agrees quite closely with the measured values. This fact lends credibility to the overall grating-transducer model. The results of the input-impedance



SA-1679-27

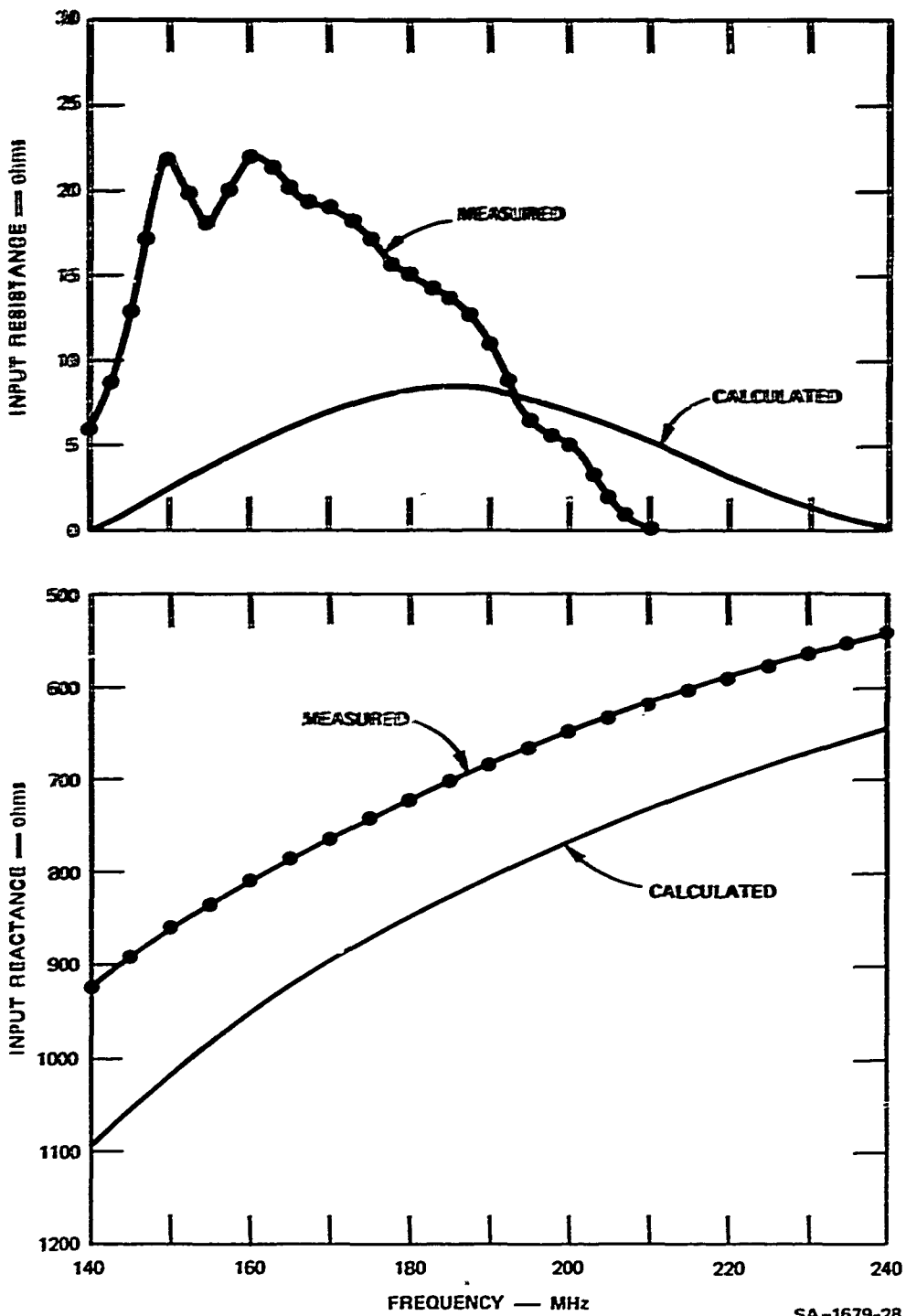
FIGURE 21 COMPARISON OF CALCULATED AND MEASURED INPUT IMPEDANCE OF A FIVE-PERIOD GRATING TRANSDUCER

measurement will be seen to match up quite well with the broadband insertion-loss measurements that were made on the same device.

The measurement of input impedance was repeated for the $N = 3$ grating transducer. The calculated and measured values of input resistance and reactance are displayed in Figure 22(a) and (b), respectively. In this instance, the transducers were made using aluminum approximately 1500 \AA thick. The capacitance per period and the capacitance to ground were assumed to be the same for this transducer as for the $N = 5$ grating transducer. A shift of the input resistance peak to a frequency lower than the expected value is observed. As with the $N = 5$ grating transducer, the maximum resistance measured (with the background electrode resistance of 170 ohms subtracted out) is higher than that calculated from the model. The agreement between measured and calculated transducer reactance is less for the $N = 3$ case than it was for $N = 5$. The reactances could be made to match more closely by adding some series inductance in the model; however, it is more likely that the calculated capacitance per period of the transducer should be made larger (thus lowering the reactance) to take account of end effects and jump-over effects. In fact, both of the discrepancies between measured and calculated input impedance for this case are probably due in part to the neglect of the capacitance and coupling of the jump-over field along with the end effects that occur in this short $N = 3$ transducer structure. The pulsed-transmission measurements made on the $N = 3$ grating that are described below will be seen to generally correspond to the observed behavior of the measured input resistance.

c. Insertion Loss and Pulse Response of Grating Transducers

To obtain further information on the grating transducer and determine the reasons for the discrepancy between the measured and calculated input impedance, insertion-loss measurements were carried out



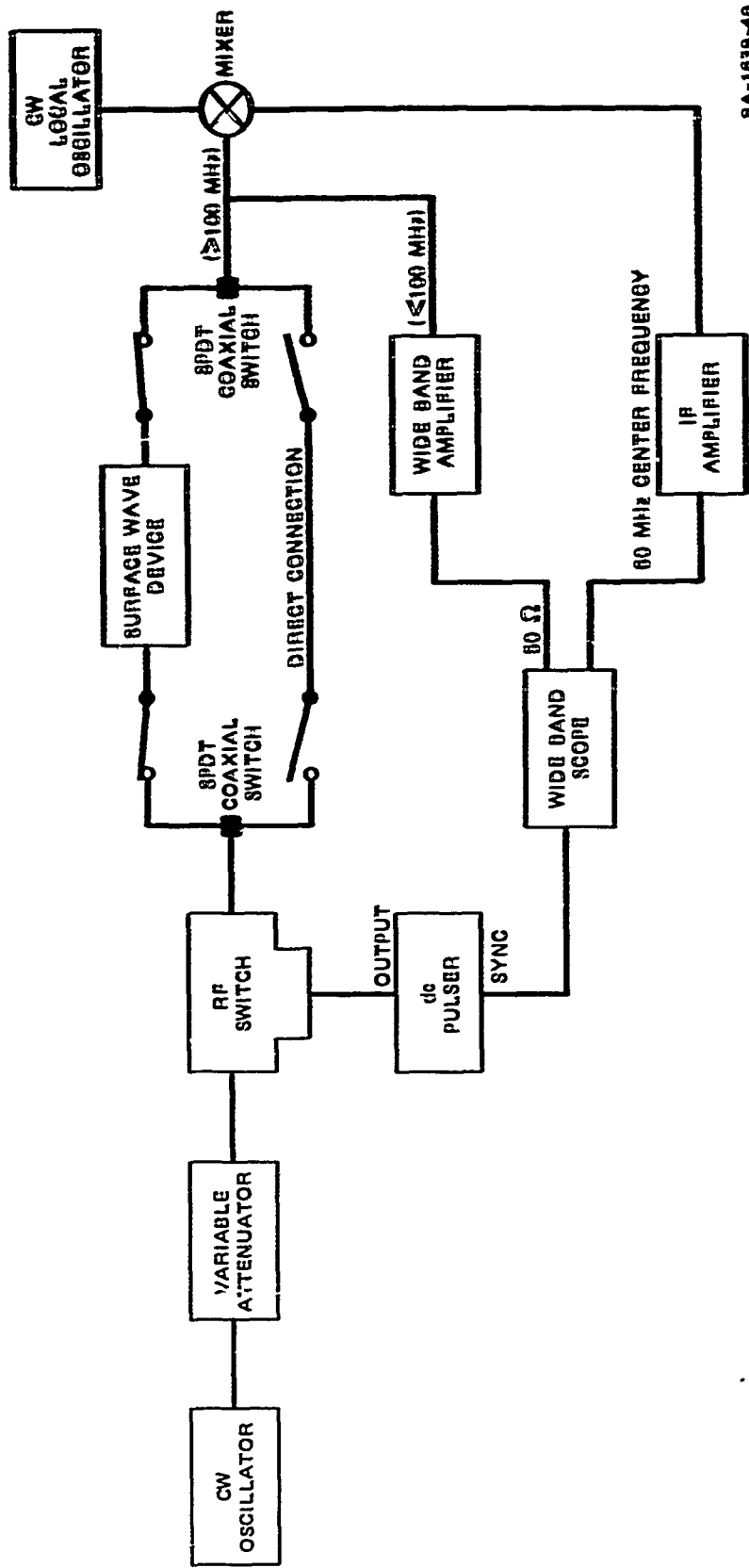
SA-1679-28

FIGURE 22 COMPARISON OF CALCULATED AND MEASURED INPUT IMPEDANCE OF A THREE-PERIOD GRATING TRANSDUCER

over a very broad frequency range using the substitution method. The tests were carried out using the arrangement shown schematically in Figure 23. The dc pulser controls the RF switch to generate RF pulses on the order of 0.75 μ s in length. The pulse, the amplitude of which is set by the variable attenuator, passes through the surface-wave device under test and the output reference level is recorded. The SPDT coaxial switch is then used to disconnect the test device and substitute a through connection. The variable attenuator is adjusted to produce the same output reference level and the difference in attenuator settings gives the insertion loss of the device under test. At frequencies above 100 MHz, a heterodyne detection scheme (with an IF frequency of 60 MHz) is used, while below 100 MHz the pulses are displayed directly on a wideband oscilloscope after appropriate amplification.

The results of the broadband untuned-insertion-loss measurement are shown in Figures 24 and 25 for the cases of transmission between two $N = 5$ grating transducers and between two $N = 3$ grating transducers, respectively. The magnitude of the insertion loss has been normalized to 40 dB, since the absolute value is of little significance because of the high resistive losses within the transducers and the transformer coupling to the transducers. What is apparent in these figures is the unexpected surface-wave transduction that takes place over a broad band of frequencies centered about a number of discrete frequency points. During the measurements great care was taken to ensure that the observed delayed pulse was due to surface-wave transduction and not to bulk modes. This was verified by (1) checking the time delay τ of the received pulse to make sure it agreed with the expected delay

$$\tau = \frac{l}{v_s} \quad (16)$$



8A-1679-40

FIGURE 23 SCHEMATIC DIAGRAM OF TEST SET-UP USED TO MEASURE INSERTION LOSS AND PULSE RESPONSE OF SURFACE-WAVE DEVICES

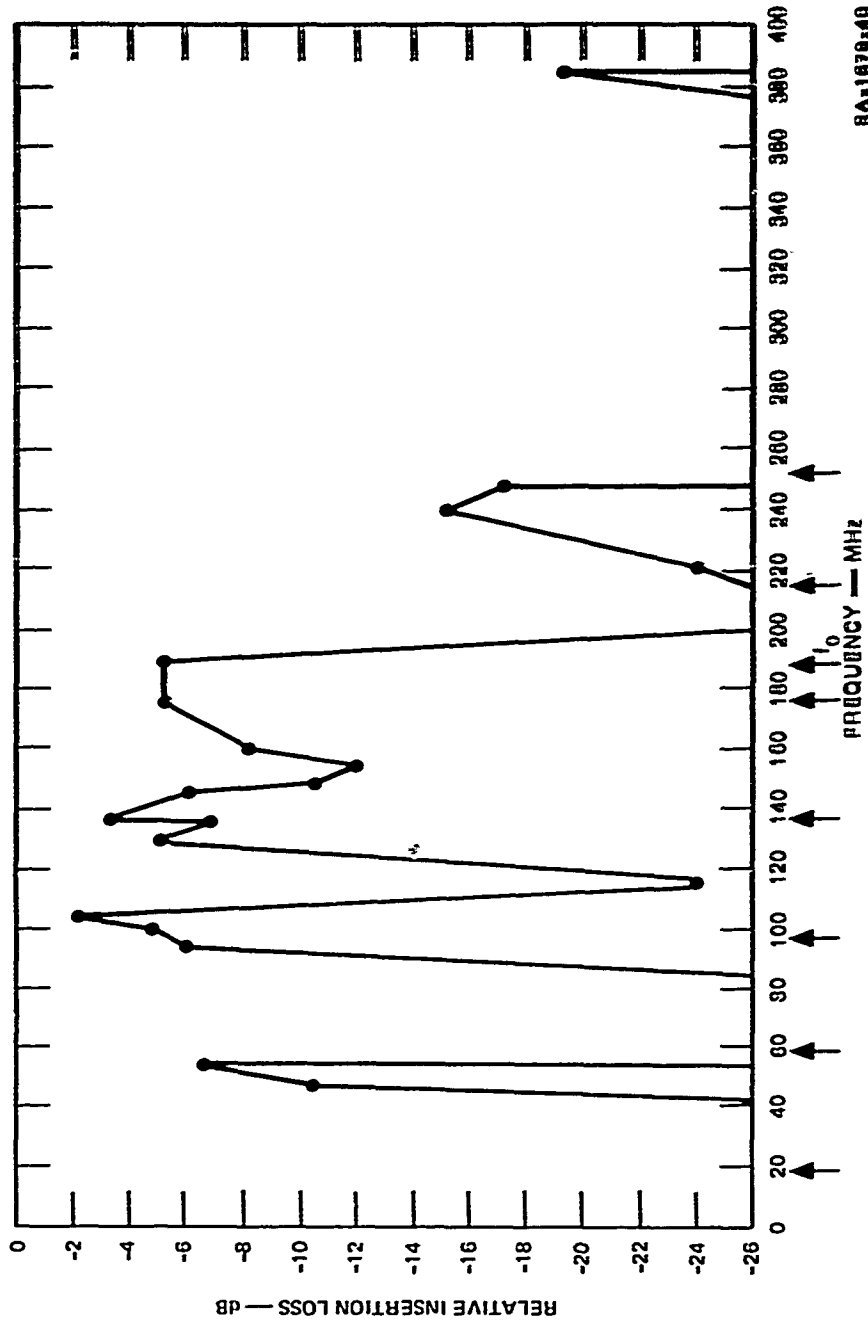


FIGURE 24 RELATIVE UNTUNED SURFACE-WAVE INSERTION LOSS (response) BETWEEN TWO FIVE-PERIOD GRATING TRANSDUCERS. The arrows indicate the frequencies at which coupling to the "jump-over" fields might exist. The frequency f_0 is the fundamental frequency of the grating mode.

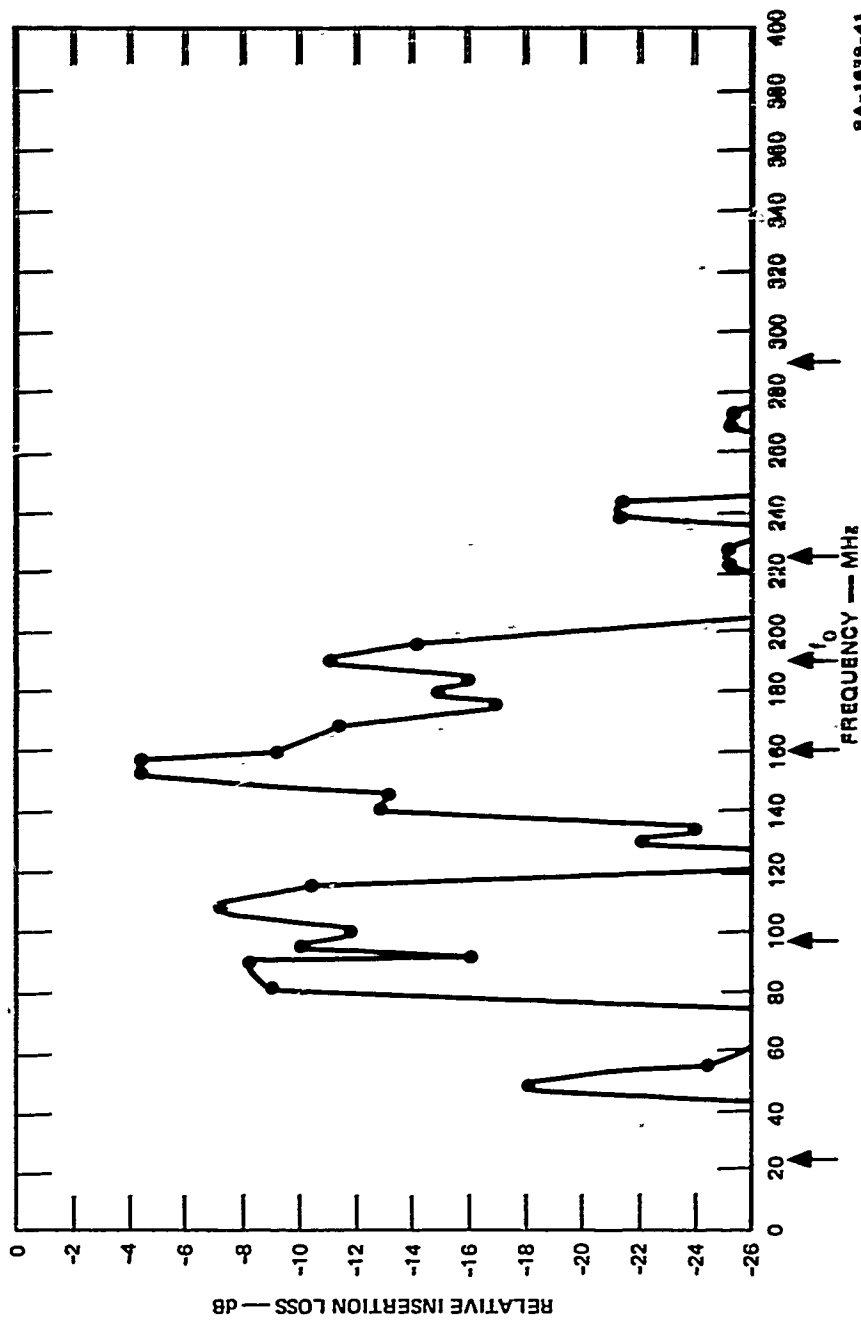


FIGURE 25 RELATIVE UNTUNED SURFACE-WAVE INSERTION LOSS (response) BETWEEN TWO THREE-PERIOD GRATING TRANSDUCERS. The arrows indicate the frequencies at which coupling to the "jump-over" fields might exist. The frequency f_0 is the fundamental frequency of the grating mode.

where ℓ is the separation between sending and receiving transducers and v_s is the surface-acoustic-wave velocity, and (2) selectively attenuating the surface wave by placing moisture (human breath) on the crystal's surface.

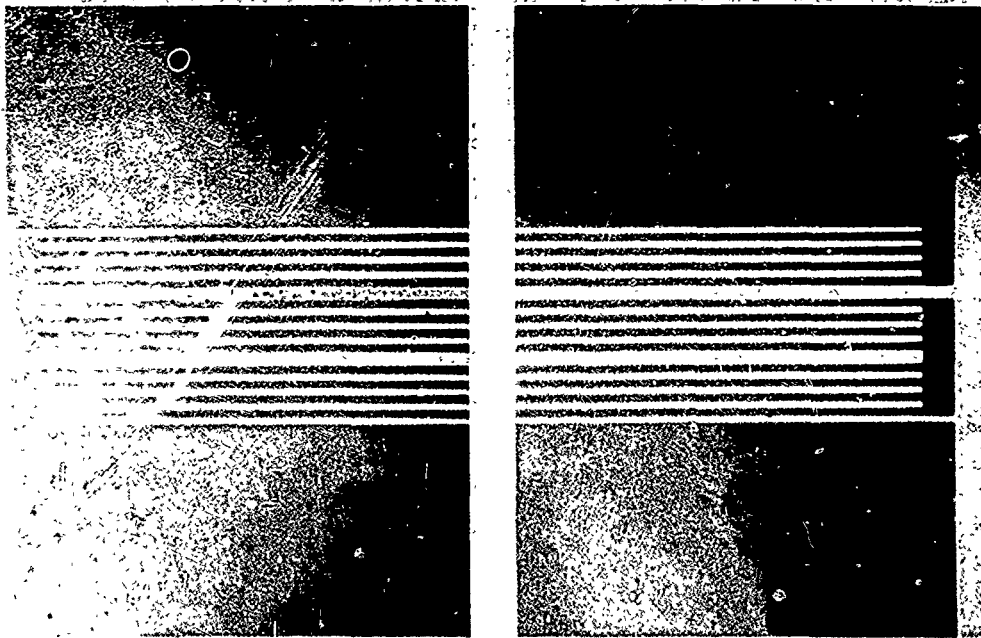
The unusual surface-wave response below the synchronous frequency of both the $N = 5$ and $N = 3$ grating transducers might be explained if one assumed there is a component of electric field that extends from the two end (driven) electrodes through the crystal--i.e., a component that "jumps over" all the floating electrodes (see Figure 1). Under this assumption there is now a second component of spatially varying electric field that has a period equal to twice the center-to-center spacing of the driven electrodes of the grating transducer. The frequencies at which surface-wave coupling might exist for this jump-over field are indicated in Figures 24 and 25 as arrows on the frequency scale. The periodicity of this field for the $N = 5$ grating is $180 \mu\text{m}$. This corresponds to a fundamental frequency of 19.33 MHz, with the third, fifth, seventh, and ninth harmonics occurring at 53 MHz, 96.65 MHz, 135.3 MHz, and 173.4 MHz, respectively. These frequencies are indicated as arrows in Figure 24. For most of these harmonics substantial transmission responses are noted, thus indicating that coupling does exist between surface waves and the fields that span the end electrodes. The $N = 3$ grating should behave in a similar manner, with the exception that end effects from a transducer having so few periods may be more prominent. The period of the jump-over electric field for the three-period grating is $108 \mu\text{m}$, which corresponds to 32.2 MHz, 96.6 MHz, 161 MHz, and 255 MHz for the first, third, fifth, and seventh harmonics, indicated as arrows in Figure 25. Again the correlation that exists between the multiple frequency responses and the proposed surface-acoustic-wave coupling due to jump-over fields appears to be quite strong. In view of this argument, the observed magnitude of the peak

in radiation resistance for the $N = 3$ grating transducer at 165 MHz (Figure 22) is probably due to surface-wave excitation by both the jump-over fields and the grating fields between the floating electrodes.

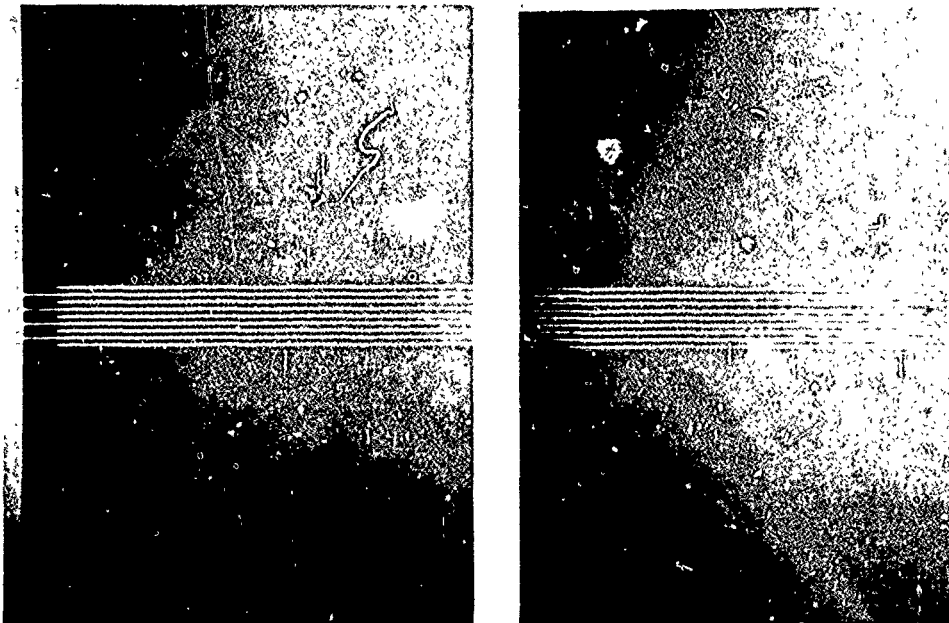
The relative untuned surface-wave insertion loss was also measured between a five- or three-period grating transducer and a four-period interdigital transducer. The frequency responses should correspond to the responses for $N = 5$ and $N = 3$ grating transducers that have been filtered by the transmission characteristic of an interdigital transducer. The measured and theoretical zeros of transmission were found to agree quite well, and the large surface-wave signal level that was observed in the sidelobes is consistent with the postulation of surface-wave excitation by jump-over fields between the end electrodes.

d. Measurements on Multi-Section or "Hybrid" Grating Transducers

The excitation and detection of surface acoustic waves by grating transducers have been further investigated by fabricating transducers having several grating sections connected electrically in parallel, but acoustically in series. A photograph of a portion of the multi-section grating (or "hybrid") transducer pattern is shown in Figure 26(a). In this instance every fourth electrode is connected to an alternate pad while the three floating fingers between these driven electrodes establish the grating pattern. It should be observed that interconnecting grating transducers in this fashion requires the central driven electrodes to be twice the width of the one-half-acoustic-wave-length-wide floating electrodes. This can be deduced from the delta-function model¹² for the transducer with the requirement that the phase of the excitation delta functions match that of the generated surface wave. The transducer illustrated has a fundamental grating period of 12 μm ,



(a) Three-section four-period grating-transducer pattern.
Middle electrodes are one full period in width.



(b) Four-period interdigital transducer.

SA-1679-31

FIGURE 26 PHOTOGRAPHS OF ALUMINUM-TRANSDUCER PATTERNS ON YZ LiNbO_3
(transducer period = $12 \mu\text{m}$)

which corresponds to a synchronous frequency of 290 MHz on a Y-cut, Z-propagating LiNbO_3 crystal. The interdigital transducer (and bond-wire connection) shown in Figure 26(b) has 3- μm -wide electrodes and gaps and thus should also have a synchronous frequency of 290 MHz.

The possibility of coupling to surface waves through the jump-over field between driven electrodes was discussed above for the example of a single-section grating transducer. For a multi-section array this effect, if present, should be magnified because there would be several periods of jump-over field that could couple to the surface waves. A schematic diagram of the electric-field configuration for two sections of a multi-section grating transducer is shown in Figure 27.

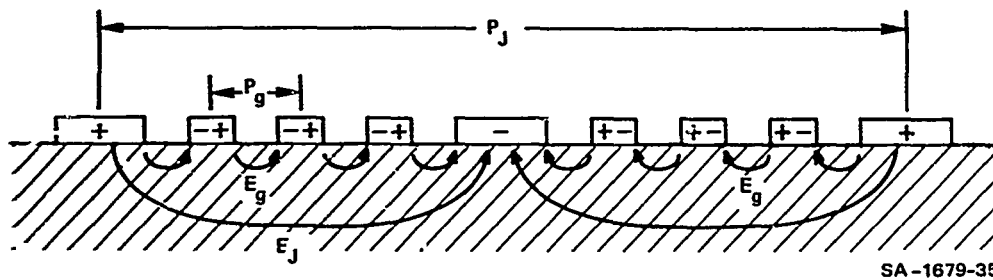


FIGURE 27 SCHEMATIC DIAGRAM OF THE ELECTRIC-FIELD PROFILE IN A MULTI-SECTION GRATING TRANSducer ILLUSTRATING THE GRATING ELECTRIC FIELD E_g AND JUMP-OVER FIELD E_j

The electric field E_g that extends between adjacent electrodes establishes a spatially varying field of periodicity P_g . This field corresponds to the fundamental grating mode of the transducer and should couple most strongly to surface waves when driven at a frequency equal to the surface-wave velocity divided by the periodicity P_g . However, coupling to other field components may occur. If one neglects for the moment the shielding effect of the floating electrodes of the array, it is apparent there will be a component of electric field (labeled E_j) between the driven

plus and minus electrodes. This field may also couple to surface waves and, as seen from the diagram, has a periodicity P_J . Thus both G and J field components may couple to surface waves. The driven electrodes can be thought of as forming an interdigital transducer of period P_J having electrodes whose widths are much smaller than the corresponding gaps. Milson¹⁷ has shown that the narrow-electrode, wide-gap configuration leads to stronger coupling at the harmonics of the fundamental synchronous frequency than for interdigital transducers having equal electrode and gap widths. Thus one would expect to see surface-wave responses that correspond to the jump-over field periodicity P_J , as well as to the grating-electrode periodicity P_G . The four-section grating transducer, shown in Figure 26, has a grating period P_G of 12 μm , corresponding to a center frequency of 290 MHz (on YZ LiNbO_3). The period of the interconnecting electrodes P_J is approximately 102 μm , which indicates that the fundamental and first few odd harmonics would occur at 34 MHz, 102 MHz, 170 MHz, 238 MHz, and 306 MHz on YZ LiNbO_3 . In Figure 28, the untuned insertion loss between two three-section grating transducers is shown. The peaks in the insertion-loss characteristic correlate very closely to the frequencies given above (indicated by arrows). The peaks occurring at 102 MHz, 170 MHz, and 238 MHz correspond to the third, fifth, and seventh harmonics for the driven alternate-phase electrodes. The peak at 260 MHz is attributed to the first sidelobe of the thirteen-period grating transducer. Two facts are evident from the insertion-loss data for the multi-section transducer: (1) It exhibits approximately 10 dB less loss at the grating frequency of 285 to 290 MHz than at other frequencies, indicating relatively strong coupling to the grating mode, and (2) the periodically spaced lower-frequency components clearly match the expected harmonic response due to the jump-over fields. Thus it is evident from this measurement that the grating transducer can couple to both the fields between adjacent electrodes (grating mode) and to the fields that extend between the driven electrodes (jump-over mode).

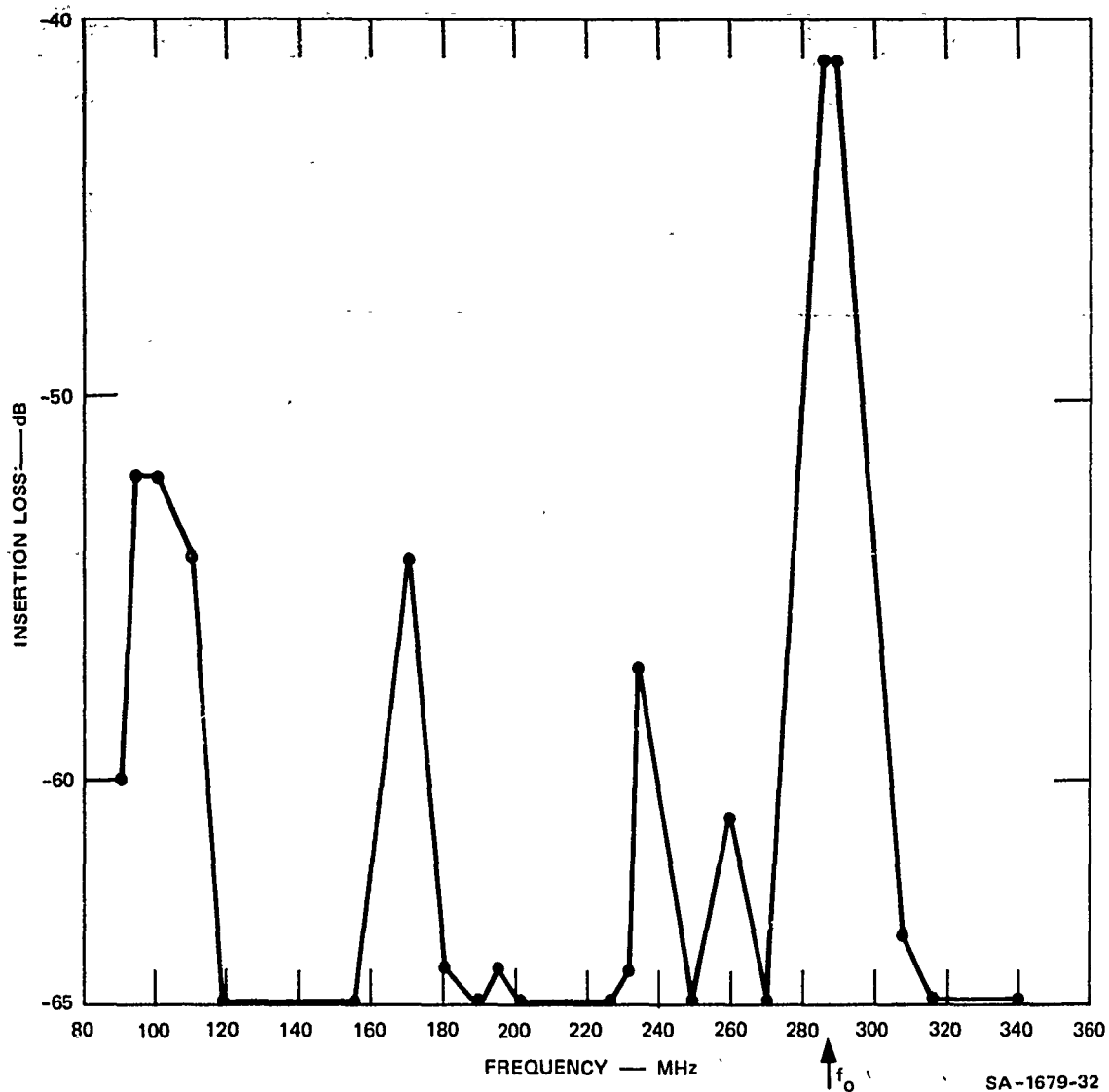
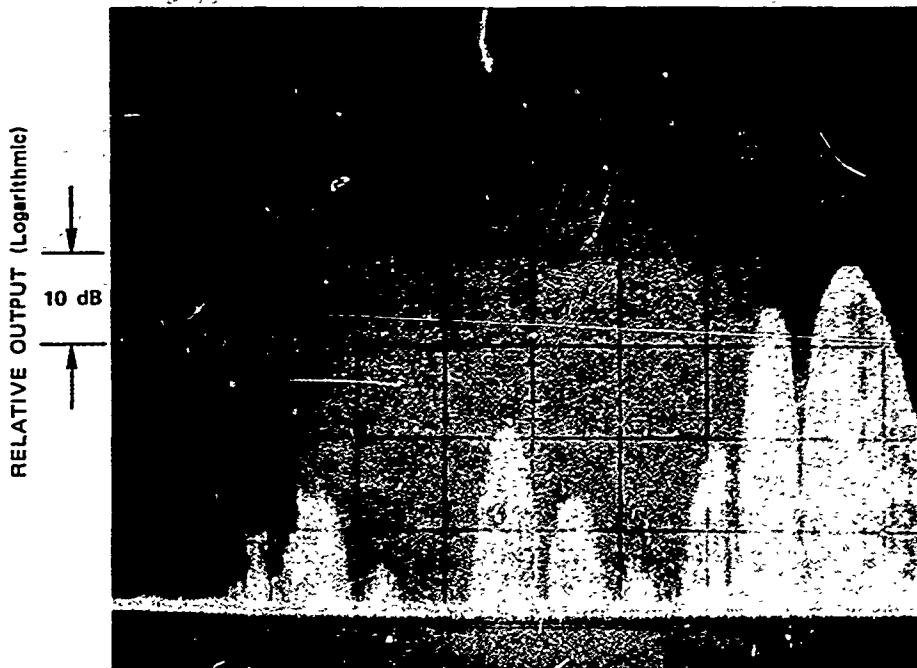
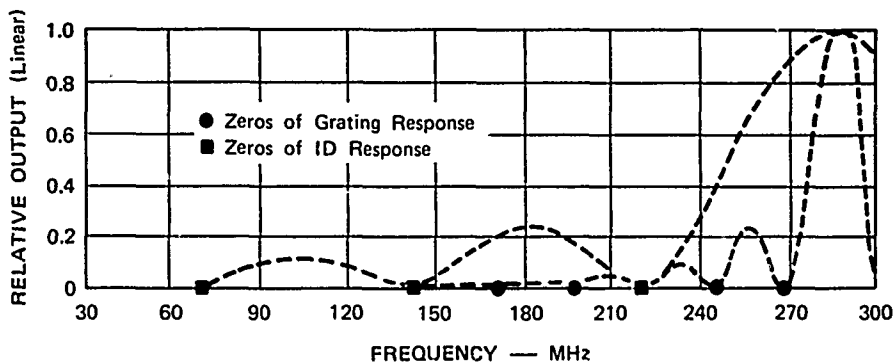


FIGURE 28 UNTUNED INSERTION LOSS FOR SURFACE WAVES GENERATED AND DETECTED BY THREE-SECTION TRANSDUCERS HAVING FOUR PERIODS PER SECTION (i.e., $N = 13$)

The close-in sidelobe structure of the grating transducer has been investigated. The results of insertion-loss measurements made between a thirteen-period grating transducer and a four-period interdigital transducer are shown in Figure 29. The transmission loss measured on a large-dynamic-range spectrum analyzer shows that the minimum loss occurs at the center frequency of the grating and interdigital transducers (285 MHz). The close-in lower-frequency sidelobes have relative maximum responses at 260 and 240 MHz which agree well with the expected behavior of a thirteen-period grating transducer. The theoretical frequency responses of a four-period interdigital and a thirteen-period grating transducer (assuming a $\sin x/x$ type characteristic, where $x = N\pi(\omega - \omega_0/\omega_0)$, N is the number of periods within the transducer structure, and ω_0 is the synchronous radian frequency) are shown in Figure 29(b). The measured bandwidth of the grating transducer is 20 MHz and is quite close to the theoretically predicted value of 22.3 MHz. Above 200 MHz the measured frequency response correlates to a high degree with the expected sidelobe structure of the combined interdigital and grating responses. As seen in Figure 29 the frequency response of the wideband four-period interdigital transducer covers a sufficient range to encompass the first three sidelobes of the grating transducer within its main lobe, and can also detect the surface acoustic waves that are generated by the jump-over field at lower frequencies within its two lower-order sidelobes. In fact, the sidelobe structure of the lower-frequency responses occurring at 160 MHz and 115 MHz (observed in Figure 28) has the same frequency extent $f_0/N = 22$ MHz as the main sidelobes. The high-frequency response roll-off observed in Figure 29 is due to two reasons: (1) The large capacitance to ground of the grating transducer structure (pad area $\sim 0.75 \text{ mm}^2$), and (2) the decreased output power available from the test-oscillator source above 300 MHz. The sidelobe level observed at 260 MHz is substantially larger (~ 12 dB above) than the -16.9 dB level relative to the main lobe that



(a) MEASURED FREQUENCY RESPONSE OF A GRATING TRANSDUCER DRIVING AN INTERDIGITAL TRANSDUCER



(b) THEORETICAL FREQUENCY RESPONSE OF INTERDIGITAL AND GRATING TRANSDUCERS

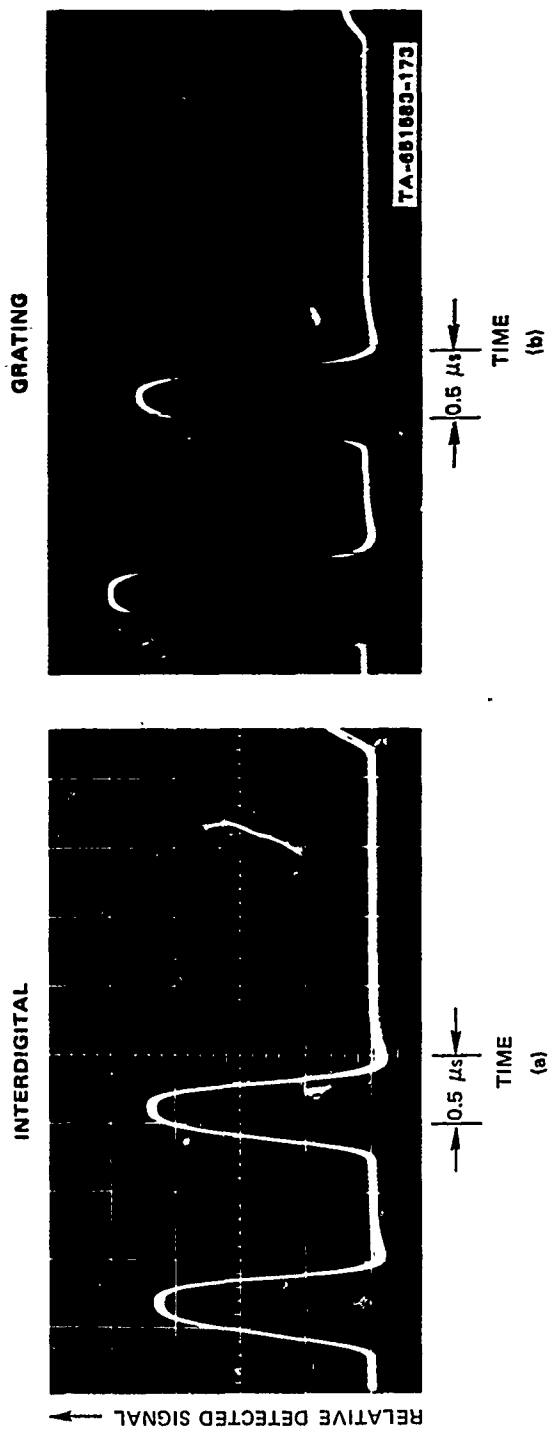
SA-1679-33

FIGURE 29 COMPARISON OF MEASURED AND CALCULATED TRANSDUCER RESPONSE BETWEEN A FOUR-PERIOD INTERDIGITAL TRANSDUCER AND A THIRTEEN-PERIOD GRATING TRANSDUCER

is predicted by theory. This indicates that either extra surface-wave coupling is occurring at this frequency or that the sidelobe level is not following the expected $\sin x/x$ type behavior.

In order to determine how efficiently the grating transducer operates at its center frequency, and relate this to measurements made on interdigital transducers that operate at the same frequency, pulsed transmission-loss data were taken between pairs of thirteen-period grating transducers and between two four-period interdigital transducers, both of which were fabricated on the same piece of YZ LiNbO_3 . The untuned insertion loss between the two grating arrays (spaced 5 mm apart) was 12 dB larger at the synchronous frequency than the insertion loss between the two interdigital arrays having the same separation. Measurements made of the input reflection coefficient of the two types of transducers showed that the 12-dB-higher loss of the grating-transducer pair could be attributed mostly to a difference in mismatch loss for the grating and interdigital transducers owing to the relatively large impedance of the grating transducer at 290 MHz. Figure 30 displays the detected delayed signal obtained when either (1) two interdigital transducers were used or (2) two grating transducers were used. The initial pulse observed is due to direct RF feedthrough of the input signal in both cases.

In order to verify that the conversion efficiency of the two transducer types is indeed comparable, tuned-insertion-loss measurements were carried out for both types. The measurements revealed that the tuned insertion loss between the two grating transducers on the average was within 1 dB of being the same as that measured between the two interdigital transducers at the center frequency. This is believed to be reasonable agreement, considering the slight imperfections observed in the several pairs of transducers tested and the differences in



UNTUNED INSERTION LOSS \approx 12 dB LARGER FOR GRATING TRANSDUCERS
 MEASURED MISMATCH LOSS: INTERDIGITAL = 4.2 dB
 GRATING = 17.4 dB
 DIFFERENCE = 13.2 dB

FIGURE 30 DETECTED SURFACE ACOUSTIC WAVE OUTPUTS BETWEEN (a) TWO INTERDIGITAL TRANSDUCERS AND (b) TWO GRATING TRANSDUCERS (operated at the synchronous frequency (285 MHz) of both transducers)

resistive loss for the different transducers. The photographs of Figure 30 show the delayed pulse for the grating transducers to be essentially identical to that for the interdigital transducers, with the spurious-bulk-wave level more than 25 dB below the direct surface-wave level at the synchronous frequency. The above experimental results give evidence that with suitable matching, the grating transducer is an efficient means for transducing surface acoustic waves (comparable to interdigital transducers).

e. Spurious Signals in Grating Transducers

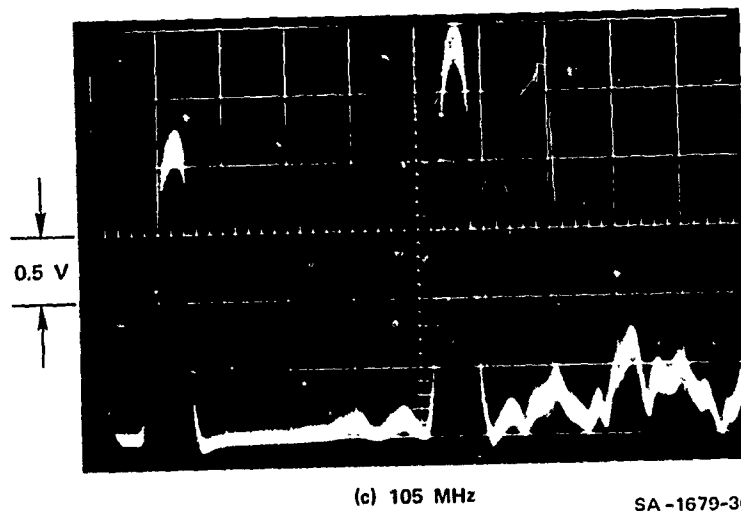
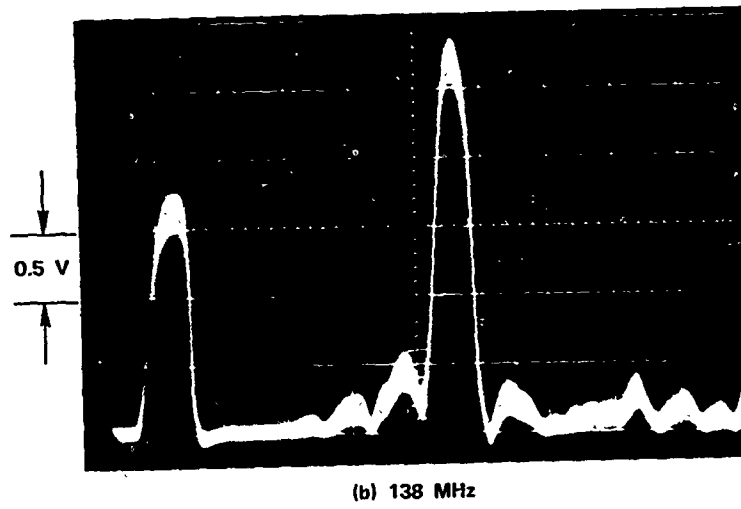
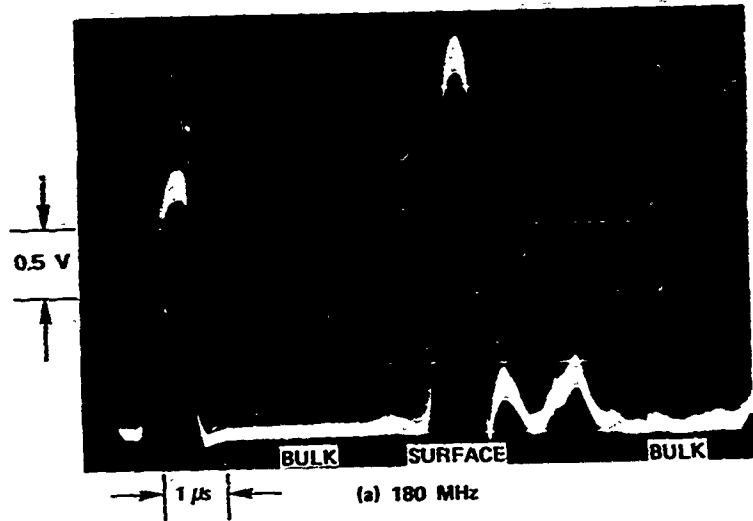
The question of how much bulk-wave generation occurs from any surface-wave-transducer scheme has not as yet been resolved. Recent laser-probe measurements¹⁸ carried out on twenty-period interdigital transducers on Y-cut, Z-propagating lithium niobate indicate that 10 percent of the input electrical power is radiated as shear waves when the transducer is driven at its synchronous frequency. Similar laser-probe measurements on the grating transducer have not been carried out; however, measurement of the input impedance of the grating transducer suggest that bulk-wave radiation may make a contribution to the transducer's radiation resistance both at frequencies near the grating-mode synchronous frequency and at lower frequencies. It is well known¹⁹ that any spatially-periodic-varying electric field, when applied to a piezoelectric material, is capable of exciting bulk waves. When the operation frequency f obeys the formula

$$f \geq \frac{v_{\text{BULK}}}{P}$$

where v_{BULK} is the velocity of the bulk mode of interest and P is the periodicity of the electric excitation field, coherent generation of bulk waves may take place and strong coupling is possible. Thus, interdigital transducers are normally operated at a center frequency $f_0 = v_s/P$

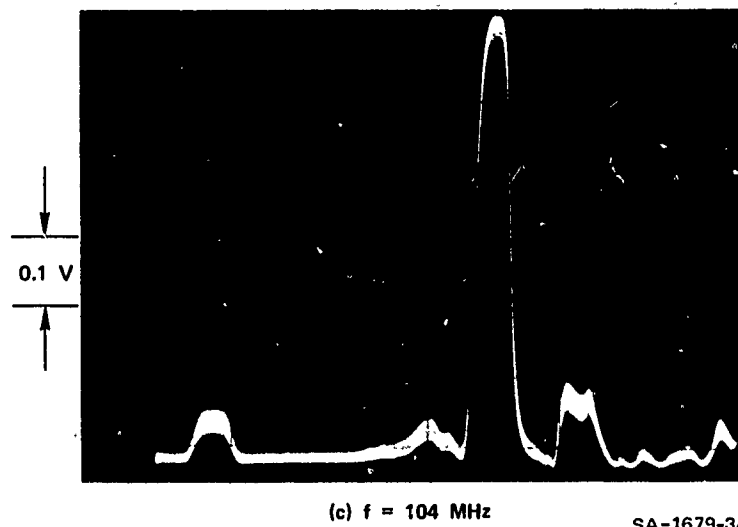
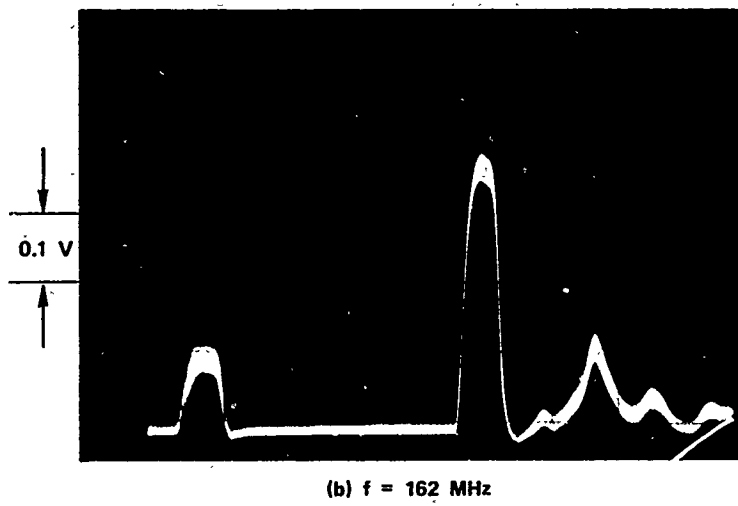
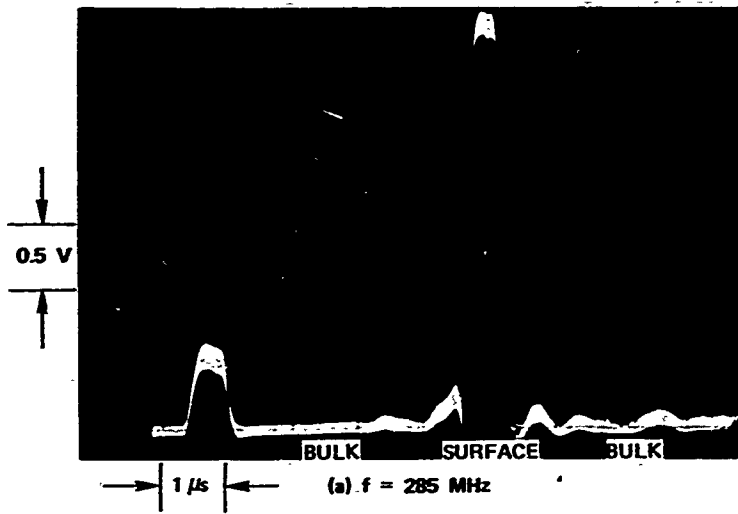
that is below the frequency of maximum bulk-wave response. This is true also for the fundamental mode of the grating transducer. However, the jump-over electric-field component associated with the end electrodes of the grating transducer has a period that is much larger than the fundamental grating period. Thus bulk waves should couple to this field component at frequencies that are below the synchronous frequency for the grating array.

The tendency of grating arrays to generate bulk waves was investigated experimentally over a wide range of frequencies by making pulsed-insertion-loss measurements between pairs of $N = 5$ single-section gratings and $N = 13$ three-section gratings (approximately four periods per section). The observed bulk waves were distinguished from surface waves by time resolution and by selectively attenuating the surface waves. Figures 31 and 32 display the pulse responses between pairs of grating transducers operated at their synchronous frequency and at lower frequencies that correspond to other minima of insertion loss. For the case of the $N = 5$ grating transducers, the bulk modes are more than 14 dB down from the main delayed surface-wave signal at the synchronous frequency. Measurements over a 40-MHz frequency range centered about 180 MHz show the bulk modes to be at least 13 dB below the main delayed signal over this range. Outside this range, rapid fluctuation in bulk-wave level is noted. Measurements on the thirteen-period grating transducer (Figure 32) shows better suppression of bulk waves than for the single-section transducers, with spurious level ≈ 25 dB below the main surface-wave pulse at synchronism and remaining more than 23 dB below the referenced level throughout the frequency range above 135 MHz. It should be noted that no extra precautions were taken to reduce the level of bulk waves transmitted and received (e.g., roughening or tilting the crystal's back surface). Hence, these measurements should be viewed only as indicative of the bulk-mode transduction capabilities of the different grating-



SA-1679-36

FIGURE 31 PULSE RESPONSE OF A FIVE-PERIOD GRATING TRANSDUCER



SA-1679-34

FIGURE 32 PULSE RESPONSE OF A THIRTEEN-PERIOD GRATING TRANSDUCER

transducer structures. It is believed the spurious bulk-wave level could be substantially reduced by either altering the distance between transducers or altering the crystal geometry. However, this would not reduce the coupling (and subsequent energy loss) to bulk waves from a grating transducer. Fortunately the measurements appear to indicate that bulk waves are not strongly coupled at frequencies near the grating mode and that multi-section many-period transducers tend to discriminate against them.

Milsom¹⁷ has observed that surface-wave transducer arrays having a large number of periods discriminate against bulk-wave transduction. He argues that acoustic waves generated by fields having a periodicity equal to the surface-wave wavelength will add coherently from the N transducer periods so that the generated surface-wave power will be proportional to N^2 . The bulk-wave power, on the other hand, adds incoherently and thus is proportional to N . These predictions agree well with the experimental results obtained on interdigital transducers¹⁸ and with measurements carried out on several types of grating arrays. For example, the three-period grating transducer gave the largest bulk-wave response, the five-period grating transducer somewhat less, and the thirteen-period multi-section grating transducer produced very little. Further indication of this effect is obtained from the measurements of tuned insertion loss discussed previously that reveal nearly comparable efficiencies (within 0.5 dB per transducer) for interdigital and grating transducers tested at synchronism. Thus the amount of energy lost by the $N = 3$ grating to bulk modes must not be more than 10 percent greater than that lost by the $N = 4$ interdigital array.

In general, the amount of energy lost to bulk waves from any surface-wave transducer cannot be estimated without resorting to a detailed analysis that takes into account the piezoelectric coupling strength, crystal orientation, electric-field configuration, and

transducer size. An analysis of this problem for the grating has not yet been attempted.

Initial tests have been carried out to investigate the triple-transit signal level for the surface waves reflected between grating transducers. The triple-transit signal was more than 24 dB below the direct-surface-wave signal for the $N = 5$ transducer and 22 dB below the direct signal for the $N = 13$ transducer. In both of these cases the transducers were effectively terminated in 50 ohms.

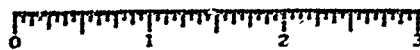
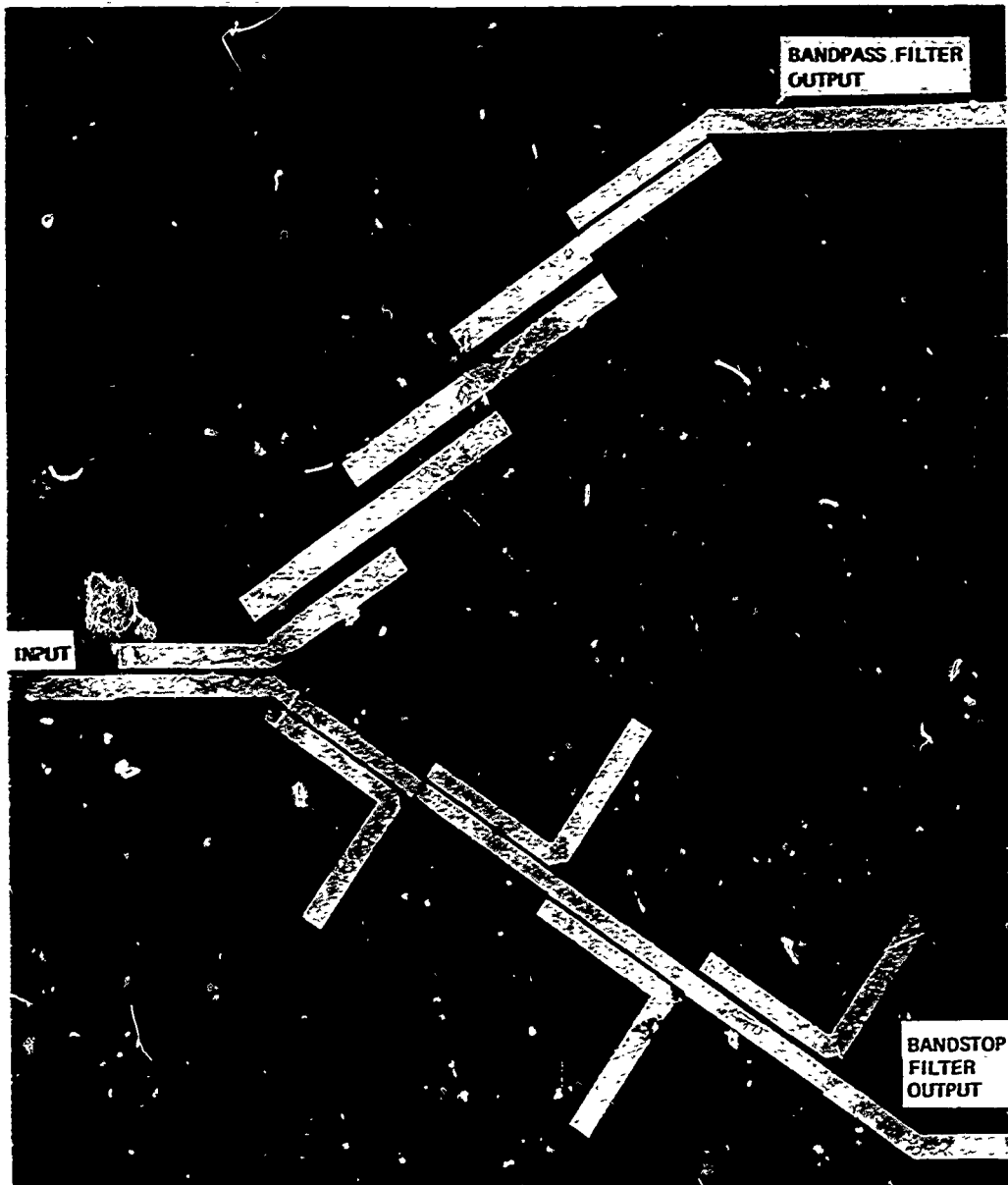
III MULTIPLEXERS

A. General

Multiplexers are utilized to separate frequencies in certain ranges from a spectrum of signals covering a larger range of frequencies, or to combine a number of frequency bands into a single spectrum. This can be accomplished using hybrids, circulators, and/or filters. A common technique is to cascade channel-dropping filters, each of which separates or combines a particular band of frequencies. Each channel-dropping filter consists of a bandpass and bandstop filter suitably designed and interconnected to produce a constant-resistance input impedance.

The theory for constant-resistance channel-dropping filters has been described by several authors, and no new theory is presented in this report.^{20,21} What we are concerned with here is the feasibility of a new channel-dropping-filter geometry that is particularly compact and that utilizes the stripline or MIC surface area in a highly efficient manner. In the past, channel-dropping filters have often consisted of interdigital, combline, or halfwave-parallel-coupled-line bandpass filters combined with bandstop filters consisting of quarter-wavelength stubs separated by quarter-wavelength lines--i.e., unit elements, hereafter abbreviated UE. In stripline a channel-dropping filter consisting of a halfwave parallel-coupled-line bandpass filter and quarter-wavelength-line bandstop filter might take the form shown in Figure 33. Note the inefficient utilization of substrate surface area revealed in this photograph.

The channel-dropping-filter geometry investigated in this report utilizes hairpin bandpass filters and folded-line bandstop filters. Both



7A-6884-87

FIGURE 33 STRIP-LINE CHANNEL-DROPPING FILTER UTILIZING HALF-WAVE PARALLEL-COUPLED-LINE BANDPASS FILTER AND QUARTER-WAVELENGTH-LINE BANDSTOP FILTER

filters are considerably more compact than their linear counterparts, and thus utilize the surface area of the substrate very effectively. A channel-dropping-filter configuration analogous to that shown in Figure 33, but utilizing the latter filters, is shown in Figure 34.

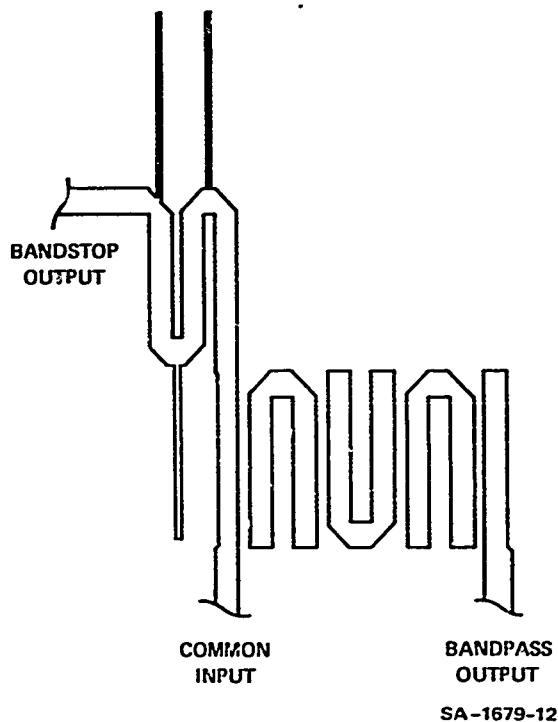
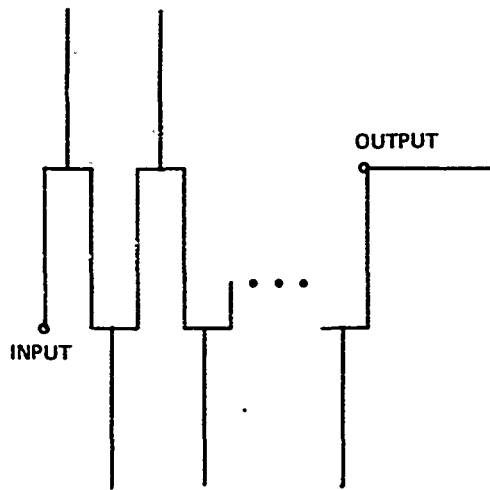


FIGURE 34 COMPACT STRIP-LINE CHANNEL-DROPPING FILTER UTILIZING HAIRPIN BANDPASS FILTER AND FOLDED-LINE BANDSTOP FILTER

In earlier reports on this contract the hairpin filter and meander-line transformer were developed.^{22,23,24} The meander-line transformer can be converted into a bandstop filter by adding open-circuited stubs at meander-line turns, as shown in Figure 35. This yields a compact bandstop filter suited for stripline or MIC media.

B. Folded-Line Bandstop-Filter Design

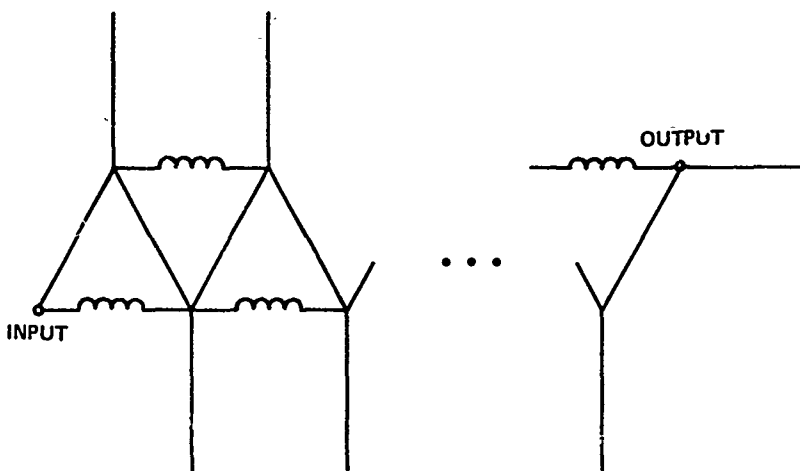
One theory for the design of channel-dropping filters calls for designing the filters from singly-terminated prototypes using approximate



SA-1679-13

FIGURE 35 FOLDED-LINE BANDSTOP FILTER

methods, or from transfer functions for singly-terminated filters using exact methods. Here, however, because of the circuit complexity of the folded-line bandstop filter, a numerical optimization method has been used rather than conventional exact or approximate methods. A numerical optimization method has additional advantages over conventional synthesis in that the coupling between folded lines, as well as stub impedances, can be restricted to reasonable values prior to the start of the filter design. Consequently, physical realizability is guaranteed from the outset. Sato has given an equivalent circuit for meander lines that requires only a slight modification in order to transform it into the equivalent circuit for a folded-line bandstop filter.²⁵ This is shown in Figure 36. Coupling between folded lines is accounted for solely by "S-plane inductors" connecting unit elements.²⁶ Unit elements are depicted as straight lines, and short-circuited stubs as inductors in Figure 26. An "unfolded" conventional bandstop filter is obtained by setting all inductive admittance values to zero. A hybrid geometry is obtained by setting some but not all inductive admittance values to zero. Using the equivalent circuit of Figure 36 the network response of the



SA-1679-14

FIGURE 36 FOLDED-LINE-BANDSTOP-FILTER EQUIVALENT CIRCUIT

folded-line bandstop filter can be calculated for use in various numerical optimization programs.

Bandler and Charalambous²⁷ have reported on a method of specifying an objective function that leads to mini-max solutions for certain classes of circuit problems. The technique uses least p^{th} minimization and allows the use of very large values of p , which can be shown to approach the mini-max solution as p approaches ∞ . The mini-max solution, itself, may be equi-ripple but does not have to be. The objective function of Bandler and Charalambous, however, is not directly applicable to the bandstop-filter problem here, since it does not maximize the selectivity.

An objective function similar to that of Bandler-Charalambous but more suitable for the bandstop-filter problem is to assign a finite penalty to the objective function when the filter specifications are exceeded, but no penalty when the filter specifications are met. For the singly-terminated bandstop-filter design, the optimization problem then reduces to minimizing the area under the conductance curve in the stopband, subject to the conditions that the ripple does not exceed

specified values in the passband. While it has not been proved that this leads to the maximum selectivity, a consideration of the problem and the locations of the transmission zeros of the bandstop filter leads one to conclude that any differences from optimum should be relatively small.

In order to check this out, a trial singly-terminated bandstop filter consisting of three stubs and three unfolded unit elements was designed for an equi-ripple bandwidth of 30 percent and 1-dB ripple.* The normalized input conductance of the resulting network and the theoretical optimum response are shown in Figure 37. The numerically determined design is seen to have the correct number of ripples and meets the bandwidth specification exactly. Its selectivity is slightly less than theoretical, which is to be expected since the response is not quite equi-ripple. The deviation of the conductance of the numerical design from theoretical can be explained in two ways: (1) The numerical optimization program has reached a local rather than global minimum, or (2) the objective function is not maximizing selectivity directly but rather minimizing the area under the curve, and thus cannot provide the exact theoretical result. (We will be investigating this problem in future work.) Although the numerically determined design is not optimum, it does meet the passband specifications and would be quite acceptable in most any practical application. Consequently, the above described objective function appears suitable for designing folded-line bandstop filters.

Next, it was decided to design a folded-line bandstop filter of the following specifications for construction and testing in a trial channel-dropping filter:

- Equi-ripple bandwidth = 0.10
- Ripple = 1.0 dB

* 1 dB ripple corresponds to $G_{in} / G_{LOAD} = 1.259$ maximum.

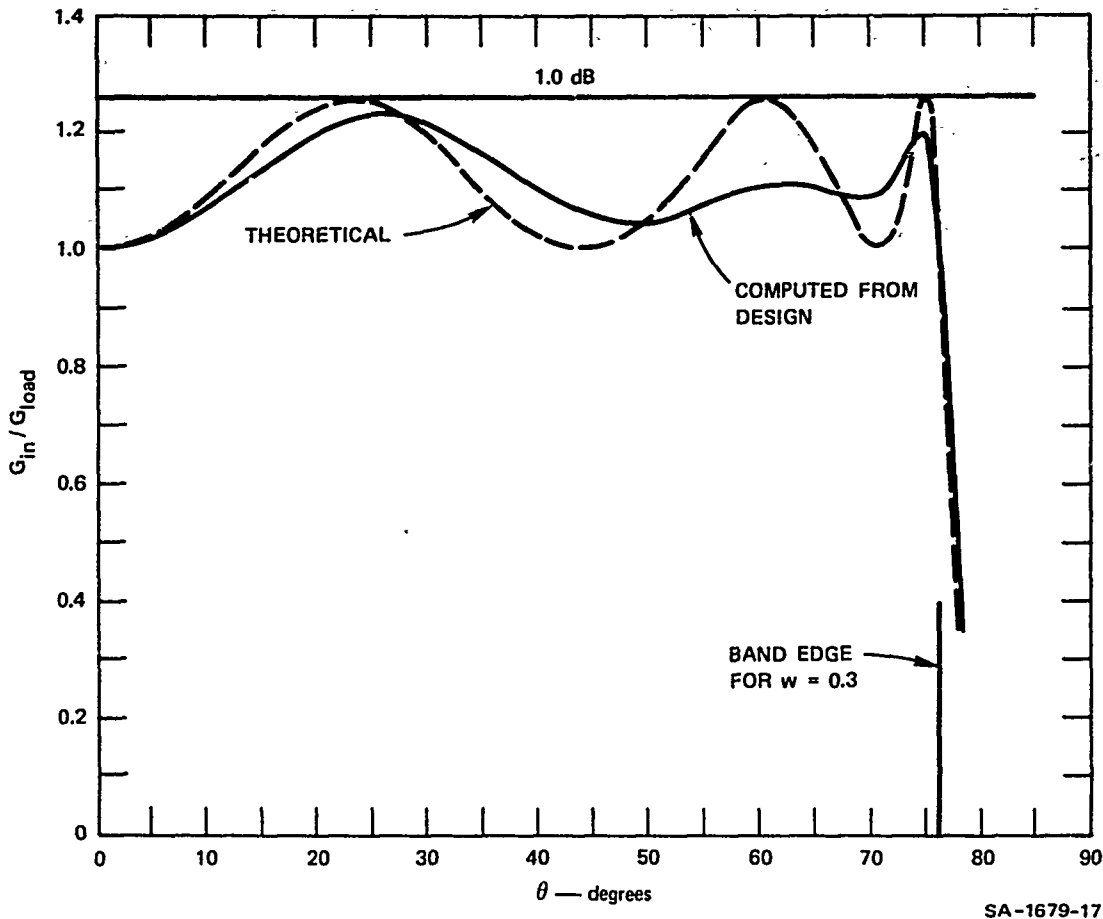


FIGURE 37 COMPUTED AND THEORETICAL INPUT CONDUCTANCE FOR TRIAL BANDSTOP FILTER

- Coupling between unit elements = 16 to 20 dB
- Center frequency = 1.5 GHz
- Three unit elements
- Three stubs.

The bandstop-filter computer program obtained a design that was not optimum but was judged sufficiently good to test the feasibility of channel-dropping filter design. A singly-terminated hairpin filter was also designed with a slightly smaller equi-ripple bandwidth in order to obtain crossovers of the conductance curve at 0.5 normalized values. The filters were constructed in stripline in Rexolite 1422 ($\epsilon_r = 2.54$) with

ground planes having 0.250-inch spacing. The design specifications for the two filters are given in Table 1. Definitions for parameters used in the table are defined in Section C.

Table 1

INITIAL PARAMETER VALUES FOR TRIAL CHANNEL-DROPPING FILTER

Hairpin Filter						
i	C_g / ϵ_g	C_m / ϵ_m^*	W/H^\dagger	S/H^\dagger	W (inch)	S (inch)
1	3.6280	1.6054	0.6474	0.0625	0.1619	0.0156
2	3.3569	0.1293	0.6111	0.7401	0.1528	0.1850
3	4.0196	0.5020	0.6823	0.3246	0.1706	0.0811
4	4.2664	0.1249	0.7427	0.7511	0.1857	0.1878
5	4.1919	0.6015	0.7385	0.2740	0.1846	0.0685
6	3.8289	0.1334	0.6502	0.7303	0.1625	0.1826
7	3.0802	2.0121	0.5557	0.0357	0.1389	0.0089
8	3.4899		0.6255		0.1564	
Folded-Line Bandstop Filter						
i	C_g / ϵ_g	C_m / ϵ_m	W/H	S/H	W (inch)	S (inch)
1	4.2975	0.5852	0.7324	0.2815	0.1831	0.0704
2	3.5482	0.5748	0.6582	0.2865	0.1645	0.0716
3	4.1514		0.6946		0.1737	
Bandstop-Filter Normalized Stub Admittance						
i				Y_s / Y_0^\ddagger		
1				0.08229		
2				0.08010		
3				0.05626		

$$* C_m \equiv C_{i,i+1}$$

$^\dagger H$ = Ground-plane spacing

$^\ddagger Y_0$ = Generator admittance; Y_s = Stub admittance

C. Definition of Parameters Used in Design Tables

Figure 38 depicts a cross-sectional representation of an arbitrary coupled transmission-line network in any TEM or quasi-TEM medium and depicts the unnormalized distributed capacitance parameters C_{g_i} and $C_{i,i+1}$. These are defined as follows:

C_{g_i} = Capacitance to ground per unit length for the i^{th} conductor

(17)

$C_{i,i+1}$ = Mutual capacitance per unit length between the i^{th} and $i^{\text{th}} + 1$ conductors.

Coupling between non-adjacent lines is assumed negligible.

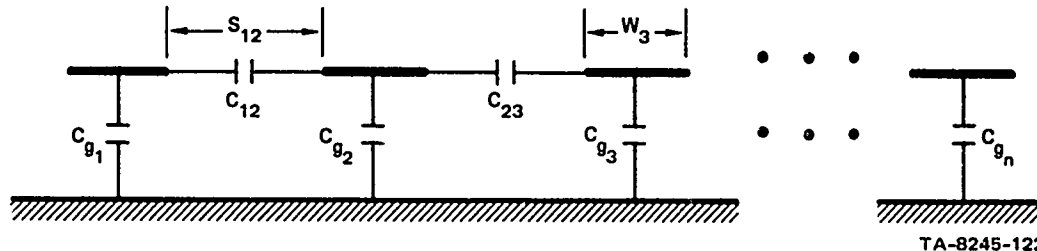


FIGURE 38 SCHEMATIC CROSS-SECTIONAL REPRESENTATION FOR COUPLED TRANSMISSION LINES

The dimensionless, distributed-capacitance parameters that are needed for use with Getsinger's data²⁸ in order to obtain dimensional parameters from electrical parameters are as follows:

$$c_{g_i} = C_{g_i} / \epsilon$$

$$c_{i,i+1} = C_{i,i+1} / \epsilon$$

$$\epsilon = \epsilon_r \epsilon_0$$

(18)

ϵ_r = Relative dielectric constant of the medium

ϵ_0 = Permittivity of free space in the units of
 C_{g_i} and $C_{i,i+1}$.

The impedances of the stubs of the bandstop filter were too large to realize directly with transmission lines. Consequently, capacitive-coupled "half-wave" open-circuited stubs were used. The impedance of the half-wave lines was set at 100 ohms, and the coupling capacitors and line lengths were adjusted to give the correct resonance and slope parameter. American Technical Ceramics capacitive chips were used as coupling capacitors. A photograph of the channel-dropping filter is shown in Figure 39.

D. Experimental Results

In order to experimentally verify the bandstop-filter design, a separate bandstop filter was constructed and tested. Its normalized input conductance was measured and graphed using a Hewlett-Packard automatic network analyzer. The data are given in Figure 40 along with the theoretical computed result. The center frequency for the theoretical result was assumed to be 1.550 GHz. It is seen that the bandwidth of the trial filter is a little greater than theoretical, but that generally there is quite good agreement between the two curves. Better agreement

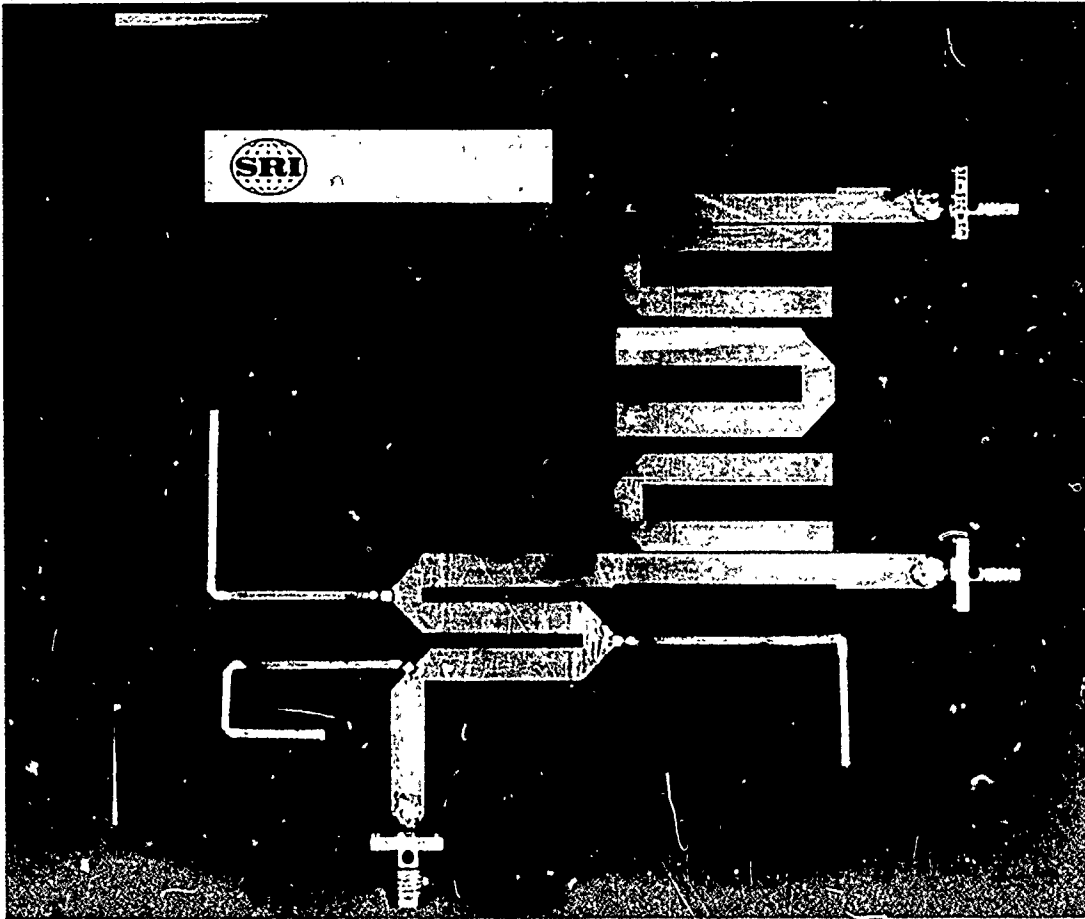


FIGURE 39 PHOTOGRAPH OF TRIAL CHANNEL-DROPPING FILTER

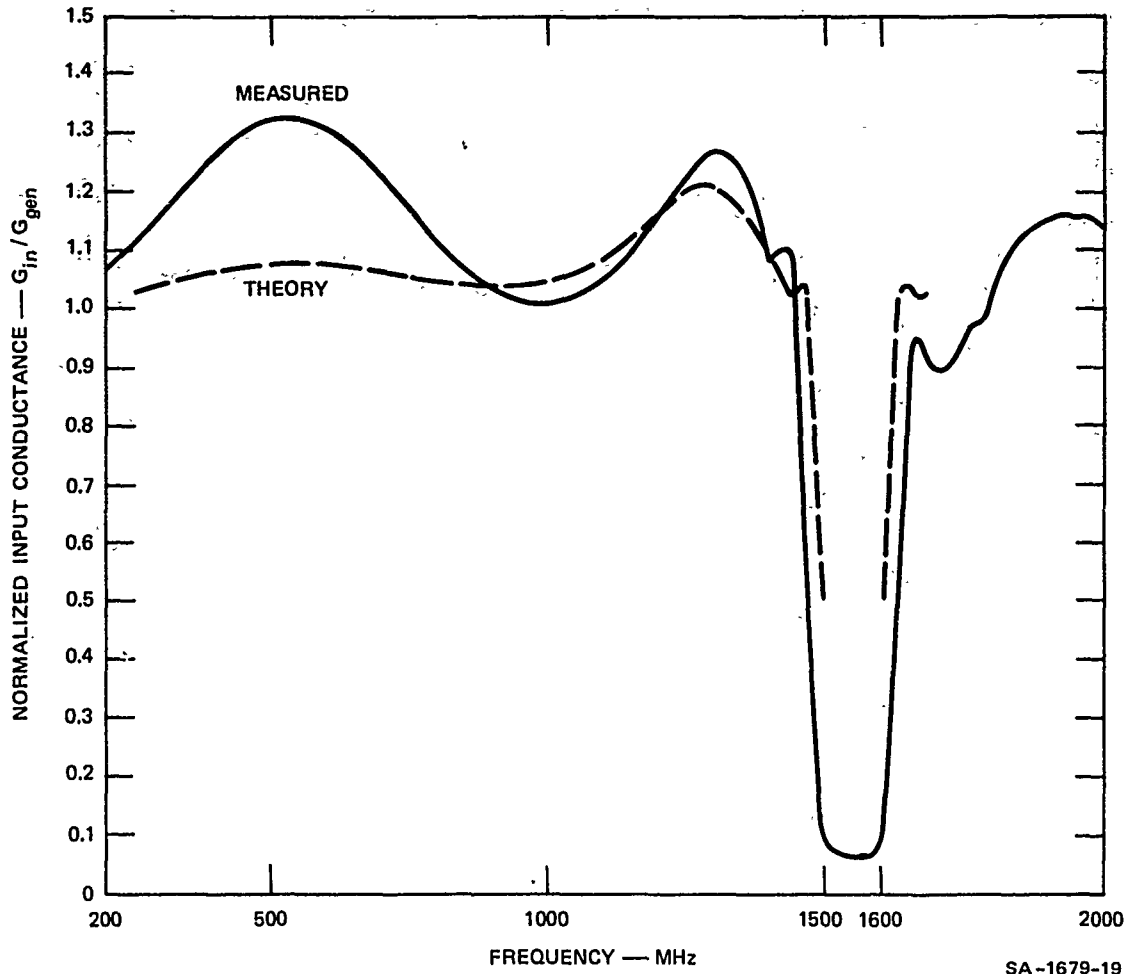


FIGURE 40 THEORETICAL AND EXPERIMENTAL NORMALIZED INPUT CONDUCTANCE OF TRIAL FOLDED-LINE BANDSTOP FILTER

could probably be achieved by refining the compensations of interconnections between folded lines. The bandwidth expansion of the trial filter is most likely due to too small a slope parameter for the shunt stubs and could be adjusted by reducing the capacitive coupling of the "half-wave" resonators. The hairpin filter was also measured by itself and was found to have the proper admittance characteristic, although the bandwidth was slightly narrow relative to the bandwidth of the bandstop filter. However, it was decided to make corrective adjustments after the filters were connected.

Next, the bandpass and bandstop filters were connected and tuned. Initial measurements of return loss and attenuation of the bandpass and bandstop channels are given in Figure 41. The responses clearly verified that the bandpass-filter bandwidth was too small. This was corrected by decreasing the spacing between the second and third resonators, which in turn required an increase in coupling from the input line to the bandpass filter. The final responses after tuning are given in Figure 42. The return loss was quite good below and throughout the passband, but deteriorated to around 13 dB from 1.8 to 2.0 GHz. Above 2 GHz the return loss continued to deteriorate and was only 10 dB at 2.3 GHz. There were several factors contributing to this: (1) The relatively large ripple of the prototype (1.0 dB), (2) incomplete compensation of the interconnections of the hairpin resonators and folded lines, and (3) the use of capacitive-coupled half-wave resonators in the bandstop filter. In the case of the present trial channel-dropping filter the latter cause was the most dominant.

The 3-dB-down bandwidth for the bandpass filter measured 10.2 percent. The midband loss was 1.5 dB and the crossovers occurred at 4.5 and 5.5 dB down from the band-center attenuation.

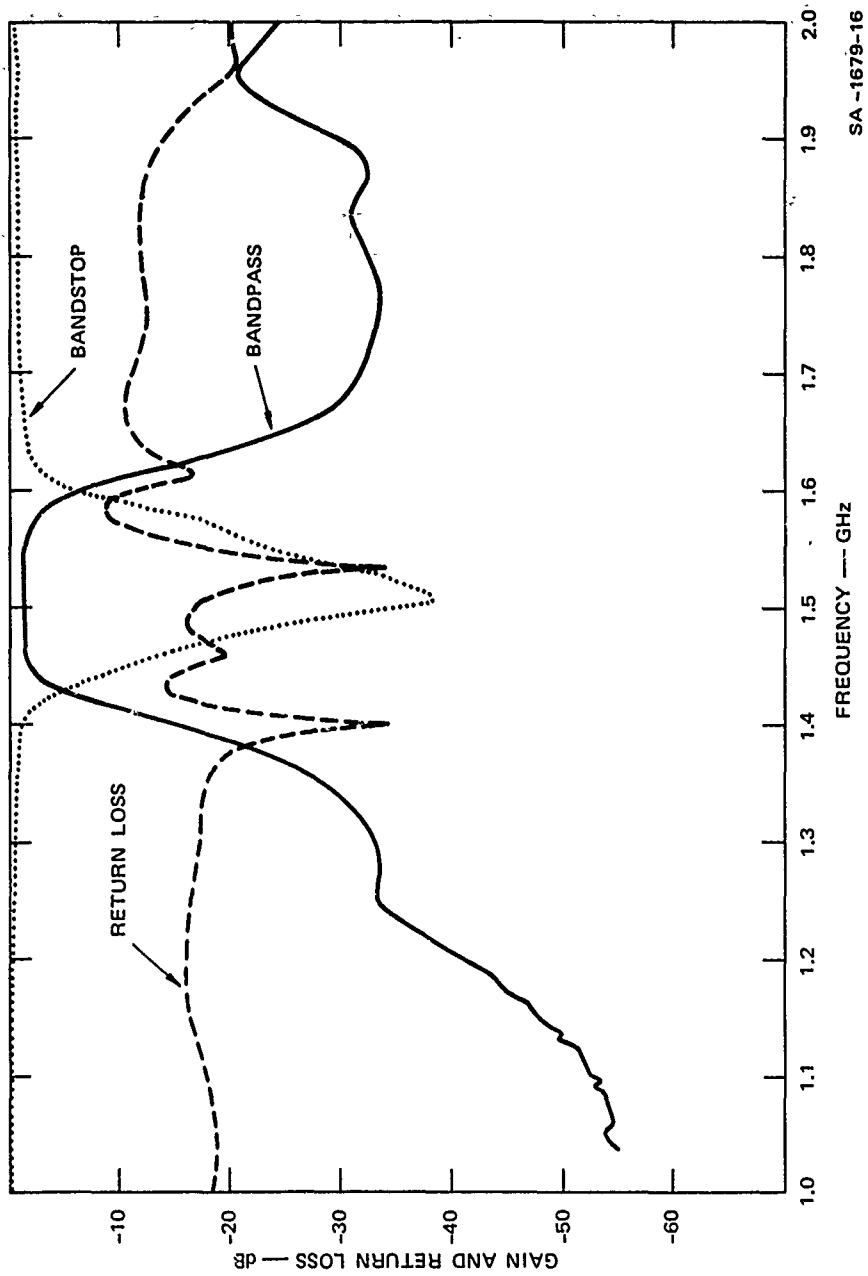


FIGURE 41 RETURN LOSS AND GAIN OF INITIAL CHANNEL-DROPPING FILTER

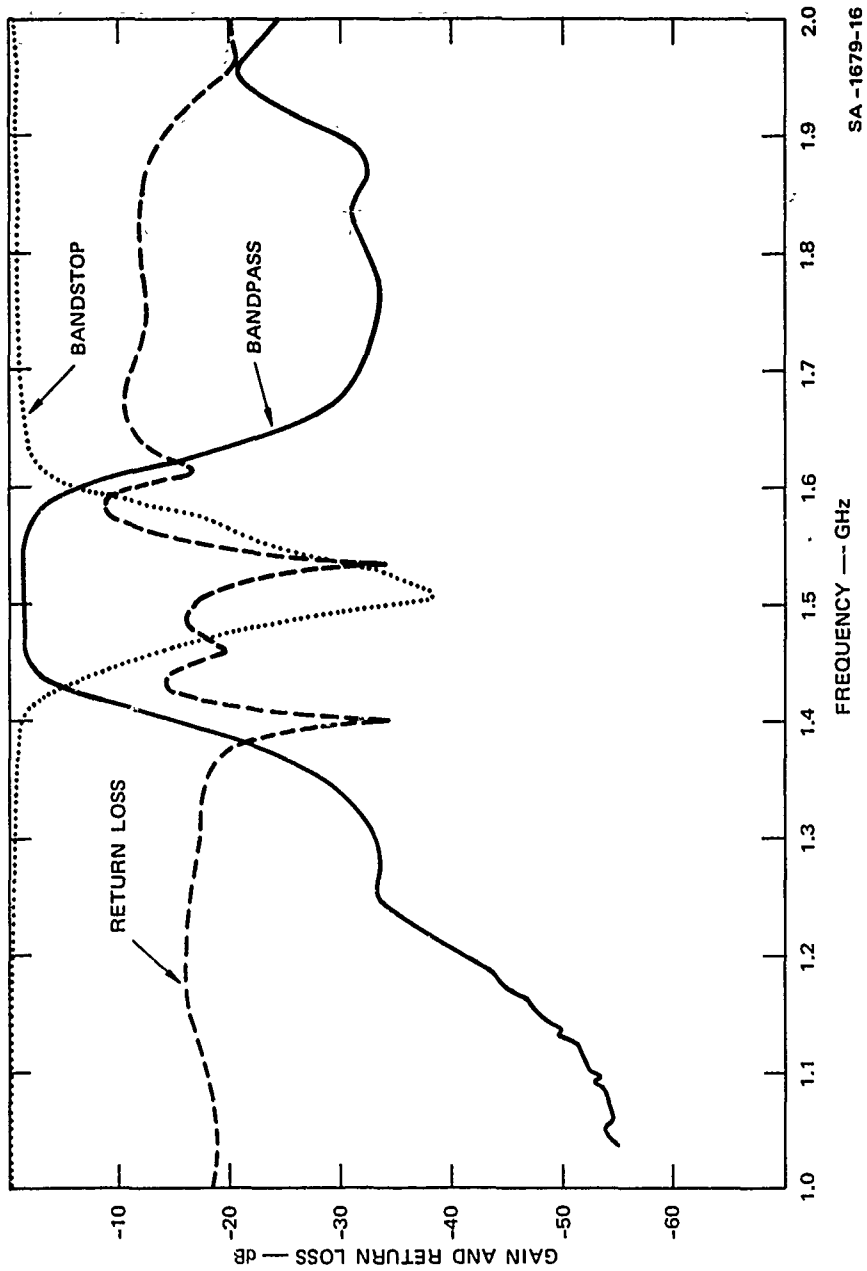


FIGURE 41 RETURN LOSS AND GAIN OF INITIAL CHANNEL-DROPPING FILTER

IV CONCLUSIONS

A. Grating Transducers

A detailed theoretical analysis has been carried out to model the new grating surface-wave transducer. Computer calculations made using this equivalent-circuit model predict that the grating transducer will behave much like an interdigital transducer except that the grating transducer will have a substantially higher input impedance. However, the inclusion of parasitic effects in the model has shown that the overall grating-transducer characteristics are affected much more strongly by stray capacitance to ground at the input than is an interdigital transducer having the same number of periods. The net effect of the stray capacitance is to decrease the input impedance of the grating transducer and to increase its electrical Q .

An experimental investigation of the grating transducer was carried out on several different transducer structures. Both simple one-section and multi-section grating transducers were tested and compared to interdigital transducers fabricated on the same piezoelectric substrate. The measurements of surface-wave-transducer input impedance and insertion loss lead to several conclusions: (1) The grating transducer couples strongly to surface waves at the frequency whose corresponding wavelength coincides with the center-to-center spacing of adjacent electrodes; (2) the conversion efficiency of a tuned grating transducer is comparable to that of a tuned interdigital transducer; (3) the grating transducer has an electric-field component that "jumps over" the electrically floating electrodes of the array and this field couples to both surface and bulk waves (the relatively large period of the jump-over field causes

the surface and bulk waves thus generated to occur predominantly at frequencies well below the grating-mode frequency); and finally, (4) by combining multiple sections of simple grating transducers electrically in parallel, the transducer capacitance can be increased (thereby decreasing the high input reactance) and thus making electrical matching easier. Increasing the transducer capacitance also tends to decrease the effect of the parasitic capacitance to ground. The multi-section grating transducer was also found to generate fewer bulk waves than the simple grating array.

Although the level of understanding of the grating transducer has been increased considerably by the work that has been carried out so far, one or two questions remain that should be examined. One of these is the question of the partial capacitances in a grating structure. A theory should be developed that will be adequate to cover most practical transducer situations. Another question is, how to include the jump-over fields properly in an equivalent-circuit model and how to compute the coupling factors associated with these fields.

Based on the results of this report, it appears that a multi-section version of the grating transducer should perform better than a simple grating structure in several respects. Therefore it is planned to fabricate and test a multi-section or "hybrid" transducer structure that is composed of grating transducers having only one floating finger between each connected pair of end electrodes. This transducer would still operate at a higher frequency than an interdigital transducer for a given finger width because, in the hybrid transducer, interdigital fingers would be one wavelength wide and floating fingers and gaps would be one-half wavelength wide. This type of transducer will be compared experimentally with an interdigital transducer that has one-wavelength-wide fingers and one-half-wavelength-wide gaps, and it will also be compared with a

"double-electrode" interdigital transducer having one-eighth-wavelength-wide fingers and gaps that is operated at its third harmonic.

B. Multiplexers

The measured input conductance of the trial bandstop filter compared favorably with the theoretically computed curve. Discrepancies were attributed to inadequate compensation of the interconnections between folded lines and the effect of the substitutions of capacitive-coupled halfwave resonators for the high-impedance quarter-wavelength stubs. The trial channel-dropping filter was judged to verify the design procedure and the feasibility of the new geometry for stripline and MIC. However, use of half-wave-coupled resonator stubs caused degradation of return loss above the passband. Means are to be considered for overcoming this problem.

Appendix

RAPID-DESIGN CHARTS FOR COUPLED MICROSTRIP LINES

Preceding page blank

Appendix

RAPID-DESIGN CHARTS FOR COUPLED MICROSTRIP LINES *

Various arrangements of coupled transmission lines are basic building blocks in modern microwave circuits. Power combiners and dividers, hybrids, phase-shift networks, mixers, etc. utilize couplers or coupled transmission lines in various forms. In the design of microwave systems, it is a significant advantage to have a rapid and efficient method for determining the physical dimensions of coupled lines from the desired electrical performance.

The data of Bryant and Weiss¹ are the most universally accepted for determining the relationship between electrical performance and mechanical dimensions for microstrip constructions of coupled lines. However, published data are presented in a tabular form generally inconvenient for design work. Figures A-1 and A-2 show a graphical presentation of the Bryant and Weiss data that allows rapid design of microstrip couplers as well as quick assessment of the effects of manufacturing tolerances both on coupler dimensions and substrate dielectric constant.

A simple example will illustrate the procedure for using the charts. Suppose a coupler is desired to operate in a 50-ohm system with -10 dB coupling or a coupling factor, $c = 0.316$. Using the TEM-mode design

* These results are included in this report as a means of rapidly disseminating a widely useful design tool for microstrip coupled lines although not a direct result of the present ECOM support. The techniques outlined were partially developed in conjunction with a program supported by NRL and partially through the personal efforts of the personnel of the Microwave Techniques Program at SRI.

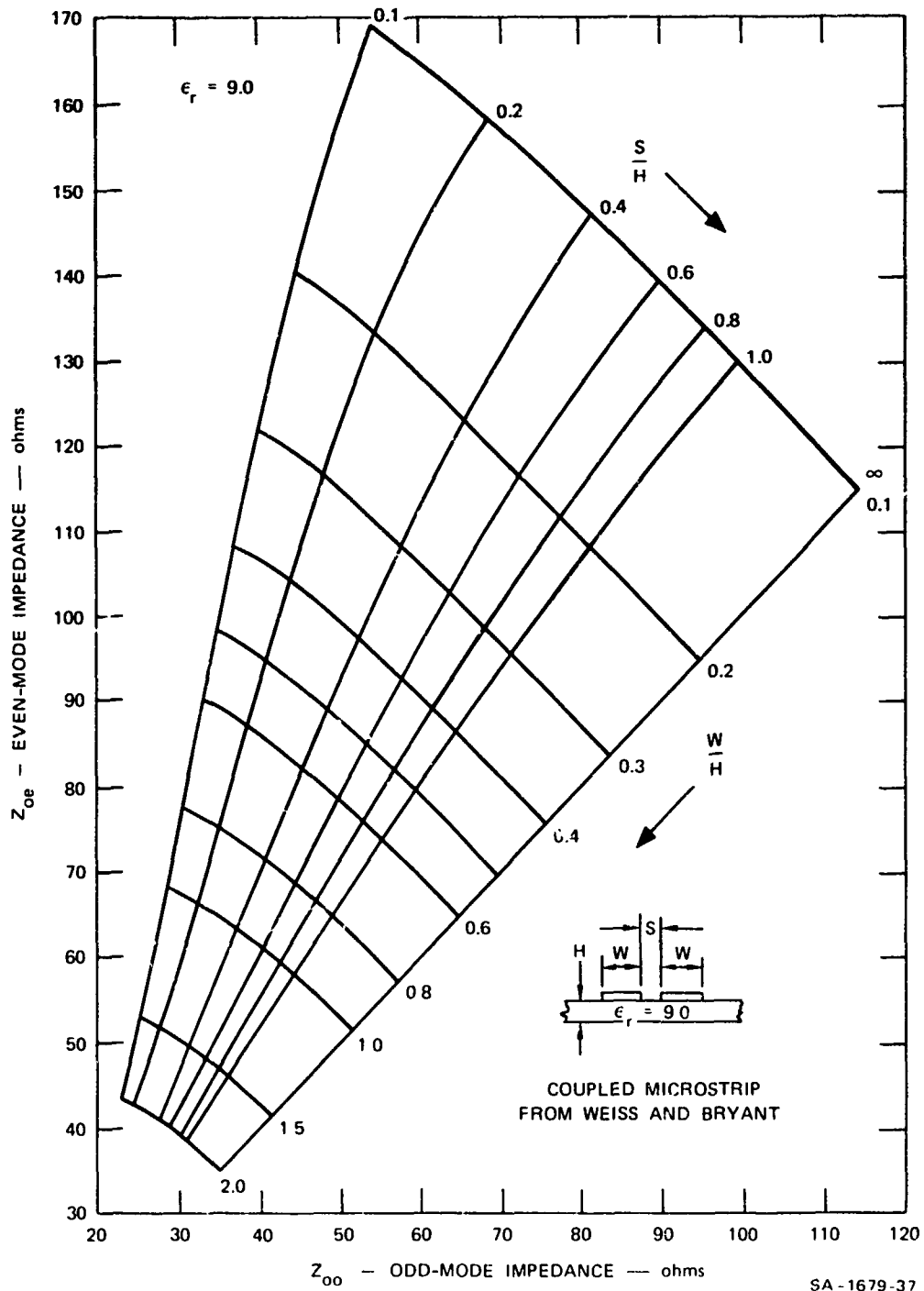


FIGURE A-1 COUPLED-LINE DESIGN CURVES

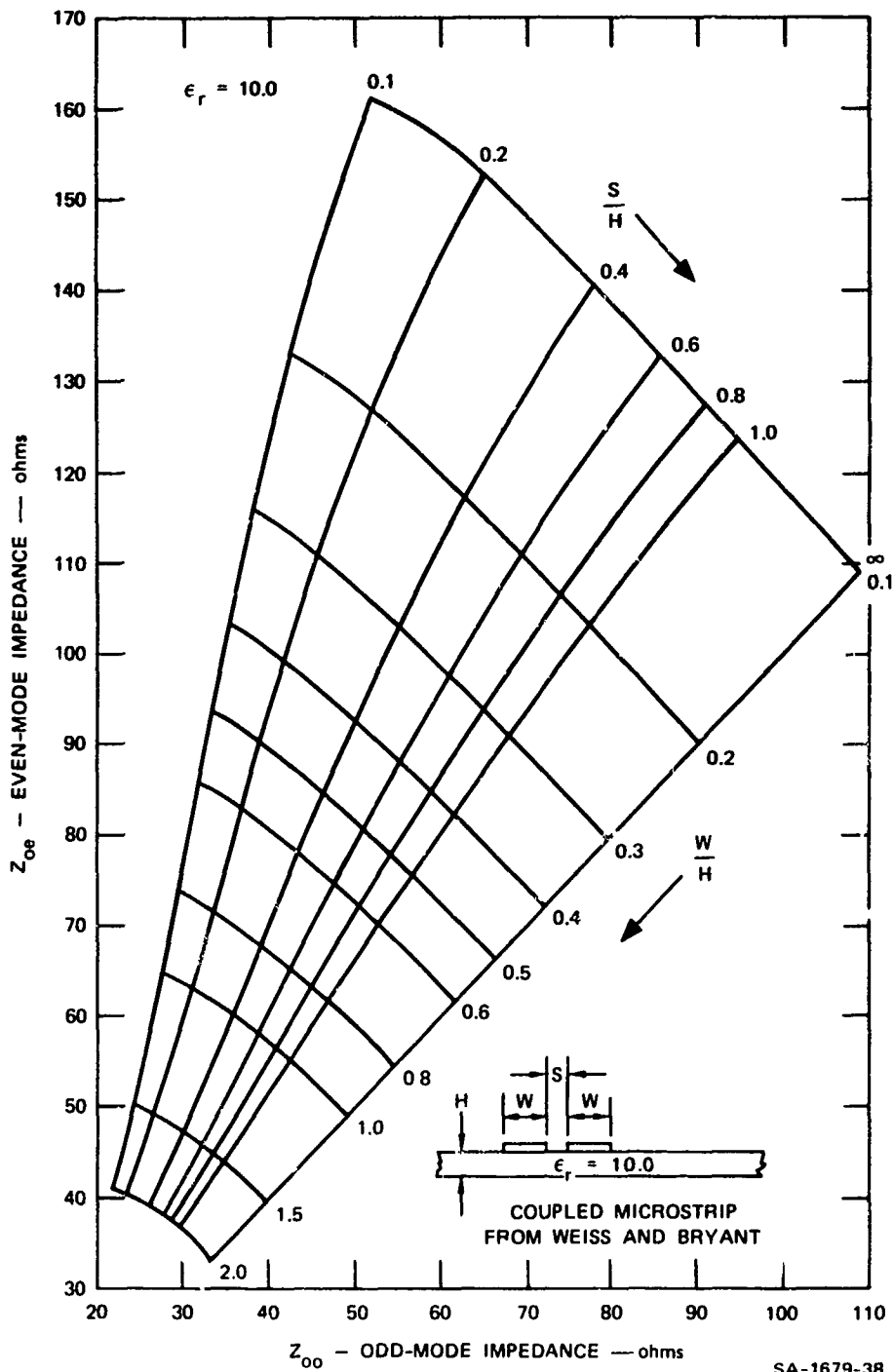


FIGURE A-2 COUPLED-LINE DESIGN CURVES

relations, the odd- and even-mode impedances can be calculated from

$$Z_{oo} = Z_0 \sqrt{\frac{1-c}{1+c}} = 36.0 \Omega$$

$$Z_{oe} = Z_0 \sqrt{\frac{1+c}{1-c}} = 69.4 \Omega \quad .$$

For a substrate material with a relative dielectric constant $\epsilon_r = 10$, enter Figure A-2 at the point where a horizontal line at $Z_{oe} = 69.4$ ohms intersects a vertical line at $Z_{oo} = 36.0$ ohms and read the ratios

$$S/H = 0.28$$

$$W/H = 0.90$$

which completes the design.

In addition to the look-up design feature of the charts, the particular method chosen to present the data accentuates certain aspects of microstrip edge-coupled-line design and the effects of tolerances on expected performance. The curve labeled $S/H = \infty$ is for the condition $Z_{oo} = Z_{oe} = Z_0$ and describes the W/H required for a single microstrip line of characteristic impedance Z_0 . Lines of constant S/H are nearly parallel to lines of constant Z_{oe}/Z_{oo} , which implies that for a given coupling the ratio S/H will be nearly the same for couplers of all impedance levels. (For a given coupling factor, the required ratio Z_{oe}/Z_{oo} is constant regardless of the impedance level.) To change impedance levels (from 50 to 75 ohms, for example) only the width of the lines needs to be changed in a manner similar to that for a single microstrip line.

As an aid in interpolating on the chart, note that the spacings between lines of constant S/H vary logarithmically to a very close

approximation when measured in the direction of constant W/H . Likewise, the variation of the spacings between lines of constant W/H is also closely logarithmic when measured in the direction of constant S/H . That is, in each case, the linear distance between curves of value 0.1 and 0.2 is nearly the same as the linear distance between curves of value 0.2 and 0.4, etc.

If Figure A-1 ($\epsilon_r = 9.0$) is plotted over Figure A-2 ($\epsilon_r = 10.0$), the effects of changes in substrate relative dielectric constant become readily apparent. Curves of constant S/H lie very nearly in the same location in both cases. The curves of constant W/H are shifted, however, in such a way that wider microstrip lines are required to maintain the same impedance on substrates of lower dielectric constant (in the manner similar to that of a single microstrip line). The important observation in this case is that to hold coupling constant as ϵ_r varies, the spacing between lines (S/H) is held constant and the individual line widths are changes to compensate for the variation of ϵ_r . Clearly then, coupled lines may be trimmed to the proper impedance levels by adding or subtracting to the line widths at the outside or uncoupled edges.

approximation when measured in the direction of constant W/H. Likewise, the variation of the spacings between lines of constant W/H is also closely logarithmic when measured in the direction of constant S/H. That is, in each case, the linear distance between curves of value 0.1 and 0.2 is nearly the same as the linear distance between curves of value 0.2 and 0.4, etc.

If Figure A-1 ($\epsilon_r = 9.0$) is plotted over Figure A-2 ($\epsilon_r = 10.0$), the effects of changes in substrate relative dielectric constant become readily apparent. Curves of constant S/H lie very nearly in the same location in both cases. The curves of constant W/H are shifted, however, in such a way that wider microstrip lines are required to maintain the same impedance on substrates of lower dielectric constant (in the manner similar to that of a single microstrip line). The important observation in this case is that to hold coupling constant as ϵ_r varies, the spacing between lines (S/H) is held constant and the individual line widths are changes to compensate for the variation of ϵ_r . Clearly then, coupled lines may be trimmed to the proper impedance levels by adding or subtracting to the line widths at the outside or uncoupled edges.

REFERENCES

1. A. J. Bahr, R. E. Lee, and A. F. Podell, "The Grating Array: A New Acoustic Surface Wave Transducer," Paper P-6, 1971 IEEE Ultrasonics Symposium, Miami Beach, Florida (December 1971).
2. A. J. Bahr, R. E. Lee, and A. F. Podell, "The Grating Array: A New Surface Acoustic Wave Transducer," Proc. IEEE, Vol. 60, pp. 443-444 (April 1972).
3. R. M. White and F. W. Voltmer, "Direct Piezoelectric Coupling to Surface Elastic Waves," Appl. Phys. Lett., Vol. 7, pp. 314-316 (December 15, 1965).
4. R. M. Arzt and K. Dransfeld, "Excitation of Rayleigh Waves at High Frequencies and Low Temperatures," Appl. Phys. Lett., Vol. 7, pp. 156-158 (September 15, 1965).
5. W. P. Mason, Ed., Physical Acoustics, Vol. 1, Part A, Chapt. 3 (Academic Press, New York, N.Y., 1964).
6. T. Krairojananan and W. Redwood, "Piezoelectric Generation and Detection of Ultrasonic Surface Waves by Interdigital Electrodes: An Electrical Equivalent Circuit," Electronic Letters, Vol. 5, pp. 134-135 (April 1969).
7. W. R. Smith, et al., "Analysis of Interdigital Surface Wave Transducers by Use of an Equivalent Circuit Model," IEEE Trans. on Microwave Theory and Techniques, Vol. MTT-17, pp. 856-864 (November 1969).
8. R. F. Mitchell, W. Willis and M. Redwood, "Electrode Interactions in Acoustic Surface-Wave Transducers," Electronic Letters, Vol. 5, pp. 456-457 (September 1969).
9. W. R. Smith and H. M. Gerard, "Differences Between In-Line and Crossed-Field Three-Port Circuit Models for Interdigital Transducers," IEEE Trans. on Microwave Theory and Techniques, Vol. MTT-19, pp. 416-417 (April 1971).

10. W. S. Jones, C. S. Hartman, and T. D. Sturdivant, "Second Order Effects in Surface Wave Devices," IEEE Trans. on Sonics and Ultrasonics, Vol. SU-19, pp. 368-376 (July 1972).
11. W. R. Smith, H. M. Gerard, and W. R. Jones, "Analysis and Design of Dispersive Interdigital Surface-Wave Transducers," IEEE Trans. on Microwave Theory and Techniques, Vol. MTT-20, pp. 458-471 (July 1972).
12. R. H. Tancrell and M. G. Holland, "Acoustic Surface Wave Filters," Proc. IEEE, Vol. 59, pp. 393-409 (March 1971).
13. G. L. Matthaei, L. Young, and E.M.T. Jones, Design of Microwave Filters, Impedance-Matching Networks, and Coupling Structures, p. 28 (McGraw Hill Book Co., New York, N.Y., 1964).
14. H. Skeie, "Electrical and Mechanical Loading of a Piezoelectric Surface Supporting Surface Wave," J. Acoust. Soc. Am., Vol. 48, No. 5 (Part 2), pp. 1098-1109 (November 1970).
15. A. W. Nalamwar and M. Epstein, "Immittance Characterization of Acoustic Surface Wave Transducers," Proc. IEEE, Vol. 60, No. 3, pp. 336-337 (March 1972).
16. H. Gerard, M. Walk, W. Jones, and R. Weglein, "Large Time-Bandwidth Product Microwave Delay Lines," TECH Report ECOM-0385, First Semi-annual Progress Report, Hughes Aircraft Co., Fullerton, California (January 1970).
17. R. F. Milsom and W. Redwood, "Generation of Acoustic Waves by a Single Pair of Electrodes on the Surface of Piezoelectric Ceramics," Electronic Letters, Vol. 7, No. 18, pp. 541-544 (September 9, 1971).
18. R. V. Schmidt, "Excitation of Shear Acoustic Waves by an Interdigital Transducer Operated at Its Surface-Wave Center Frequency," J. Appl. Phys., Vol. 43, No. 6, pp. 2498-2501 (June 1972).
19. P. H. Carr, "The Generation and Propagation of Acoustic Surface Waves at Microwave Frequencies," IEEE Trans. on Microwave Theory and Techniques, Vol. MTT-17, No. 11, pp. 845-855 (November 1969).
20. G. L. Matthaei and E. G. Cristal, "Theory and Design of Diplexers and Multiplexers," Advances in Microwaves, Vol. 2, Leo Young, Ed. (Academic Press, New York, N.Y., 1967).

21. R. J. Wenzel, "Applications of Exact Synthesis Methods to Multi-channel Filter Design," IEEE Trans. on Microwave Theory and Techniques, Vol. MTT-13, pp. 5-15 (1965).
22. E. G. Cristal, A. Podell, and S. B. Cohn, "Microwave Active Network Synthesis," Semiannual Report 1, Contract DAAB07-70-C-0044, SRI Project 8245, Stanford Research Institute, Menlo Park, California (October 1971).
23. E. G. Cristal, A. Podell, and S. B. Cohn, "Microwave Active Network Synthesis," Final Report, Contract DAAB07-70-C-0044, SRI Project 8245, Stanford Research Institute, Menlo Park, California (February 1972).
24. E. G. Cristal, "Meander Line and Hybrid Meander Line Transformers," 1972 IEEE-GMTT International Microwave Symposium Digest, IEEE Catalog No. 72 CHO 612-2-MTT, pp. 149-152 (May 22-24, 1972).
25. R. Sato, "A Design Method for Meander-Line Networks Using Equivalent Circuit Transformations," IEEE Trans. on Microwave Theory and Techniques, Vol. MTT-19, pp. 431-442 (May 1971).
26. H. Ozaki and J. Ishii, "Synthesis of Transmission-Line Networks and the Design of UHF Filters," IEEE Trans. on Circuit Theory, Vol. CT-2, pp. 325-333 (December 1955).
27. J. W. Bandler and C. Charalambous, "A New Approach to the Computer-Aided Design of Microwave Circuits," 1972 IEEE-GMTT International Microwave Symposium Digest, IEEE Catalog No. 72 CHO 612-2-MTT, pp. 121-123 (May 22-24, 1972).
28. W. J. Getsinger, "Coupled Rectangular Bars Between Parallel Plates," IRE Trans. on Microwave Theory and Techniques, Vol. MTT-10, pp. 65-73 (January 1962).
29. T. G. Bryant and J. W. Weiss, "Parameters of Microstrip Transmission Lines and of Coupled Pairs of Microstrip Lines," IEEE Trans. on Microwave Theory and Techniques, Vol. MTT-16, No. 12, pp. 1021-1027 (December 1968).